

Alma Mater Studiorum - Università di Bologna

DOTTORATO DI RICERCA IN  
AUTOMOTIVE PER UNA MOBILITÀ INTELLIGENTE

Ciclo 34

**Settore Concorsuale:** 09/E2 - INGEGNERIA DELL'ENERGIA ELETTRICA

**Settore Scientifico Disciplinare:** ING-IND/32 - CONVERTITORI, MACCHINE E AZIONAMENTI ELETTRICI

MULTI-PHASE ELECTRIC DRIVES FOR MOBILITY

**Presentata da:** Luca Vancini

**Coordinatore Dottorato**

Nicolò Cavina

**Supervisore**

Angelo Tani

**Co-supervisore**

Mattia Ricco

**Esame finale anno 2022**



## Summary

|       |  |    |
|-------|--|----|
| 0     | Introduction .....   | 1  |
| 1     | Mathematical Instruments and Machine Models .....  | 5  |
| 1.1   | Simplifying Assumptions.....   | 6  |
| 1.2   | Magnetic Field in the Air Gap .....  | 6  |
| 1.2.1 | Magnetic Field in the Air Gap Generated by the Stator Windings .....                           | 6  |
| 1.2.2 | Magnetic Field Generated by the Rotor Windings .....   | 9  |
| 1.2.3 | Total Magnetic Field.....  | 11 |
| 1.3   | Flux Linkage .....   | 11 |
| 1.3.1 | Flux Linkage with a Stator Phase.....  | 11 |
| 1.3.2 | Flux Linkage with a Rotor Phase .....  | 12 |
| 1.4   | Electromagnetic Torque .....   | 13 |
| 1.5   | Model of Five-Phase Wound-Rotor Induction Machines .....                                       | 14 |
| 1.5.1 | Magnetic Field .....   | 15 |
| 1.5.2 | Flux Linkages.....   | 18 |
| 1.5.3 | Electromagnetic Torque .....   | 21 |
| 1.5.4 | Summary of the Mathematical Model of the five-Phase Wound-Rotor Induction Machines .....       | 22 |
| 1.6   | Model of Six-Phase Permanent Magnet Synchronous Machines .....                                 | 23 |
| 1.6.1 | Magnetic Field .....   | 23 |
| 1.6.2 | Flux Linkages.....   | 30 |
| 1.6.3 | Electromagnetic Torque .....   | 32 |
| 1.6.4 | Summary of the Mathematical Model of the Six-Phase Permanent Magnet Synchronous Machines ..... | 33 |
| 2     | Voltage Balancing of the DC-Link Capacitors in Three-Level T-Type Multi-phase Inverters .....  | 35 |
| 2.1   | Voltage Balance in a Multilevel Multi-Phase Inverter .....                                     | 36 |
| 2.2   | Control Scheme for Voltage Balance .....   | 43 |
| 2.3   | Domain Without Low-Frequency Voltage Oscillations.....   | 44 |
| 2.4   | Experimental Results .....   | 47 |
| 2.5   | Conclusions.....   | 53 |

|       |  |     |
|-------|--|-----|
| 3     | Detection and Estimation of Magnet Demagnetization in Six-Phase Permanent Magnet Synchronous Motor ..... | 55  |
| 3.1   | Permanent Magnet Synchronous Motor.....  | 56  |
| 3.2   | Effect of Demagnetization.....   | 57  |
| 3.3   | Diagnostic Algorithm .....   | 59  |
| 3.4   | Control Scheme .....   | 64  |
| 3.4.1 | Speed Regulator.....   | 64  |
| 3.4.2 | Current Regulators.....  | 65  |
| 3.4.3 | Diagnostic Algorithm.....  | 65  |
| 3.4.4 | Modulation Block.....  | 66  |
| 3.5   | Experimental Results .....   | 67  |
| 3.6   | Experimental Tests on the Healthy Machine .....  | 68  |
| 3.7   | Experimental Tests on the Faulty Machine .....   | 70  |
| 3.8   | Conclusions.....   | 72  |
| 4     | Overmodulation Strategies for Five-Phase Inverters .....   | 73  |
| 4.1   | Overmodulation .....   | 74  |
| 4.2   | Modulation Regions in Five Phase Inverters .....   | 74  |
| 4.3   | Extended Linear Modulation Region.....   | 77  |
| 4.4   | Overmodulation Region .....  | 83  |
| 4.4.1 | Minimum Phase Error.....   | 83  |
| 4.4.2 | Minimum Distance.....  | 84  |
| 4.4.3 | Bolognani's Modulation.....  | 87  |
| 4.5   | Experimental Result.....   | 89  |
| 4.6   | Conclusion .....   | 96  |
| 5     | Model of Eighteen-Phase Squirrel Cage Induction Machine .....  | 97  |
| 5.1   | Magnetic Field .....   | 98  |
| 5.1.1 | Magnetic Field Produced by the Stator Currents.....  | 99  |
| 5.1.2 | Magnetic Field Produced by the Rotor Currents.....   | 101 |
| 5.1.3 | Air Gap Magnetic Field.....  | 104 |
| 5.2   | Flux Linkages.....   | 104 |

|       |   |     |
|-------|---|-----|
| 5.2.1 | Flux Linkage with a Stator Ohase .....  | 104 |
| 5.2.2 | Flux linkage with a Rotor Loop.....   | 105 |
| 5.3   | Voltage Equations.....  | 106 |
| 5.4   | Electromagnetic Torque .....  | 107 |
| 5.5   | Summary of the Mathematical Model of the Eighteen-Phase Two Poles Squirrel Cage Induction Machines..... | 108 |
| 5.5.1 | Equations .....   | 108 |
| 5.5.2 | MatLab- Simulink Tests .....  | 109 |
| 6     | References.....   | I   |



*I want to thank my family for supporting me even in this academic experience.*

*Thank a lot Angelo Tani and Michele Mengoni for their time and for having guided me during my Ph.D. program.*

*Last but not least, thanks to my colleagues from Bologna university for helping me during these three years.*



# *Introduction*

*Nowadays, electric mobility is widely seen as a way to improve the environmental sustainability of transport, and new research trends are aimed to promote reliability and reduce energy waste. Future vehicles will increasingly integrate electrical systems to cope with ecological policies and reduce the consumption of resources.*

*This thesis aims to contribute to the technological development of electric vehicles of the future by suggesting solutions to improve the performance and the reliability of innovative motor drives. Some different topics, concerning the inverter, the motor and the system diagnosis will be addressed. In particular, the attention will be focused on multi-phase and multilevel technologies, and their potential advantages with respect to traditional technologies.*

*The power rating of the converter should meet the required level for the machine and driven load. However, the converter ratings cannot be increased over a certain range due to the limitation on the power rating of semiconductor devices. The advent of inverter-fed motor drives also removed the limits of the number of motor phases. This fact made it possible to design machines with more than three phases and brought about the increasing investigation and applications of multi-phase motor drives.*

*A multi-phase inverter is the generalization of a three-phase inverter obtained through the parallel connection of a higher number of inverter legs. In three-phase systems, the most widespread control techniques are the carrier-based Pulse Width Modulation (PWM) and the Space Vector Modulation (SVM). The same strategies can be extended to multi-phase converters [1]. The analysis is difficult because the resulting number of possible configurations cannot be described through a two-dimensional representation but requires a multidimensional description. The Vector Space Decomposition (VSD) solves this problem by introducing new complex planes or subspaces that are intrinsically linked to specific spatial harmonics of the magnetic field of the electric machine.*

*The multi-phase technology has a more significant number of degrees of freedom in comparison with the three-phase one. This increasing number of degrees of freedom allows independent control of the magnetic field's harmonics in the air gap after the fundamental one [2].*

*The greater number of degrees of freedom can be successfully utilized in order to increase the torque per RMS amperes for the same volume machine [3]. Also, multi-phase motor drive allows to increase the frequency of torque pulsations [4], the reliability [5], lower the dc-link current harmonics and carry out on-line machine diagnostics without affecting the system behaviour.*

*For their intrinsic increased reliability, the multi-phase drives play a crucial role in high-reliability applications where fault tolerance is an essential requirement to guarantee the operation in critical conditions. The marine and aeronautical applications [6] well represent this combination of robustness requirements and high-power operating conditions but, in recent years, also the automotive industries [7]*

[8] are taking an interest in these applications. Furthermore, multi-phase systems have features that make them competitive in many other industrial areas.

In addition to the multi-phase technology, in the last decades also the multilevel technology has been developed.

Multilevel converters are finding increased attention in the field of electronic power conversion for high-power applications. The multilevel converters [9] use switches of reduced voltage rating to develop high power level converters. Currently, they are commercialized in standard and customized products that power a wide range of applications, reactive power compensation [10], marine propulsion [11], high-voltage direct-current (HVDC) transmission [12], wind energy conversion [13], railway traction [14], automotive systems [15], [16].

Although it is an enabled and already proven technology, multilevel converters present many challenges, and they offer a great range of possibilities for their development. Researchers are contributing to improving energy efficiency, reliability, power density, and cost of multilevel converters. The traditional multilevel converter topologies, such as the neutral point clamped (NPC), cascaded H-bridge (CHB), and flying capacitor (FC), are the most used [9]. From these technologies the 3L-NPC and the CHB are the most popular in the industry [17] due to low voltage stress on switches, better harmonic performance, low switching frequency, and less switching losses.

Note that, multi-phase technology has many advantages in common with the multilevel technology. In multi-phase machines, by dividing the required power between multiple phases, more than the conventional three, higher power levels can be obtained and power electronic converters with limited power range switches can be used to drive the multi-phase machine.

This thesis is divided into five chapters, and, in each of them, a different topic is addressed.

The first chapter introduces the mathematical models of two different multi-phase machines, i.e., the five-phase wound-rotor induction machine, and the asymmetrical six-phase permanent magnet synchronous machine, which will be used in the following chapters to study different aspects of the drives. The study of the multi-phase systems will be based on the Vector Space Decomposition approach. This mathematical method allows simplifying the analysis by describing the systems with decoupled sets of equations.

The second chapter will be focused on T-type multilevel multi-phase inverters, which represent an interesting opportunities for an electric vehicle motor drive. In particular, a well-known problem of the T-type multilevel inverter, that is the voltage balancing of the DC-link capacitors, will be analysed. In literature, this problem has been analysed in deep by the scientific community for three-phase systems and many papers have been published [18], [19], [20]. This problem has been recently analysed for multi-phase systems [21], [18], where the techniques proposed in those papers are based on an iterative routine. In this thesis, an innovative control technique, which ensures flexible management of the voltages on the DC-link capacitors will be presented. The effectiveness of the technique, as well as its operating range, will be validated by experimental tests on a five-phase wound-rotor inductor motor. The proposed solution can

also be used in applications where the bus-dc is composed of batteries with different voltages. In this case, the proposed solution can guarantee the correct operation of the inverter and, consequently, the drives.

The third chapter will present an online algorithm for the diagnosis of the magnet demagnetization in six-phase permanent magnet synchronous motors. The analysis of the state of health of the machine is a fundamental point to guarantee the safety of the electric vehicle. The scientific community always has interest in the diagnostic. The diagnosis of the magnet demagnetization in multiphase PMSM has been analysed in several papers. The state of health of the rotor magnets can be analysed using passive and active methods. Passive methods commonly use the motor back-emf. They are simple but are poorly reliable at low speed [22]. Active methods inject high frequency harmonics to obtain information [23] or use additional sensors [24] or search coil [25]. The proposed algorithm, which is based on the analysis of the electromotive force induced in the stator windings by the rotor magnets, is able to evaluate the state of the health of the traction electric motor on board the vehicle while the vehicle is running. Analytic analysis of the effects of the magnets demagnetization in case of rotor magnets with parallel magnetization will be given.

The fourth chapter will study the overmodulation operating region of multi-phase inverters. This topic is fascinating, and for three-phase systems has been studied in deep by the researcher community in the past [26], [27], [28]. In recent years, the overmodulation techniques for multiphase systems have been studied. The overmodulation techniques can be based on the Space Vector Modulation (SVM) approach or on the Space Vector Pulse Width Modulation (SVPWM) approach. A procedure for the analysis of the overmodulation region for  $n$ -phase systems is presented in [29]. In contrast, a PWM strategy for dual three-phase PMSM operating in the overmodulation region is presented in [30], and [31] reports a generalization of overmodulation for multiphase PMSM drives. The activity presented in this chapter emphasizes the peculiarity related to the increased number of phases. Specifically, exploiting the degrees of freedom of multi-phase systems, a new “extended linear zone” will be introduced and studied in details. Experimental tests with a five-phase wound-rotor induction motor will validate the proposed solution. The extension of the linear range allows increasing the available voltage on the motor drive, for a prefixed DC-link voltage, enabling higher speed operating conditions. Moreover, a generalisation for multi-phase systems of the traditional three-phase overmodulation techniques will be given.

In the last chapter, the mathematical model of an eighteen-phase squirrel cage induction motor will be presented. This particular electric machine will be used for the development of an innovative variable-pole motor drive for traction applications. The model is based on the Vector Space Decomposition approach, and takes into account up to the 35<sup>th</sup> spatial harmonic of the magnetic field in the air gap. This activity is the result of part of a collaboration made with the KTH, Royal Institute of Technology in Stockholm.



# Chapter 1

## *Mathematical Instruments and Machine Models*

*In this chapter, the mathematical instruments and the machine models, that are the basis of the study carried out during the Ph.D., will be presented.*

*All the mathematical developments in this thesis will exploit the potentiality of the well-known Vector Space Decomposition (VSD) approach, which allows a simple and effective representation of the multi-phase systems by means of multiple space vectors.*

*Firstly, the evaluation of the magnetic field in a uniform air gap, produced by a generic coil with an arbitrary position, arranged both in the stator or rotor slots, will be carried out.*

*Then, the relation of the linkage flux with the stator and rotor phases, due to the magnetic field in the air gap, will be obtained.*

*Subsequently, the expression of the electromagnetic torque in terms of magnetic field produced by the stator and the rotor currents will be given.*

*Finally, the mathematical models of the two multi-phase machines under study, i.e., the five-phase wound-rotor induction machine and the six-phase permanent magnet synchronous machines, will be determined.*

*In the following chapters, only the aspects of the machines related to the applications of the case of study will be studied in depth.*

## 1.1 Simplifying Assumptions

A rigorous analysis of an electrical machine represents a very hard task. Therefore, some simplifying assumptions are usually introduced in order to make the mathematical model more compact and useful. The main assumptions adopted in this thesis are listed hereafter.

- The air gap of the machine is supposed perfectly uniform, i.e. the air gap length is the same everywhere. This assumption is more acceptable for machines with semi-closed slots.
- The B-H relationship of the ferromagnetic material adopted for stator and rotor cores is assumed linear. This means that the effects of magnetic saturation are not taken into account.
- An infinite value of the magnetic permeability of the ferromagnetic material is assumed. Consequently, the drop of magnetomotive force in the stator and rotor cores is negligible.
- All the cross sections of the electrical machine are supposed equivalent, i.e. the axial length of the machine is assumed very large. According to this hypothesis, it is possible to carry out a two dimensional analysis of the system.
- The magnetic field in the airgap is supposed to be radial and the bending of the airgap is neglected (the radial component of the field results in parallel flux lines).
- The mutual magnetic coupling between different phases, due to the leakage fluxes, is assumed negligible. Note that, the leakage fluxes are typically localized in the end-winding of the coils, and within the stator and rotor slots.

## 1.2 Magnetic Field in the Air Gap

In this section, the magnetic field in the air gap is determined. The two contributions, due to stator and rotor windings, are separately evaluated.

### 1.2.1 Magnetic Field in the Air Gap Generated by the Stator Windings

A simple stator winding, constituted by only one coil with  $n_s$  turns for each pole pair, is considered. All the coils are series connected. Due to the symmetry of the machine, the analysis can be limited to a single pair of poles. The number of pole pairs of the machine is  $p$ .

In Fig. 1.1, a schematic representation of a generic stator coil in a cross section of a pole pair of the machine is shown. The coil of the phase  $k$  is in an arbitrary position, and his angular pitch is equal to  $\gamma$ . Its magnetic axis can be localized by the specific value  $\psi_{sk}$  of the electrical coordinate  $\theta_s$ , whose origin is positioned on the x-axis. Unless otherwise stated, all coordinates will be considered in electrical angles.

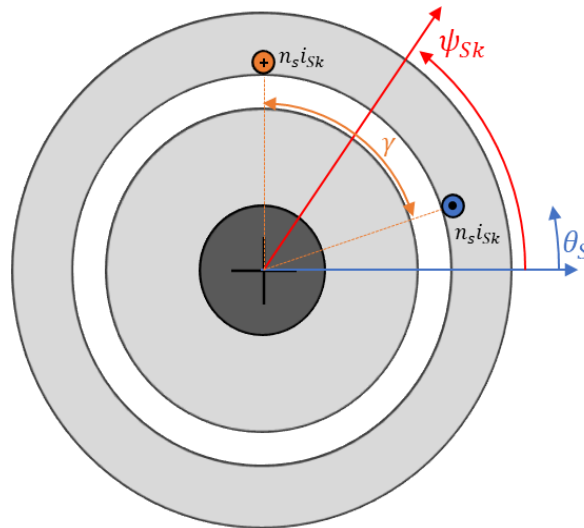


Figure 1.1 Representation of a generic stator coil in electrical coordinate.

The generic stator winding represented in Fig. 1.1 produces a magnetic field in the air gap having a square waveform, as shown in Fig. 1.2.

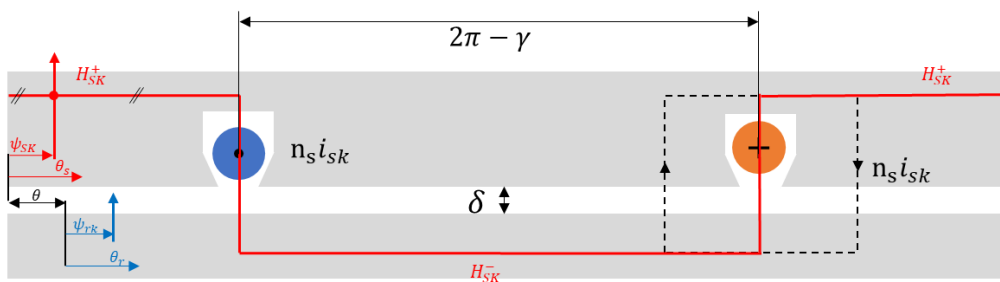


Figure 1.2 Waveform of the magnetic field generated by a generic winding.

The distribution of the magnetic field in the air gap can be obtained by Ampere's and the Gauss's laws, as shown in (1.1). The arbitrary closed curve taken into consideration is represented as a black dashed line in Fig. 1.2.

$$\oint \vec{H} \cdot \vec{l} \approx H_{Sk}^+ \delta - H_{Sk}^- \delta = n_s i_{sk} \quad (1.1)$$

where:

$$H_{Sk}^+ = n_s \frac{i_{sk}}{\delta} \frac{(2\pi - \gamma)}{2\pi} \quad (1.2)$$

$$H_{Sk}^- = -n_s \frac{i_{sk}}{\delta} \frac{\gamma}{2\pi} \quad (1.3)$$

are the values of the magnetic field shown in Fig. 1.2.

Let us define the relationship between the number of conductors in series per phase ( $N_s$ ) and the number of conductors in slots ( $n_s$ ) as:

$$n_s = \frac{N_s}{2p} \quad (1.4)$$

where  $p$  is the number of pole pairs.

The square waveform of the magnetic field in the air gap, produced by the generic stator winding, can be represented by Fourier expansion, as in (1.5):

$$h_{Sk}(\theta_s, t) = \sum_{\rho} H_{Sk\rho} \cos(\rho(\psi_{Sk} - \theta_s)) \quad (1.5)$$

where:

$$H_{Sk\rho} = \frac{1}{\pi} \int_{\psi_{Sk}-\frac{\gamma}{2}}^{\psi_{Sk}+\frac{\gamma}{2}} H_{Sk}^+ \cos(\rho\theta_s) d\theta_s - \frac{1}{\pi} \int_{\psi_{Sk}+\frac{\gamma}{2}}^{\psi_{Sk}-\frac{\gamma}{2}} H_{Sk}^- \cos(\rho\theta_s) d\theta_s \quad (1.6)$$

Solving (1.6) it is possible to obtain the expression of  $H_{Sk\rho}$  as:

$$H_{Sk\rho} = \frac{N_s i_{Sk}}{\rho\pi\delta p} \sin\left(\rho\frac{\gamma}{2}\right) \quad (1.7)$$

Replacing (1.7) in (1.5) leads to:

$$h_{Sk}(\theta_s, t) = \sum_{\rho \text{ odd}} \frac{N_s i_{Sk}}{\pi\delta p\rho} \sin\left(\rho\frac{\gamma}{2}\right) \cos(\rho(\psi_{Sk} - \theta_s)) \quad (1.8)$$

According to the Euler equation ( $e^{ix} = \cos(x) + i \sin(x) \rightarrow \cos(x) = \text{Re}[e^{ix}]$ ) (1.9) can be rewritten as:

$$h_{Sk}(\theta_s, t) = \sum_{\rho \text{ odd}} \frac{N_s i_{Sk}}{\pi\delta p\rho} \sin\left(\rho\frac{\gamma}{2}\right) \text{Re}[e^{j\rho(\psi_{Sk}-\theta_s)}] \quad (1.9)$$

It is possible to generalize (1.9) for a generic winding arrangement that is distributed in more than one slot per pole per phase and/or with shortened coils, by introducing the winding factor (1.10):

$$K_w = K_{BF} K_{SF} \quad (1.10)$$

where  $K_{BF}$  is the Blondel's factor that represents the distribution of the coil into the machine slots, whereas  $K_{SF}$  is the shortening factor. They are evaluated as:

$$K_{BF} = \frac{\sin\left(q\frac{\alpha}{2}\right)}{q\sin\left(\frac{\alpha}{2}\right)} \quad (1.11)$$

$$K_{SF} = \cos\left(\frac{\beta}{2}\right) \quad (1.12)$$

where  $q$  is the number of slots for pole for phase,  $\alpha$  is the angle between two adjacent slots and  $\beta$  is the angle of shortening.

Consequently, assuming  $\psi_{sk}$  as the position of the magnetic axis of the  $k^{th}$  phase, (1.9) can be rewritten as:

$$h_{sk}(\theta_s, t) = \sum_{\rho \text{ odd}} \frac{N_s i_{sk} K_{wS}}{\pi \delta p \rho} \sin\left(\rho \frac{\gamma}{2}\right) \text{Re}\left[e^{j\rho(\psi_{sk} - \theta_s)}\right] \quad (1.13)$$

The total magnetic field produced by stator, in the stator reference frame, is the sum of the magnetic fields generated by each phase, and can be written as:

$$h_s(\theta_s, t) = \sum_{\rho \text{ odd}} \frac{N_s K_{wS}}{\pi \delta p \rho} \sin\left(\rho \frac{\gamma}{2}\right) \text{Re}\left[e^{-j\rho\theta_s} \sum_{k=1}^N i_{sk}(t) e^{j\rho\psi_{sk}}\right] \quad (1.14)$$

It is possible to compact (1.14) by introducing the following new quantities:

$$\bar{h}_{s\rho}^S(t) = \frac{N_s K_{wS}}{\pi \delta p \rho} \sin\left(\rho \frac{\gamma}{2}\right) \sum_{k=1}^N i_{sk}(t) e^{j\rho\psi_{sk}} \quad (1.15)$$

The complex variable  $\bar{h}_{s\rho}^S(t)$  describes the time evolution, in terms of amplitude and position, of the  $\rho$ -th spatial harmonic of the magnetic field in the air gap produced by the stator windings. The superscript S indicates that this quantity is represented in the stator reference frame. In general, the absence of a superscript means that the superscript should be equal to the subscript.

Introducing (1.15) in to (1.14) it is possible to write:

$$h_s(\theta_s, t) = \sum_{\rho \text{ odd}} \text{Re}\left[\bar{h}_{s\rho}^S(t) e^{-j\rho\theta_s}\right] \quad (1.16)$$

### 1.2.2 Magnetic Field Generated by the Rotor Windings

The same procedure used to obtain the magnetic field into the air gap produced by the stator windings can be used to determine the magnetic field produced by the rotor windings.

The relationship between the mechanical angle  $\theta_m$  and the electrical angle  $\theta$  is the following:

$$\theta = p\theta_m \quad (1.17)$$

A schematic draw of a cross section of a pole pair of the machine, with a generic rotor coil, is shown in Fig. 1.3.

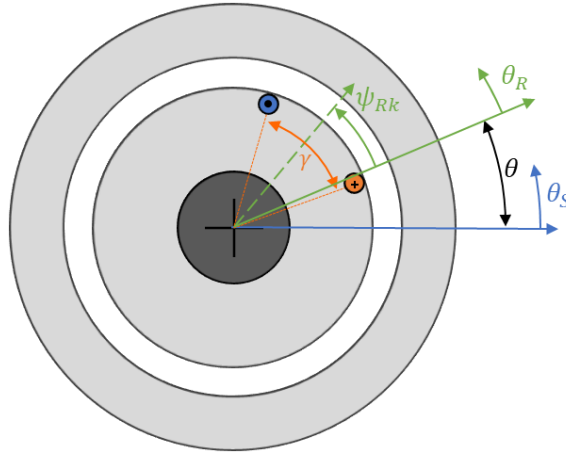


Figure 1.3 Representation of a generic coil of the rotor winding.

Observing Fig. 1.3, the variable  $\psi_{Rk}$  is the angular coordinate of the magnetic axis of the  $k^{th}$  rotor coil and the relationship between the stator and the rotor coordinates is the following:

$$\theta_S = \theta_R + \theta \quad (1.18)$$

where  $\theta$  is the rotor position in electrical radians.

According to the spatial Fourier expansion, the magnetic field in the air gap produced by the rotor windings can be expressed as follows:

$$h_R(\theta_R, t) = \sum_{\rho \text{ odd}} \text{Re}[\bar{h}_{R\rho}^R(t)e^{-j\rho\theta_R}] \quad (1.19)$$

where  $\bar{h}_{R\rho}^R(t)$  is:

$$\bar{h}_{R\rho}^R(t) = \frac{N_R K_{wR}}{\pi \delta p \rho} \sin\left(\rho \frac{\pi}{2}\right) \sum_{k=1}^N i_{Rk} e^{j\rho\psi_{Rk}} \quad (1.20)$$

The quantity  $N_R$  represents the number of rotor conductors in series per phase,  $\theta_R$  is the angular coordinate of the rotor reference frame and  $\psi_{Rk}$  the angular coordinate of the magnetic axis of the  $k^{th}$  rotor winding.

### 1.2.3 Total Magnetic Field

The total magnetic field in the air gap is obtained by summing the stator and rotor contribution.

The expression of the total magnetic field in the stator reference frame is the following:

$$h_T(\theta_s, t) = \sum_{\rho \text{ odd}} \text{Re}[\bar{h}_{S\rho} e^{-j\rho\theta_s} + \bar{h}_{R\rho} e^{j\rho(\theta-\theta_s)}] \quad (1.21)$$

In the rotor reference frame, (1.21) can be rewritten as:

$$h_T(\theta_R, t) = \sum_{\rho \text{ odd}} \text{Re}[\bar{h}_{S\rho} e^{-j\rho(\theta+\theta_R)} + \bar{h}_{R\rho} e^{-j\rho\theta_R}] \quad (1.22)$$

## 1.3 Flux Linkage

In this section, the flux linkages with the stator and rotor windings, due to the magnetic field in the air gap, are evaluated.

### 1.3.1 Flux Linkage with a Stator Phase

A simple stator winding, constituted by only one coil with  $n_s$  turns for each pole pair, is considered. With reference to the  $k^{\text{th}}$  stator phase, it is possible to consider the red surface at the air gap shown in Fig. 1.4, that is delimited by the axial lengths of the machine (L) and the coil pitch of the coil  $[(\psi_{Sk} + \frac{\pi}{2}) - (\psi_{Sk} - \frac{\pi}{2})]$ .

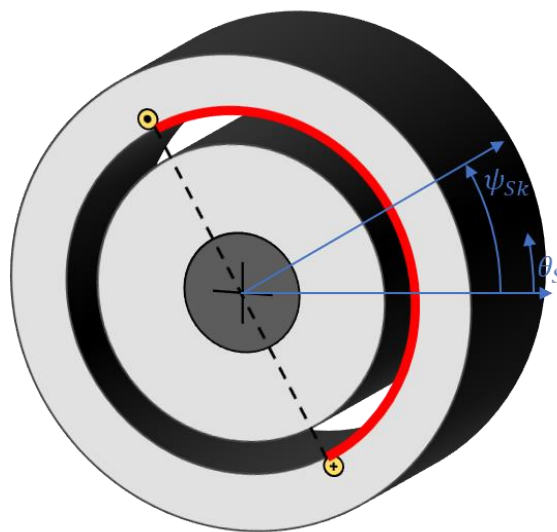


Figure 1.4 Surface at the air gap of a generic stator coil in an arbitrary position.

From the Gauss's law, the magnetic flux through a generic surface  $S$  can be expressed as:

$$\varphi = \iint_S \bar{B} \cdot \hat{n} dS \quad (1.23)$$

Substituting the generic surface  $S$  with the red surface of integration individuated in Fig 1.4, it is possible to obtain the following expression of the flux linkage with the generic  $k^{th}$  phase, due to the magnetic field in the air gap:

$$\varphi_{STk} = n_s \mu_0 \int_0^L \int_{\psi_{Sk}-\frac{\pi}{2}}^{\psi_{Sk}+\frac{\pi}{2}} h_t(\theta_S, t) R d\theta_S dl \quad (1.24)$$

where  $R$  is the mean radius in the air gap of the machine.

According with the assumptions, since the magnetic field is independent of the axial position in the air gap, (1.24) can be rewritten as:

$$\varphi_{STk} = n_s \mu_0 L \int_{\psi_{Sk}-\frac{\pi}{2}}^{\psi_{Sk}+\frac{\pi}{2}} h_t(\theta_S, t) R d\theta_S \quad (1.25)$$

Remembering that the pole pitch is the distance between two slots that contain the same phase, defined as:

$$\tau = \frac{2\pi}{2p} R \quad (1.26)$$

The general expression of the flux linkage with a generic phase in position  $\Psi_{Sk}$  can be achieved:

$$\varphi_{STk} = \frac{N_S}{2} \mu_0 L \int_{\Psi_{Sk}-\frac{\pi}{2}}^{\Psi_{Sk}+\frac{\pi}{2}} h_t(\theta_S, t) \frac{\tau}{\pi} d\theta_S \quad (1.27)$$

### 1.3.2 Flux Linkage with a Rotor Phase

By following the same procedure adopted to obtain the expression of the flux linkage with a generic stator phase (1.27) it is possible to obtain the expression (1.28) that represents the flux linkage with a generic rotor phase.

$$\varphi_{RTk} = \frac{N_R}{2} \mu_0 L \int_{\psi_{Rk}-\frac{\pi}{2}}^{\psi_{Rk}+\frac{\pi}{2}} h_t(\theta_R, t) \frac{\tau}{\pi} d\theta_R \quad (1.28)$$

It is important to underline that, the flux linkages expressed by (1.27) and (1.28) represent only the contribution of the magnetic field in the air gap. Another contribution must be considered to achieve the total flux linkage, that is the leakage flux.

Under the hypothesis that mutual couplings due to the leakage fluxes, localized in the end-winding and between different phase coils into the same slot, are negligible, the leakage fluxes result to be proportional to the corresponding phase current by means of a simple leakage inductance. Note that, the leakage flux in the end-windings is usually weak, since a large part of the corresponding flux line path is in air. Furthermore, the mutual coupling in the slots is null when the windings are not shortened. It can be demonstrated that taking into account the mutual couplings due to the leakage fluxes would lead to different values of leakage inductances in each available space of the machine.

## 1.4 Electromagnetic Torque

The electromagnetic torque in electric machines can be determined by means of an energy balance. In general, the following expression can be written [32]

$$T_{em} = \frac{\partial W'_m(i_k, \theta_m)}{\partial \theta_m} \quad (1.29)$$

where  $T_{em}$  is the electromagnetic torque,  $\theta_m$  is the mechanical angle representing the position of the rotor with respect to the stator,  $i_k$  is the  $k^{th}$  phase current and  $W'_m$  is the magnetic co-energy stored in the magnetic field of the machine. According to the simplifying assumptions adopted, in (1.29) the magnetic co-energy can be replaced with the magnetic energy, leading to (1.30):

$$T_{em} = \frac{\partial W_m(i_k, \theta_m)}{\partial \theta_m} \quad (1.30)$$

Previous assumptions permit to consider the magnetic energy connected to leakage fluxes independent of the angular position  $\theta$ , since the mutual couplings due to the leakage fluxes between the stator and rotor windings are negligible. Therefore, to determine the torque is sufficient to consider the magnetic energy in the air gap  $W_{mT}$  only, so that (1.30) becomes (1.31).

$$T_{em} = \frac{\partial W_{mT}(i_k, \theta)}{\partial \theta} \quad (1.31)$$

The general definition of magnetic energy stored in the air gap of the machine, evaluated as the integral of the energy density in the air gap volume  $\nu$ , assumes the following form:

$$W_m = \frac{1}{2} \int_{\nu} \bar{H} \cdot \bar{B} \, d\nu \quad (1.32)$$

where  $\nu$  is the volume of the air gap. Taking into account a general distribution of the magnetic field in the air gap, the magnetic energy can be expressed as:

$$W_{mT} = \frac{1}{2} \mu_0 p \delta L \frac{\tau}{\pi} \int_0^{2\pi} h_T^2(\theta_s, t) d\theta_s \quad (1.33)$$

According to (1.21), (1.33) can be rewritten as follows:

$$W_{mT} = \frac{1}{2} \mu_0 p \delta L \tau \sum_{\rho \text{ odd}} |\bar{h}_{T\rho}^s|^2 \quad (1.34)$$

According to (1.31) and taking (1.21) into account, and by means of some mathematical developments, the electromagnetic torque takes the following form:

$$T_{em} = \mu_0 p^2 \delta L \tau \sum_{\rho \text{ odd}} \rho [\bar{h}_{S\rho} \cdot j \bar{h}_{R\rho} e^{j\rho\theta}] \quad (1.35)$$

Equation (1.35) shows how only stator and rotor space harmonics of the same order interact with each other to produce electromagnetic torque.

## 1.5 Model of Five-Phase Wound-Rotor Induction Machines

In this section, the model of a five-phase wound-rotor induction machine will be developed. Note that, the model will take into account all the spatial harmonics of the magnetic field in the air gap.

The five-phase wound-rotor induction machine is a symmetrical machine where each phase is rotated by  $\frac{2\pi}{5}$  electrical radians. It presents two different windings, one distributed in the stator slots, and another distributed in the rotor slots. A cross-section of the machine is represented in Fig. 1.5.

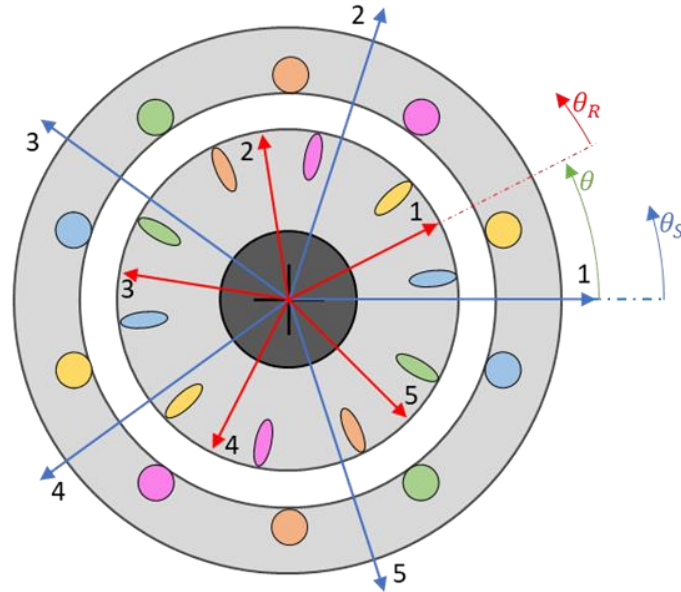


Figure 1.5 Cross section of a Five-Phase Induction Machine.

The study of the machine starts with the analysis of the magnetic field produced by stator and rotor windings.

### 1.5.1 Magnetic Field

The total magnetic field in the air gap is due to two contributions. The first one is the magnetic field produced by the currents flowing in the stator windings, and the second one is the magnetic field produced by the current induced in the rotor windings.

#### 1.5.1.1 Magnetic field produced by the stator currents

According to (1.14) and considering the positions of the magnetic axes of the stator windings shown in Fig. 1.5, it is possible to obtain the following expression of the magnetic field in the air gap, produced by the stator windings, in the five-phase induction machine.

$$h_s(\theta_s, t) = \sum_{\rho \text{ odd}} \frac{N_s K_{ws} \rho}{\pi \delta p \rho} \sin\left(\rho \frac{\pi}{2}\right) \text{Re} \left[ e^{-j\rho\theta_s} \left( i_{s1}(t) + i_{s2}(t) e^{j\frac{2\pi\rho}{5}} + i_{s3}(t) e^{j\frac{4\pi\rho}{5}} + i_{s4}(t) e^{j\frac{6\pi\rho}{5}} + i_{s5}(t) e^{j\frac{8\pi\rho}{5}} \right) \right] \quad (1.36)$$

Introducing the complex constant  $\bar{\alpha}_5 = e^{j\frac{2\pi}{5}}$  it is possible to rewrite (1.36), as follows:

$$h_s(\theta_s, t) = \sum_{\rho(\text{odd})=1}^{\infty} \frac{N_s K_{ws} \rho}{\rho \pi \delta p} \sin\left(\rho \frac{\pi}{2}\right) \Re_e \left[ \left( i_{s1}(t) + i_{s2}(t) \bar{\alpha}_5^\rho + i_{s3}(t) \bar{\alpha}_5^{2\rho} + i_{s4}(t) \bar{\alpha}_5^{3\rho} + i_{s5}(t) \bar{\alpha}_5^{4\rho} \right) e^{-j\rho\theta_s} \right] \quad (1.37)$$

Equation (1.37) suggests defining new complex variable (multiple space vectors), useful to represent both the evolution of the five stator currents and of the magnetic field in the air gap, by means of a specific Clarke transformation as follows:

$$\bar{i}_{S\rho} = \frac{2}{5} (i_{S1} + i_{S2}\bar{\alpha}_5^\rho + i_{S3}\bar{\alpha}_5^{2\rho} + i_{S4}\bar{\alpha}_5^{3\rho} + i_{S5}\bar{\alpha}_5^{4\rho}) \quad (1.38)$$

In (1.38),  $\rho$  can assume all the odd integer values but, as demonstrated below, only the three complex variables obtained for  $\rho = 1, 3$  and  $5$  are independent, and then sufficient to fully describe the behaviour of the currents in a five-phase system. Therefore, (1.38) can be explicitly rewritten as:

$$i_{S0} = \bar{i}_{S5} = \frac{2}{5} (i_{S1} + i_{S2} + i_{S3} + i_{S4} + i_{S5}) \quad (1.39)$$

$$\bar{i}_{S1} = \frac{2}{5} (i_{S1} + i_{S2}\bar{\alpha}_5^1 + i_{S3}\bar{\alpha}_5^2 + i_{S4}\bar{\alpha}_5^3 + i_{S5}\bar{\alpha}_5^4) \quad (1.40)$$

$$\bar{i}_{S3} = \frac{2}{5} (i_{S1} + i_{S2}\bar{\alpha}_5^3 + i_{S3}\bar{\alpha}_5^1 + i_{S4}\bar{\alpha}_5^4 + i_{S5}\bar{\alpha}_5^2) \quad (1.41)$$

It is possible to verify that:

$$\bar{i}_{S1} = \bar{i}_{S\rho} \quad \text{for } \rho = 1, 11, 21, \dots \quad (1.42)$$

$$\bar{i}_{S3} = \bar{i}_{S\rho} \quad \text{for } \rho = 3, 13, 23, \dots \quad (1.43)$$

$$\bar{i}_{S5} = \bar{i}_{S\rho} \quad \text{for } \rho = 5, 15, 25, \dots \quad (1.44)$$

$$\bar{i}_{S1}^* = \bar{i}_{S\rho} \quad \text{for } \rho = 7, 17, 27, \dots \quad (1.45)$$

$$\bar{i}_{S3}^* = \bar{i}_{S\rho} \quad \text{for } \rho = 9, 19, 29, \dots \quad (1.46)$$

where \* indicates the complex conjugate of the space vector.

It should be noted that,  $i_{S0}$ , called zero-sequence component, is a real quantity, whereas  $\bar{i}_{S1}$  and  $\bar{i}_{S3}$ , called space vectors in the  $\alpha_1 - \beta_1$  plane and  $\alpha_3 - \beta_3$  plane, respectively, are complex quantities. As can be seen, the number of degrees of freedom of the new variables is equivalent to the number of degrees of freedom of the five stator currents, confirming the correctness of the adopted Clarke transformation.

The compact expression of the adopted Clarke transformation for five-phase systems is:

$$\bar{i}_{S\rho} = \frac{2}{5} \sum_{k=1}^5 i_{Sk} \bar{\alpha}^{\rho(k-1)} \quad (1.47)$$

It can be demonstrated that the corresponding inverse transformations are [33]:

$$i_{Sk} = \frac{1}{2} i_{S0} + \sum_{\rho(\text{odd})=1}^3 \bar{i}_{S\rho} \cdot \bar{\alpha}_5^{\rho(k-1)} \quad k = 1, 2, \dots, 5 \quad (1.48)$$

Introducing (1.38) into (1.37) gives:

$$h_s(\theta_s, t) = \sum_{\rho(\text{odd})=1}^{\infty} \frac{5 N_s K_{ws\rho}}{2 \rho \pi \delta p} \sin\left(\rho \frac{\pi}{2}\right) \Re_e[\bar{i}_{S\rho} e^{-j\rho\theta_s}] \quad (1.49)$$

By comparing (1.49) with (1.14) it is possible to achieve the following relevant relationships between the stator current space vectors and the stator magnetic field space vectors:

$$\bar{h}_{S\rho} = \frac{5 N_s K_{ws\rho}}{2 \pi \delta p} \frac{\sin\left(\rho \frac{\pi}{2}\right)}{\rho} \bar{i}_{S\rho} \quad (1.50)$$

Observing (1.50) it is important to underline that the  $\rho^{\text{th}}$  spatial harmonic of the magnetic field is produced by the  $\rho^{\text{th}}$  current space vector.

It is also possible to relate the spatial harmonics of the magnetic field to the stator current space vectors in the different planes and the zero-sequence component as follows:

- the harmonic fields with order: 5, 15, 25, 35 ... are stationary, with variable amplitude;
- the harmonic fields with order 1,11,21,31 ... rotate in the same direction of  $\bar{i}_{S1}$  with the same speed of  $\bar{i}_{S1}$  divided by  $\rho$ ;
- the harmonic fields with order 9,19,29,39 ... rotate in the opposite direction of  $\bar{i}_{S1}$  with the same speed of  $\bar{i}_{S1}$  divided by  $\rho$ ;
- the harmonic fields with order 3,13,23,33 ... rotate in the same direction of  $\bar{i}_{S3}$  with the same speed of  $\bar{i}_{S3}$  divided by  $\rho$ ;
- the harmonic fields with order 7,17,27,37 ... rotate in the opposite direction of  $\bar{i}_{S3}$  with the same speed of  $\bar{i}_{S3}$  divided by  $\rho$ .

### 1.5.1.2 Magnetic field produced by the rotor currents

Following the same procedure adopted to obtain the magnetic field produced by the stator windings, it is possible to obtain the following expression of the magnetic field produced by the rotor windings:

$$h_R(\theta_R, t) = \sum_{\rho \text{ odd}} \text{Re}[\bar{h}_{R\rho}^R(t)e^{-j\rho\theta_R}] \quad (1.51)$$

where:

$$\bar{h}_{R\rho}^R = \frac{5 N_R K_{wR\rho}}{2 \pi \delta p} \frac{\sin\left(\rho \frac{\pi}{2}\right)}{\rho} \bar{i}_{R\rho} \quad (1.52)$$

It should be noted that the magnetic field produced by the rotor currents is evaluated in the rotor reference frame.

The same observations made for the harmonic fields produced by the stator can be reformulated for the harmonic fields produced by the rotor.

### 1.5.1.3 Air gap magnetic field

Once the magnetic fields produced by the stator and rotor currents in the air gap have been determined, it is possible to obtain the total magnetic field in the air gap by summing the two contributions in the same reference frame, according to the following relationship:

$$\bar{h}_{T\rho}^S = \bar{h}_{S\rho} + \bar{h}_{R\rho} e^{j\rho\theta} \quad (1.53)$$

Substituting (1.50) and (1.52) into (1.53) leads to:

$$\bar{h}_{T\rho}^S = \frac{5 N_s K_{wS\rho}}{2 \pi \delta p} \frac{\sin\left(\rho \frac{\pi}{2}\right)}{\rho} \bar{i}_{S\rho} + \frac{5 N_R K_{wR\rho}}{2 \pi \delta p} \frac{\sin\left(\rho \frac{\pi}{2}\right)}{\rho} \bar{i}_{R\rho} e^{j\rho\theta} \quad (1.54)$$

## 1.5.2 Flux Linkages

In order to complete the mathematical model of the five-phase induction machine it is necessary to determine the expressions of the flux linkages with the stator and the rotor windings.

### 1.5.2.1 Flux linkage with a stator phase

Introducing (1.49) into (1.27), it is possible to obtain the following relationship:

$$\varphi_{STk} = \frac{\mu_0 N_S L \tau}{\pi} \sum_{\rho(\text{odd})=1}^{\infty} \frac{K_{wS\rho}}{\rho} (-1)^{\frac{\rho-1}{2}} \Re_e [\bar{h}_{T\rho}^S e^{-j\rho\psi_{SK}}] \quad (1.55)$$

where,  $\psi_{SK}$  assumes the values expressed in (1.56), owing to the symmetric distribution of the stator windings:

$$\psi_{SK} = \frac{2\pi}{5} (k - 1) \quad (1.56)$$

The total flux linkage with a generic phase  $k$  is the sum of the leakage flux and the flux due to the magnetic field in the air gap, as:

$$\varphi_{Sk} = \varphi_{Sdk} + \varphi_{STk} \quad k = 1, 2, \dots, 5 \quad (1.57)$$

where the leakage flux can be expressed in term of the stator leakage inductance  $L_{Sd}$  as:

$$\varphi_{Sdk} = L_{Sd} i_{Sk} \quad k = 1, 2, \dots, 5 \quad (1.58)$$

By applying the Clarke transformation to (1.57) leads to:

$$\bar{\varphi}_{S\rho} = \bar{\varphi}_{Sd\rho} + \bar{\varphi}_{ST\rho} \quad \rho = 1, 3. \quad (1.59)$$

$$\varphi_{S0} = \varphi_{Sd0} + \varphi_{ST0} \quad (1.60)$$

According to (1.55) and (1.58), by applying the Clarke transformation, the following relationships can be obtained:

$$\bar{\varphi}_{ST\rho} = \frac{N_S L \mu_0 \tau K_{wS\rho}}{\rho \pi} (-1)^{\frac{\rho-1}{2}} \bar{h}_{T\rho}^S \quad \rho = 0, 1, 3. \quad (1.61)$$

$$\bar{\varphi}_{Sd\rho} = L_{Sd} \bar{i}_{S\rho} \quad \rho = 0, 1, 3. \quad (1.62)$$

From the previous relationships it is possible to define some relevant magnetic parameters of the machine in the different planes, which are the stator self-inductance  $L_{SS\rho}$ , and the mutual inductance  $M_\rho$ . Introducing (1.54) into (1.61) it is possible to obtain

$$\bar{\varphi}_{ST\rho} = \frac{5L\mu_0\tau K_{wS\rho}^2 N_S^2}{2\pi^2\delta p} \bar{i}_{S\rho} + \frac{5L\mu_0\tau N_S K_{wS\rho} N_R K_{wR\rho}}{2\pi^2\delta p} \bar{i}_{R\rho} e^{j\rho\theta} \quad (1.63)$$

where

$$L_{SS\rho} = \frac{5L\mu_0\tau K_{wS\rho}^2 N_S^2}{2\pi^2\delta p} \quad (1.64)$$

$$M_\rho = \frac{5L\mu_0\tau N_S K_{wS\rho} N_R K_{wR\rho}}{2\pi^2\delta p} \quad (1.65)$$

The stator inductance is the sum of the self-inductance  $L_{SS\rho}$  and the leakage inductance  $L_{sd}$ :

$$L_{S\rho} = L_{sd} + L_{SS\rho} \quad (1.66)$$

### 1.5.2.2 Flux linkage with a rotor phase

The expression of the flux linkage with a rotor phase can be derived following the same steps carried out for the stator phases.

The following relationships can be achieved:

$$\bar{\varphi}_{R\rho} = \bar{\varphi}_{Rd\rho} + \bar{\varphi}_{RT\rho} \quad \rho = 1, 3. \quad (1.67)$$

$$\varphi_{R0} = \varphi_{Rd0} + \varphi_{RT0} \quad (1.68)$$

where:

$$\bar{\varphi}_{RT\rho} = \frac{N_R L \mu_0 \tau K_{wR\rho}}{\pi \rho} (-1)^{\frac{\rho-1}{2}} \bar{h}_{T\rho}^R \quad (1.69)$$

$$\bar{\varphi}_{Rd\rho} = L_{Rd} \bar{i}_{R\rho} \quad \rho = 0, 1, 3. \quad (1.70)$$

From the previous relationships it is possible to define some relevant magnetic parameters of the machine in the different planes, which are the stator self-inductance  $L_{S\rho}$ , the rotor self-inductance  $L_{R\rho}$  and the mutual inductance  $M_\rho$ .

Introducing (1.54) expressed in the rotor reference frame into (1.69) it is possible to define the self-inductance  $L_{RR\rho}$ , and the mutual inductance  $M_\rho$  of the rotor.

$$\bar{\varphi}_{RT\rho} = \frac{5L\mu_0\tau}{2\pi^2\delta p} \frac{N_S K_{wS\rho} N_R K_{wR\rho}}{\rho^2} \bar{i}_{S\rho} e^{-j\rho\theta} + \frac{5L\mu_0\tau K_{wR\rho}^2 N_R^2}{2\pi^2\delta p} \frac{1}{\rho^2} \bar{i}_{R\rho} \quad (1.71)$$

where

$$L_{RR\rho} = \frac{5L\mu_0\tau K_{wR\rho}^2 N_R^2}{2\pi^2\delta p} \frac{1}{\rho^2} \quad (1.72)$$

The rotor inductance is the sum of the self-inductance  $L_{RR\rho}$  and the leakage inductance  $L_{Rd}$ :

$$L_{R\rho} = L_{Rd} + L_{RR\rho} \quad (1.73)$$

### 1.5.3 Electromagnetic Torque

Starting by (1.35) and introducing the expressions of the magnetic field generated by stator (1.50) and rotor (1.52) currents, it is possible to express the electromagnetic torque as:

$$T_{em} = \mu_0 p^2 \delta L \tau \sum_{\rho \text{ odd}} \rho \left[ \frac{5K_{wS\rho} N_S}{2\pi\delta} \frac{\sin\left(\frac{\rho\pi}{2}\right)}{\rho} \bar{i}_{S\rho} \cdot j \frac{5K_{wR\rho} N_R}{2\pi\delta} \frac{\sin\left(\frac{\rho\pi}{2}\right)}{\rho} \bar{i}_{R\rho} e^{j\rho\theta} \right] \quad (1.74)$$

$$T_{em} = p^2 \sum_{\rho \text{ odd}} \frac{25N_S K_{wS\rho} N_R K_{wR\rho} L \tau \mu_0}{4\pi^2 \delta} \rho [\bar{i}_{S\rho} \cdot j \bar{i}_{R\rho} e^{j\rho\theta}] \quad (1.75)$$

Observing that the torque contributions are inversely proportional to the square of  $\rho$ , in (1.75) it is possible to take into account only the torque contributions due to the first and the third spatial harmonics of the magnetic field in the air gap, which are the most relevant, obtaining a good approximation. The (1.75) can be simplified as follows:

$$T_{em} = \frac{5}{2} p M_1 [\bar{i}_{S1} \cdot j \bar{i}_{R1} e^{j\theta}] + \frac{15}{2} p M_3 [\bar{i}_{S3} \cdot j \bar{i}_{R3} e^{j3\theta}] \quad (1.76)$$

### 1.5.4 Summary of the Mathematical Model of the five-Phase Wound-Rotor Induction Machines

The mathematical model of the five-phase wound-rotor induction machine, previously determined, expressed in terms of space vectors and zero-sequence components, is summarized hereafter. Note that, the model takes into account up to the third spatial harmonic of the magnetic field in the air gap.

$$V_{S0} = R_S i_{S0} + \frac{d\varphi_{S0}}{dt} \quad (1.77)$$

$$0 = R_R i_{R0} + \frac{d\varphi_{R0}}{dt} \quad (1.78)$$

$$\varphi_{S0} = L_{S5} i_{S0} + M_5 i_{R0} e^{j\theta} \quad (1.79)$$

$$\varphi_{R0} = L_{R5} i_{R0} + M_5 i_{S0} e^{-j\theta} \quad (1.80)$$

$$\bar{V}_{S1} = R_S \bar{i}_{S1} + \frac{d\bar{\varphi}_{S1}}{dt} \quad (1.81)$$

$$0 = R_R \bar{i}_{R1} + \frac{d\bar{\varphi}_{R1}}{dt} \quad (1.82)$$

$$\bar{\varphi}_{S1} = L_{S1} \bar{i}_{S1} + M_1 \bar{i}_{R1} e^{j\theta} \quad (1.83)$$

$$\bar{\varphi}_{R1} = L_{R1} \bar{i}_{R1} + M_1 \bar{i}_{S1} e^{-j\theta} \quad (1.84)$$

$$\bar{V}_{S3} = R_S \bar{i}_{S3} + \frac{d\bar{\varphi}_{S3}}{dt} \quad (1.85)$$

$$0 = R_R \bar{i}_{R3} + \frac{d\bar{\varphi}_{R3}}{dt} \quad (1.86)$$

$$\bar{\varphi}_{S3} = L_{S3} \bar{i}_{S3} + M_3 \bar{i}_{R3} e^{j3\theta} \quad (1.87)$$

$$\bar{\varphi}_{R3} = L_{R3} \bar{i}_{R3} + M_3 \bar{i}_{S3} e^{-j3\theta} \quad (1.88)$$

$$T_{em} = \frac{5}{2} p M_1 [\bar{i}_{S1} \cdot j \bar{i}_{R1} e^{j\theta}] + \frac{15}{2} p M_3 [\bar{i}_{S3} \cdot j \bar{i}_{R3} e^{j3\theta}] \quad (1.89)$$

## 1.6 Model of Six-Phase Permanent Magnet Synchronous Machines

The system analysed in this section is a six-phase synchronous machine with an asymmetrical winding distribution and surface-mounted permanent magnets NdFeB grade 33 on the rotor. In the stator slots there are two independent three-phase windings rotated by  $30^\circ$  electrical degrees relative to each other, as shown in Fig. 1.6. The rotation of  $30^\circ$  electrical degrees of the two stator coil sets leads to a harmonic reduction and improves the quality of the magnetic field in the air gap.

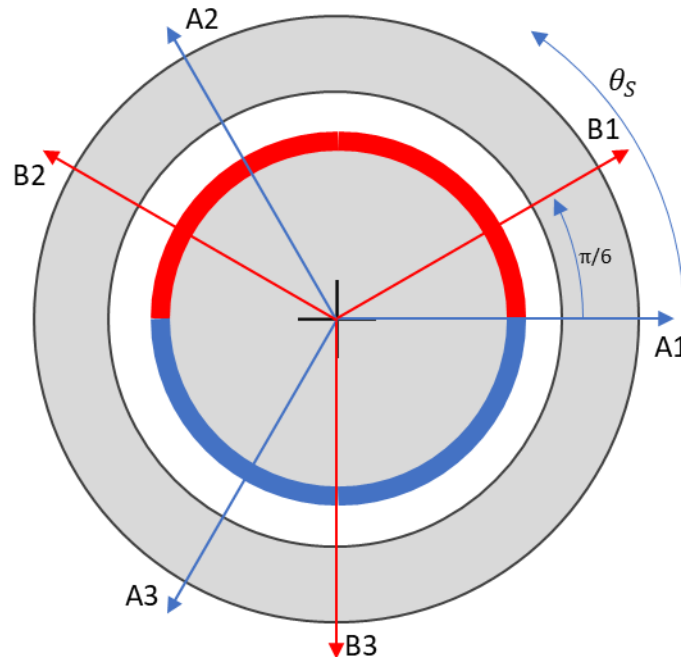


Figure 1.6 Equivalent representation by using electric angles of a cross-section of a Six-Phase Permanent Magnet Synchronous Machine.

Initially the model will be developed taking into account all the spatial harmonics of the magnetic field in the air gap, but, afterward, the analysis will be limited up to the  $11^{th}$  one.

### 1.6.1 Magnetic Field

The total magnetic field in the air gap has two contributions, the first one is produced by the currents that flow through to the stator windings, and the other one is produced by the permanent magnets on the rotor. The total magnetic field in the air gap can be obtained as the sum of the two contributions by neglecting the non-linearities of the magnetic materials according to the previous hypothesis.

Generally, the rotor can have two different types of magnets which differ for the kind of magnetization they have. The magnetization can have radial or parallel direction, as can be seen in Fig. 1.7. These two kinds of magnetization produce different space harmonics in the air gap.

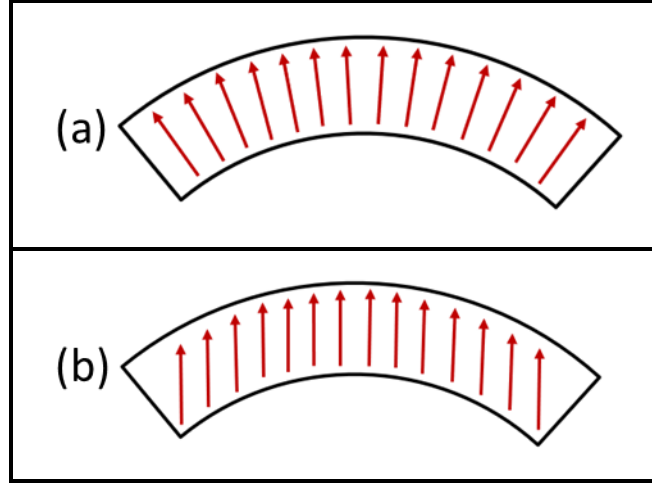


Figure 1.7 Representation of different kinds of magnetization of the permanent magnets, (a) radial magnetization, (b) parallel magnetization.

The machine that will be adopted for the experimental tests has parallel magnetization and the model is developed for this type of magnets. The two contributions, stator and rotor, will be studied separately and, after that, they will be summed to obtain the total magnetic field in the air gap of the machine.

#### 1.6.1.1 Magnetic field produced by the stator

According to (1.13), by summing the six contributions of every single phase, it is possible to obtain the expression of the magnetic field produced by the stator windings for the six-phase machine under study.

According with Fig. 1.6, the quantities  $\psi_{Sk}$ , which identify the position of the magnetic axes of the stator windings, assume the following values:  $0, \frac{\pi}{6}, \frac{4\pi}{6}, \frac{5\pi}{6}, \frac{8\pi}{6}, \frac{9\pi}{6}$  respectively for the phases A1, B1, A2, B2, A3, and B3.

By substituting their values in (1.14), allows to write:

$$h_s(\theta_s, t) = \sum_{\rho \text{ odd}} \frac{N_s K_{ws} \rho}{\pi \delta p \rho} \sin\left(\rho \frac{\pi}{2}\right) \text{Re} \left[ e^{-j\rho\theta_s} \left( i_{SA1} + i_{SB1} e^{j\frac{\pi\rho}{6}} + i_{SA2} e^{j\frac{4\pi\rho}{6}} \right. \right. \\ \left. \left. + i_{SB2} e^{j\frac{5\pi\rho}{6}} + i_{SA3} e^{j\frac{8\pi\rho}{6}} + i_{SB3} e^{j\frac{9\pi\rho}{6}} \right) \right] \quad (1.90)$$

Introducing the complex constant  $\bar{\alpha}_6 = e^{\frac{j\pi}{6}}$ , it is possible to rewrite (1.90) as follows:

$$h_s(\theta_s, t) = \sum_{\rho(\text{odd})=1}^{\infty} \frac{N_s K_{ws} \rho}{\rho \pi \delta p} \sin\left(\rho \frac{\pi}{2}\right) \Re_e \left[ \left( i_{SA1} + i_{SB1} \bar{\alpha}_6^\rho + i_{SA2} \bar{\alpha}_6^{4\rho} + i_{SB2} \bar{\alpha}_6^{5\rho} \right. \right. \\ \left. \left. + i_{SA3} \bar{\alpha}_6^{8\rho} + i_{SB3} \bar{\alpha}_6^{9\rho} \right) e^{-j\rho\theta_s} \right] \quad (1.91)$$

Equation (1.91) suggests defining new complex variable (multiple space vectors), useful to represent both the evolution of the six stator currents and of the magnetic field in the air gap, by means of a specific Clarke transformation as follows:

$$\bar{i}_{S\rho} = \frac{1}{3} (i_{SA1} + i_{SB1} \bar{\alpha}_6^\rho + i_{SA2} \bar{\alpha}_6^{4\rho} + i_{SB2} \bar{\alpha}_6^{5\rho} + i_{SA3} \bar{\alpha}_6^{8\rho} + i_{SB3} \bar{\alpha}_6^{9\rho}) \quad (1.92)$$

In (1.92),  $\rho$  can assume all the odd integer values, but it is trivial to demonstrate that only the three complex variables obtained for  $\rho = 1, 3$  and  $5$  are independent. Verification of how the space vectors  $1, 3$ , and  $5$  can lead back to all the possible combinations of  $\rho$  is shown in the following:

$$\bar{i}_{S1} = \bar{i}_{S\rho} \quad \text{for } \rho = 1, 13, 25, \dots \quad (1.93)$$

$$\bar{i}_{S3} = \bar{i}_{S\rho} \quad \text{for } \rho = 3, 15, 27, \dots \quad (1.94)$$

$$\bar{i}_{S5} = \bar{i}_{S\rho} \quad \text{for } \rho = 5, 17, 29, \dots \quad (1.95)$$

$$\bar{i}_{S5}^* = \bar{i}_{S\rho} \quad \text{for } \rho = 7, 19, 31, \dots \quad (1.96)$$

$$\bar{i}_{S3}^* = \bar{i}_{S\rho} \quad \text{for } \rho = 9, 21, 33, \dots \quad (1.97)$$

$$\bar{i}_{S1}^* = \bar{i}_{S\rho} \quad \text{for } \rho = 11, 23, 35, \dots \quad (1.98)$$

Therefore, (1.92) can be explicitly rewritten as:

$$\bar{i}_{S1} = \frac{1}{3} (i_{SA1} + i_{SB1} \bar{\alpha}_6^1 + i_{SA2} \bar{\alpha}_6^4 + i_{SB2} \bar{\alpha}_6^5 + i_{SA3} \bar{\alpha}_6^8 + i_{SB3} \bar{\alpha}_6^9) \quad (1.99)$$

$$\bar{i}_{S3} = \frac{1}{3} (i_{SA1} + i_{SB1} \bar{\alpha}_6^3 + i_{SA2} + i_{SB2} \bar{\alpha}_6^3 + i_{SA3} + i_{SB3} \bar{\alpha}_6^3) \quad (1.100)$$

$$\bar{i}_{S5} = \frac{1}{3} (i_{SA1} + i_{SB1} \bar{\alpha}_6^5 + i_{SA2} \bar{\alpha}_6^8 + i_{SB2} \bar{\alpha}_6^1 + i_{SA3} \bar{\alpha}_6^4 + i_{SB3} \bar{\alpha}_6^9) \quad (1.101)$$

It should be noted that,  $\bar{i}_{S1}$ ,  $\bar{i}_{S3}$  and  $\bar{i}_{S5}$ , called space vectors in the  $\alpha_1 - \beta_1$  plane, in the  $\alpha_3 - \beta_3$  plane, and in the  $\alpha_3 - \beta_3$  plane, respectively, are complex quantities. As can be seen, the number of degrees of freedom of the new variables is equivalent to the number of degrees of freedom of the six stator currents, confirming the correctness of the adopted Clarke transformation.

It can be demonstrated that the corresponding inverse transformation is [34]:

$$\begin{aligned}
 i_{SA1} &= \bar{i}_{S1} \cdot \bar{\alpha}_6^0 + \bar{i}_{S3} \cdot \bar{\alpha}_6^0 + \bar{i}_{S5} \cdot \bar{\alpha}_6^0 \\
 i_{SB1} &= \bar{i}_{S1} \cdot \bar{\alpha}_6^1 + \bar{i}_{S3} \cdot \bar{\alpha}_6^3 + \bar{i}_{S5} \cdot \bar{\alpha}_6^5 \\
 i_{SA2} &= \bar{i}_{S1} \cdot \bar{\alpha}_6^4 + \bar{i}_{S3} \cdot \bar{\alpha}_6^0 + \bar{i}_{S5} \cdot \bar{\alpha}_6^8 \\
 i_{SB2} &= \bar{i}_{S1} \cdot \bar{\alpha}_6^5 + \bar{i}_{S3} \cdot \bar{\alpha}_6^3 + \bar{i}_{S5} \cdot \bar{\alpha}_6^1 \\
 i_{SA3} &= \bar{i}_{S1} \cdot \bar{\alpha}_6^8 + \bar{i}_{S3} \cdot \bar{\alpha}_6^0 + \bar{i}_{S5} \cdot \bar{\alpha}_6^4 \\
 i_{SB3} &= \bar{i}_{S1} \cdot \bar{\alpha}_6^9 + \bar{i}_{S3} \cdot \bar{\alpha}_6^3 + \bar{i}_{S5} \cdot \bar{\alpha}_6^9
 \end{aligned} \tag{1.102}$$

Introducing (1.92) in (1.91) gives:

$$h_S(\theta_S, t) = \sum_{\rho(\text{odd})=1}^{\infty} 3 \frac{N_s K_{ws\rho}}{\rho \pi \delta p} \sin\left(\rho \frac{\pi}{2}\right) \Re_e[\bar{i}_{S\rho} e^{-j\rho\theta_S}] \tag{1.103}$$

By comparing (1.103) with (1.13) it is possible to achieve the following relevant relationships between the stator current space vectors and the stator magnetic field space vectors:

$$\bar{h}_{S\rho} = 3 \frac{N_s K_{ws\rho}}{\pi \delta p} \frac{\sin\left(\rho \frac{\pi}{2}\right)}{\rho} \bar{i}_{S\rho} \tag{1.104}$$

Observing (1.104) it is important to underline that the  $\rho^{th}$  harmonic of the magnetic field is produced by the  $\rho^{th}$  current space vector.

### 1.6.1.2 Magnetic field produced by the rotor magnets

Let us consider a generic representation of one pole pair of the rotor magnets, arranged as shown in Fig. 1.7 where the angles are in electrical degrees. In healthy conditions, the angles  $\gamma_1$  and  $\gamma_2$  are equal, whereas they can be different under demagnetization of the magnet edges. The origin of the rotor reference frame is independent of the magnet status and is positioned in the middle of the magnet in the left side, in the case  $\gamma_1 = \gamma_2$ .

The following linear characteristic of the magnet is assumed hereafter:

$$b_m = \mu_d h_m + B_R \tag{1.105}$$

where  $B_R$  is the residual flux density of the magnetic material and,  $\mu_d$  is the differential permeability assumed equivalent to the permeability of free space to analyse the machine as isotropic.

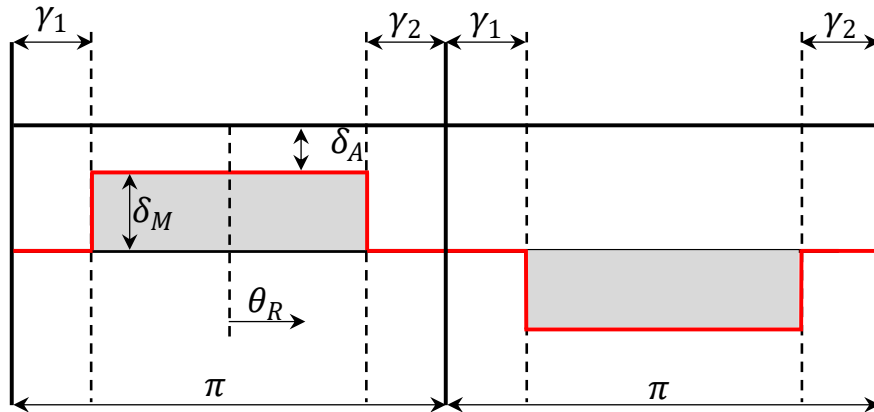


Figure 1.8 Graphical representation of the geometry of the rotor magnets in electrical degrees.

In agreement with the assumption of parallel magnetization, the distribution of the magnetic field in the air gap produced by the rotor magnets of a machine with two poles, is represented in Fig. 1.9 [35]-[37]. According to previous assumptions, both in case of healthy or demagnetized magnets, the peak of the magnetic field takes place in the origin of the rotor reference frame.

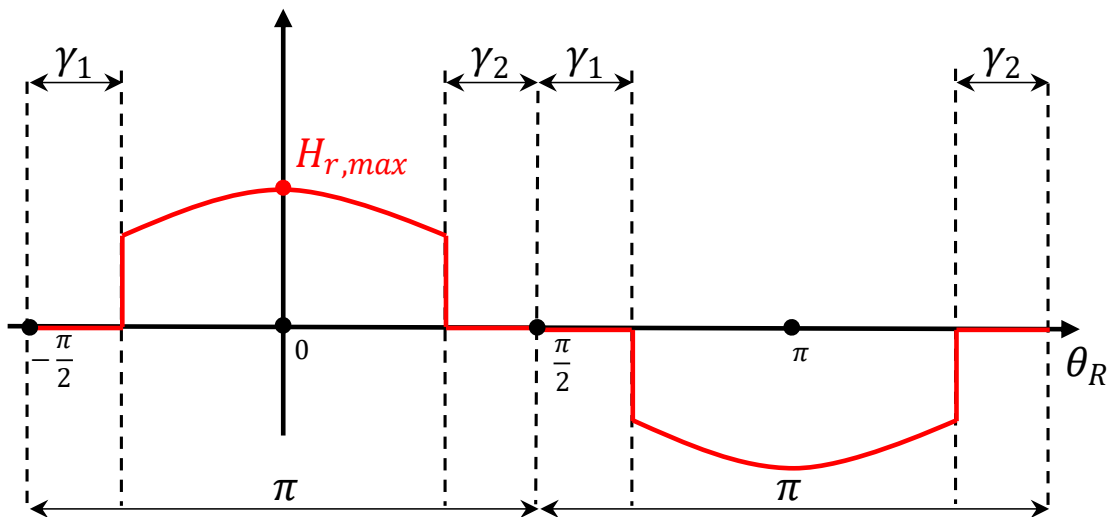


Figure 1.9 Distribution of the radial component of the magnetic field produced by magnets with parallel magnetization.

From the divergence theorem and Ampère's circuital law it is easy to obtain the following expression of the maximum value of the magnetic field, that corresponds to the value of the magnetic field at the origin of the rotor reference frame.

$$H_{r,max} = B_R \left( \frac{\delta_M}{\mu_0 \delta_M + \mu_d \delta_A} \right) \quad (1.106)$$

For a machine with an arbitrary number of pole pairs, it is possible to describe the waveform of the magnetic field produced by the rotor magnets with a parallel magnetization as:

$$h(\theta) = \begin{cases} H_{r,max} \cos\left(\frac{\theta_R}{p}\right) & -\frac{\pi}{2} + \gamma_1 < \theta_R < \frac{\pi}{2} - \gamma_2 \\ H_{r,max} \cos\left(\frac{\theta_R + (p-1)\pi}{p}\right) & \frac{\pi}{2} + \gamma_1 < \theta_R < \pi \\ H_{r,max} \cos\left(\frac{\theta_R - (p-1)\pi}{p}\right) & \pi < \theta_R < -\frac{\pi}{2} - \gamma_2 \\ 0 & \text{Otherwise} \end{cases} \quad (1.107)$$

where  $\theta_R$  is the electrical angular coordinate and  $p$  is the number of pole pairs of the rotor.

Applying the Fourier expansion to the magnetic field produced by the rotor it is possible to emphasize its spatial harmonic content, in the rotor reference frame. The basic relations are the following:

$$h_R(\theta_R, t) = h_0 + \sum_{\rho=1}^{\infty} \Re_e[\bar{h}_{R\rho} e^{-j\rho\theta_R}] \quad (1.108)$$

$$h_0 = \frac{1}{2\pi} \int_{-\pi}^{\pi} h_R(\theta_R, t) d\theta_R \quad (1.109)$$

$$\bar{h}_{R\rho} = \frac{1}{\pi} \int_{-\pi}^{\pi} h_R(\theta_R, t) e^{j\rho\theta_R} d\theta_R \quad (1.110)$$

A non-zero component  $h_0$  would give rise to a magnetic flux across a closed surface at the air gap different from zero. This would violate the divergence law. Hence the law of divergence ensures that the  $h_0$  component is zero.

Taking (1.107) into account, by observing the periodicity of magnetic field represented in Fig. 1.9, the quantity  $\bar{h}_{R\rho}$  can be evaluated in the range as:

$$\bar{h}_{R\rho} = H_{r,max} \frac{2}{\pi} \int_{-\frac{\pi}{2} + \gamma_1}^{\frac{\pi}{2} - \gamma_2} \cos\left(\frac{\theta_R}{p}\right) e^{-j\rho\theta_R} d\theta_R \quad (1.111)$$

The integral term can be expressed as follows:

$$\int \cos\left(\frac{\theta_R}{p}\right) e^{-j\rho\theta_R} d\theta_R = \frac{p}{\rho^2 p^2 - 1} e^{-j\rho\theta_R} \left[ j\rho p \cos\left(\frac{\theta_R}{p}\right) - \sin\left(\frac{\theta_R}{p}\right) \right] \quad (1.112)$$

Substituting (1.112) in (1.111) leads to

$$\bar{h}_{R\rho} = 2 \frac{H_{r,max}}{\pi} \frac{p}{\rho^2 p^2 - 1} \left\{ \left[ j p \rho \cos\left(\frac{\pi}{2} - \gamma_2\right) - \sin\left(\frac{\pi}{2} - \gamma_2\right) \right] e^{-j\rho\left(\frac{\pi}{2} - \gamma_2\right)} \right. \\ \left. - \left[ j p \rho \cos\left(\frac{-\pi}{2} + \gamma_1\right) - \sin\left(\frac{-\pi}{2} + \gamma_1\right) \right] e^{-j\rho\left(\frac{-\pi}{2} + \gamma_1\right)} \right\} \quad (1.113)$$

It is possible to compact (1.113) by isolating the expression (1.114) that concerns the geometrical shape and the kind of magnetization of the magnets.

$$f(\gamma_1, \gamma_2, \rho, p) = \frac{p}{\rho^2 p^2 - 1} \left[ j p \rho \cos\left(\frac{\pi}{2} - \gamma_2\right) - \sin\left(\frac{\pi}{2} - \gamma_2\right) \right] e^{-j\rho\left(\frac{\pi}{2} - \gamma_2\right)} \\ - \frac{p}{\rho^2 p^2 - 1} \left[ j p \rho \cos\left(\frac{-\pi}{2} + \gamma_1\right) - \sin\left(\frac{-\pi}{2} + \gamma_1\right) \right] e^{-j\rho\left(\frac{-\pi}{2} + \gamma_1\right)} \quad (1.114)$$

The expression (1.114) represents the form factor of the magnet that takes into account its arc length.

Equation (1.113) can be rewritten as:

$$\bar{h}_{R\rho} = 2 \frac{H_{r,max}}{\rho\pi} (-1)^{\frac{\rho-1}{2}} f(\gamma_1, \gamma_2, \rho, p) \quad (1.115)$$

### 1.6.1.3 Air gap magnetic field

Once the magnetic fields produced by stator windings and rotor magnets in the air gap have been determined, it is possible to obtain the entire magnetic field by summing the two contributions as follows:

$$\bar{h}_{T\rho}^S = \bar{h}_{S\rho} + \bar{h}_{R\rho} e^{j\rho\theta} \quad (1.116)$$

Replacing (1.104) and (1.115) in (1.116), it is possible to write the following relationship:

$$\bar{h}_{T\rho}^S = \frac{3 N_S K_{ws\rho}}{\rho\pi\delta p} (-1)^{\frac{\rho-1}{2}} \bar{i}_{S\rho} + 2 \frac{H_{r,max}}{\rho\pi} (-1)^{\frac{\rho-1}{2}} f(\gamma_1, \gamma_2, \rho, p) e^{j\rho\theta} \quad (1.117)$$

### 1.6.2 Flux Linkages

Once the spatial distribution of the magnetic field produced by the stator currents and the rotor magnets is known, it is possible to derive the expression of the flux linkages with the stator phases. In order to facilitate understanding of the followed process, the study of the flux linkages will be split into two sections.

Firstly, the fluxes linkage due to the air gap magnetic field will be analysed, and then, the leakage fluxes will be evaluated. After that, the two contributions will be summed to determine the total flux linkages.

#### 1.6.2.1 Flux linkages due to the air gap magnetic field

Repeating the same procedure already carried out for the five phase induction machine, it is possible to write the expression of the flux linkage with the generic  $k$ -th stator phase:

$$\varphi_{STk} = \frac{\mu_0 N_S L \tau}{\pi} \sum_{h(\text{odd})=1}^{\infty} \frac{K_{wSh}}{h} (-1)^{\frac{h-1}{2}} \Re_e [\bar{h}_{Th}^S e^{-j\rho\psi_{SK}}] \quad (1.118)$$

Using the definitions of space vectors, it is possible to obtain the three space vectors of the flux linkages due to the air gap magnetic field, as follows:

$$\bar{\varphi}_{ST\rho} = \frac{1}{3} [\varphi_{STA1} + \varphi_{STB1} \bar{\alpha}_6^\rho + \varphi_{STA2} \bar{\alpha}_6^{4\rho} + \varphi_{STB2} \bar{\alpha}_6^{5\rho} + \varphi_{STA3} \bar{\alpha}_6^{8\rho} + \varphi_{STB3} \bar{\alpha}_6^{9\rho}] \quad (1.119)$$

where  $\rho = 1, 3, 5$ .

After some mathematical passages, that is introducing (1.118) into (1.119) with their relative value of  $\psi_{SK}$ , in terms of  $\bar{\alpha}_6$  and using the following Eulero trigonometric relation:

$$\Re_e[\bar{x}] = \frac{[\bar{x} + \bar{x}^*]}{2} \quad (1.120)$$

it is possible to rewrite the space vectors of the flux linkages due to the air gap magnetic field, as follows:

$$\bar{\varphi}_{ST\rho} = \frac{\mu_0 N_S L \tau}{\pi} \sum_{h=\rho \pm 12N}^{\infty} \frac{K_{wSh}}{h} (-1)^{\frac{h-1}{2}} \bar{h}_{Th}^S + \frac{\mu_0 N_S L \tau}{\pi} \sum_{h=-\rho \pm 12N}^{\infty} \frac{K_{wSh}}{h} (-1)^{\frac{h-1}{2}} \bar{h}_{Th}^{S*} \quad (1.121)$$

where,  $\rho$  is the order of the space vector and  $h$  is the spatial harmonic index of the flux linkage.

### 1.6.2.2 Leakage fluxes

The space vectors of the leakage fluxes can be calculated as follows:

$$\bar{\varphi}_{Sd\rho} = L_{Sd\rho} \bar{i}_{S\rho} \quad (1.122)$$

where  $L_{Sd\rho}$  is the stator leakage inductance in the  $\rho^{\text{th}}$   $\alpha - \beta$  planes. The values are function of the geometrical characteristics of the stator slots and of the type of winding.

### 1.6.2.3 Total flux linkages

The space vectors of the total flux linkage can be determined as the sum of the two contributions, the leakage flux  $\bar{\varphi}_{Sd\rho}$  and the air gap flux linkage  $\bar{\varphi}_{ST\rho}$ :

$$\bar{\varphi}_{S\rho} = \bar{\varphi}_{Sd\rho} + \bar{\varphi}_{ST\rho} \quad (1.123)$$

Introducing (1.122) and (1.121) in (1.123), and taking (1.117) into account, leads to:

$$\begin{aligned} \bar{\varphi}_{S\rho} = & L_{Sd\rho} \bar{i}_{S\rho} \\ & + \sum_{h=\rho\pm 12N}^{\infty} \frac{3\mu_0 N_S^2 L\tau}{\pi^2 \delta p} \frac{K_{wSh}^2}{h^2} \bar{i}_{S\rho} \\ & + \sum_{h=\rho\pm 12N}^{\infty} \frac{2\mu_0 N_S L\tau}{\pi^2} \frac{K_{wSh} H_{r,max}}{h^2} f(\gamma_1, \gamma_2, \rho, p) e^{j\rho\theta} \\ & + \sum_{h=-\rho\pm 12N}^{\infty} \frac{3\mu_0 N_S^2 L\tau}{\pi^2 \delta p} \frac{K_{wSh}^2}{h^2} \bar{i}_{S\rho} \\ & + \sum_{h=-\rho\pm 12N}^{\infty} \frac{2\mu_0 N_S L\tau}{\pi^2} \frac{K_{wSh} H_{r,max}}{h^2} f(\gamma_1, \gamma_2, \rho, p)^* e^{-j\rho\theta} \end{aligned} \quad (1.124)$$

To compact the size of (1.124) it is useful to define the synchronous inductance  $L_{S\rho}$  in the different planes as in (1.125):

$$L_{S\rho} = L_{Sd\rho} + \sum_{\rho=h\pm 12N}^{\infty} \frac{3\mu_0 N_S^2 L\tau}{\pi^2 \delta P} \frac{K_{wS\rho}^2}{\rho^2} + \sum_{\rho=-h\pm 12N}^{\infty} \frac{3\mu_0 N_S^2 L\tau}{\pi^2 \delta P} \frac{K_{wS\rho}^2}{\rho^2} \quad (1.125)$$

Furthermore, for the same reason, the following constants are introduced:

$$\varphi_{M\rho} = \frac{2\mu_0 N_S L\tau}{\pi^2} \frac{H_{R,max}}{\rho^2} K_{wS\rho} \quad (1.126)$$

Introducing (1.125) and (1.126) into the expressions of the total flux linkages (1.123), and considering (1.126), leads to:

$$\begin{aligned} \bar{\varphi}_{S\rho} = L_{S\rho} \bar{i}_{S\rho} + \sum_{\rho=h\pm 12N}^{\infty} \varphi_{M\rho} f(\gamma_1, \gamma_2, \rho, p) e^{j\rho\theta} + \\ + \sum_{\rho=-h\pm 12N}^{\infty} \varphi_{M\rho} f(\gamma_1, \gamma_2, \rho, p)^* e^{-j\rho\theta} \end{aligned} \quad (1.127)$$

### 1.6.3 Electromagnetic Torque

As already demonstrated in this chapter, the electromagnetic torque can be expressed as:

$$T_{em} = \mu_0 P^2 \delta L \tau \sum_{\rho(\text{odd})=1}^{\infty} \rho [\bar{h}_{S\rho}^S \cdot j \bar{h}_{R\rho}^S] \quad (1.128)$$

Limiting the analysis up to the eleventh spatial harmonic of the magnetic field in the air gap and introducing (1.113) and (1.104) in (1.128), the following torque expression can be found:

$$T_{em} = \sum_{\rho=1,3,5}^{11} T_{em\rho} \quad (1.129)$$

where:

$$T_{em\rho} = 3p\varphi_{M\rho} \rho [\bar{i}_{S\rho} \cdot j f(\gamma_1, \gamma_2, \rho, p) e^{j\rho\theta}] \quad (1.130)$$

It should be noted that, in six-phase systems, the space vectors in the plane  $\alpha_3 - \beta_3$  are related to the zero-sequence components of the two three-phase stator windings. Since the attention is focused on a six-phase machine with two separated neutral points, the equations concerning space vectors in the plane  $\alpha_3 - \beta_3$  can be omitted.

### 1.6.4 Summary of the Mathematical Model of the Six-Phase Permanent Magnet Synchronous Machines

The mathematical model of the asymmetrical six-phase permanent magnet synchronous machine, previously determined, expressed in terms of space vectors, is summarized hereafter. Note that, the model takes into account up to the eleventh spatial harmonic of the magnetic field in the air gap.

$$\bar{V}_{S1} = R_S \bar{i}_{S1} + \frac{d\bar{\varphi}_{S1}}{dt} \quad (1.131)$$

$$\bar{\varphi}_{S1} = L_{S1} \bar{i}_{S1} + \varphi_{M1} f(\gamma_1, \gamma_2, 1, p) e^{j\theta} + \varphi_{M11} f(\gamma_1, \gamma_2, 11, p) e^{-j11\theta} \quad (1.132)$$

$$\varphi_{M1} = \frac{2 \mu_0 N_S L \tau K_{wS1} H_{R,max}}{\pi^2} \quad (1.133)$$

$$H_{r,max} = B_R \left( \frac{\delta_M}{\mu_0 \delta_M + \mu_d \delta_A} \right) \quad (1.134)$$

$$\bar{V}_{S3} = R_S \bar{i}_{S3} + \frac{d\bar{\varphi}_{S3}}{dt} \quad (1.135)$$

$$\bar{\varphi}_{S3} = L_{S3} \bar{i}_{S3} + \varphi_{M3} f(\gamma_1, \gamma_2, 3, p) e^{j3\theta} + \varphi_{M9} f(\gamma_1, \gamma_2, 9, p) e^{-j9\theta} \quad (1.136)$$

$$\varphi_{M3} = \frac{2 \mu_0 N_S L \tau H_{R,max} K_{wS3}}{\pi^2 3^2} \quad (1.137)$$

$$\bar{V}_{S5} = R_S \bar{i}_{S5} + \frac{d\bar{\varphi}_{S5}}{dt} \quad (1.138)$$

$$\bar{\varphi}_{S5} = L_{S5} \bar{i}_{S5} + \varphi_{M5} f(\gamma_1, \gamma_2, 5, p) e^{j5\theta} + \varphi_{M7} f(\gamma_1, \gamma_2, 7, p) e^{-j7\theta} \quad (1.139)$$

$$\varphi_{M5} = \frac{2 \mu_0 N_S L \tau H_{R,max} K_{wS5}}{\pi^2 5^2} \quad (1.140)$$

$$\begin{aligned} C_{em} = 3p \{ & \varphi_{M1} [\bar{i}_{S1} \cdot j f(\gamma_1, \gamma_2, 1, p) e^{j\theta}] + 3\varphi_{M3} [\bar{i}_{S3} \cdot j f(\gamma_1, \gamma_2, 3, p) e^{j3\theta}] \\ & + 5\varphi_{M5} [\bar{i}_{S5} \cdot j f(\gamma_1, \gamma_2, 5, p) e^{j5\theta}] + 7\varphi_{M7} [\bar{i}_{S5}^* \cdot j f(\gamma_1, \gamma_2, 7, p) e^{j7\theta}] \\ & + 9\varphi_{M9} [\bar{i}_{S3}^* \cdot j f(\gamma_1, \gamma_2, 9, p) e^{j9\theta}] \\ & + 11\varphi_{M11} [\bar{i}_{S1}^* \cdot j f(\gamma_1, \gamma_2, 11, p) e^{j11\theta}] \} \end{aligned} \quad (1.141)$$



## Chapter 2

# *Voltage Balancing of the DC-Link Capacitors in Three-Level T-Type Multi-phase Inverters*

*In this chapter the capacitor voltage-balancing for five-phase T-type inverters, is analysed. A new PWM strategy able to balance the neutral-point voltage in multi-phase inverters is proposed.*

*The proposed technique, in many operating conditions, cancels the voltage oscillation of the DC-link capacitors, allowing the DC link voltage to be constant in every cycle. This aspect has two important benefits. Firstly, the inverter can satisfy the voltage request. Secondly, the voltage stress on the capacitors is reduced, leading to an increased lifetime of the capacitors.*

*A closed-loop capacitor voltage balancing control technique is presented. It is based on a precise calculation of the zero-sequence component of the modulating signals, according to the neutral-point current command for T-type NPC multi-phase inverter, and works properly for any multi-phase system with an odd number of star-connected phases.*

*The proposed strategy makes it possible to keep the DC-link capacitors under control at any reference value and in any operating condition, even during open phase faults and with not-sinusoidal output currents. This solution can minimise low-frequency voltage oscillations. Finally, the active region where the voltage oscillations of the DC-link capacitors can be cancelled is identified.*

*For an automotive application the two capacitors of the DC-link can be substituted by two battery packs. In this case the proposed technique makes possible a flexible regulation of the power-sharing among the voltage sources, while guaranteeing the proper voltages at the inverter output. This makes it possible to use two different battery packs to obtain the DC-link of the inverter without any effect on the converter output because the proposed solution can guarantee the correct operation of the inverter even when the sources have different voltage levels.*

## 2.1 Voltage Balance in a Multilevel Multi-Phase Inverter

A three-level T-type multi-phase inverter is shown in Fig. 2.1.

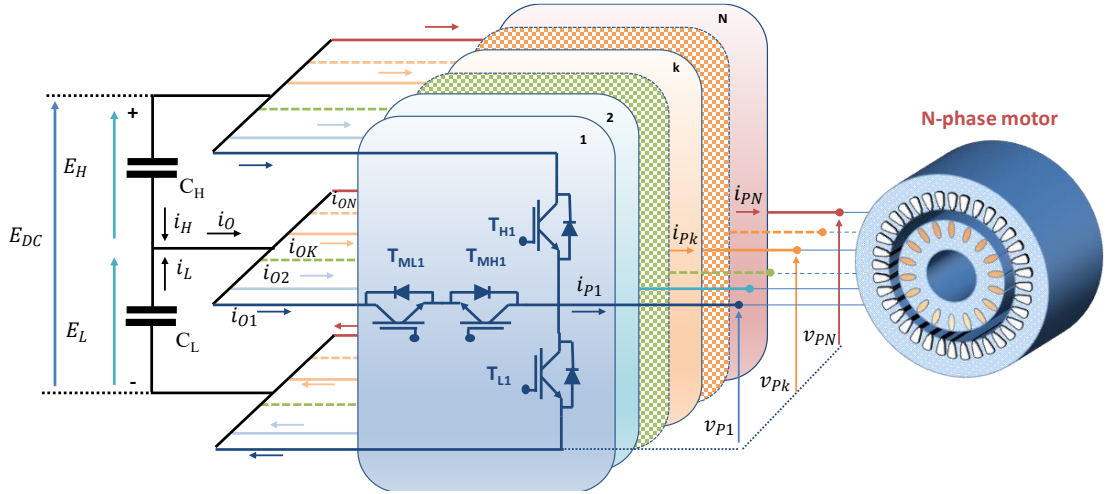


Figure. 2.1 Schematic of a three-level T-type multi-phase inverter.

It is worth noting that, in this chapter, equations concern variable represented in terms of local average values (in a cycle period  $T_c$ ). The ratio of the voltage on the lower capacitor to the total voltage of the DC-link  $\lambda$  can be defined as:

$$\lambda = \frac{E_L}{E_H + E_L} \quad (2.1)$$

According to the fundamental relationship of the capacitors, it is possible to write the following equations concerning the upper (H) and the lower (L) capacitor in the DC-link.

$$i_H = C_H \frac{dE_H}{dt} \quad (2.2)$$

$$i_L = -C_L \frac{dE_L}{dt} \quad (2.3)$$

where the minus sign on the right side of (2.3) is due to the assumed positive direction of the currents, as shown in Fig. 2.1.  $C_H$  and  $C_L$  are the capacitances of the two capacitors.

It is possible to define the current  $i_0$  that flows through the middle point of the converter as the sum of the upper and the lower currents as:

$$i_0 = i_H + i_L \quad (2.4)$$

Considering the common case, when the two the capacitances  $C_H$  and  $C_L$  are equal ( $C_H = C_L = C$ ), and introducing (2.2) and (2.3) in (2.4), leads to:

$$\frac{d(E_H - E_L)}{dt} = \frac{1}{C}(i_H + i_L) = \frac{1}{C}i_0 \quad (2.5)$$

Equation (2.5) shows how the current  $i_0$  represents the unbalancing current, which is proportional to the derivative of the difference between the two capacitor voltages. By this relation, it is possible to show how, in order to keep the voltage difference between the two capacitors constant, it is necessary to keep the current  $i_0$  equal to zero.

As shown in Fig. 2.1, the unbalancing current is the sum of the currents  $i_{0k}$  that pass through the switches  $T_{MHk}$  and  $T_{MLk}$  of the  $k^{th}$  inverter leg. The current  $i_0$  depends not only on the output currents but also on the adopted modulation strategy, which can affect the conduction time of the switches in each leg of the converter [18].

To analyse the modulation strategy, the Vector Space Decomposition, and then the concepts of space vectors and zero-sequence components, will be used. In a multi-phase inverter, the relationship between the modulating signals  $m_k$  and the zero-sequence component  $m_0$  is given by the following equations [19]:

$$m_k = m_0 + n_k \quad \text{for } k = 1, 2, 3, \dots, N \quad (2.6)$$

where:

$$m_0 = \frac{v_0}{E_{DC}} \quad ; \quad n_k = \frac{v_{k,ref}}{E_{DC}} \quad (2.7)$$

$E_{DC}$  is the total DC-link voltage,  $v_0$  is the desired zero-sequence component (1.39) of the inverter pole voltages and  $v_{k,ref}$  is the reference value of the  $k^{th}$  load voltage shown in Fig. 2.1.

In (2.6),  $m_0$  (2.7) is a degree of freedom that can be used to improve the performance of the modulation strategy. In the proposed solution,  $m_0$  will be chosen to minimize the voltage variation of the DC-link.

To control a single leg of a three-level inverter it is necessary to use two separated modulating signals. The modulating signal  $m_{Hk}$  controls the switches  $T_{Hk}$  and  $T_{MHk}$ , the modulating signal  $m_{Lk}$  control the switches  $T_{Lk}$  and  $T_{MLk}$  of the  $k^{th}$  inverter leg. The three admitted states of the leg are obtained by an opportune choice of the signals  $m_{Hk}$  and  $m_{Lk}$  in compliance with the constraints. The control of the inverter is an easy extension of the control of the single inverter leg.

The output pole voltage  $v_{pk}$ , defined as the voltage between the  $k^{th}$  inverter pole and the negative terminal of the DC link, shown in Fig. 2.1, can be expressed as follows:

$$v_{pk} = m_{Hk}E_H + m_{Lk}E_L \quad (2.8)$$

Equation (2.8) can be rewritten by introducing the parameter  $\lambda$  defined in (2.1):

$$v_{pk} = E_{DC}[m_{Hk}(1 - \lambda) + m_{Lk} \lambda] \quad (2.9)$$

The two modulating signals,  $m_{Hk}$  and  $m_{Lk}$ , are related to the modulating signal  $m_k$ , defined by (2.6), by the following relationships:

$$m_{Hk} = \begin{cases} \frac{m_k - \lambda}{1 - \lambda} & \text{if } m_k \geq \lambda \\ 0 & \text{Otherwise} \end{cases} \quad k = 1, 2, 3, \dots, N \quad (2.10)$$

$$m_{Lk} = \begin{cases} 1 & \text{if } m_k \geq \lambda \\ \frac{m_k}{\lambda} & \text{Otherwise} \end{cases} \quad k = 1, 2, 3, \dots, N \quad (2.11)$$

The meaning of the modulating signals  $m_{Hk}$  and  $m_{Lk}$  is shown in Fig. 2.2. The two modulating signals, high (H) and low (L), are obtained by the modulating signal  $m_k$  by considering two carrier waveforms. The low carrier wave is a triangle wave in the range  $[0-\lambda]$  and the higher carrier wave is a triangle wave in the range  $[\lambda-1]$ .

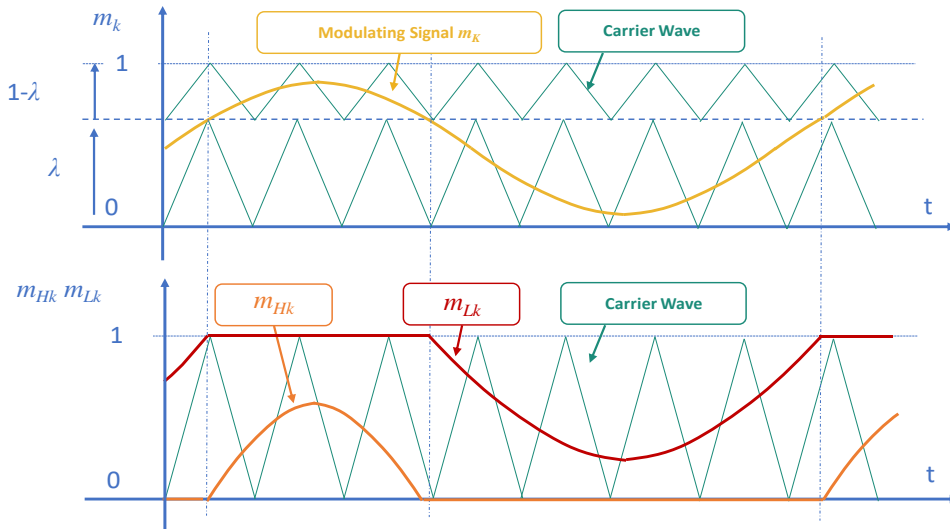


Fig. 2.2 Graphic representation of the meaning of the modulating signals  $m_k$ ,  $m_{Hk}$ ,  $m_{Lk}$ .

By observing the scheme of a single leg of the T-type inverter shown in Fig. 2.1, it is possible to find the relationships between the current in the leg and the duty cycles of the switches as a function of the modulating signals as follows:

$$i_{Hk} = \begin{cases} m_{Hk} i_{pk} & \text{if } m_k \geq \lambda \\ m_{Hk} i_{pk} & \text{Otherwise} \end{cases} \quad (2.12)$$

$$i_{0k} = \begin{cases} (1 - m_{Hk}) i_{pk} & \text{if } m_k \geq \lambda \\ m_{Lk} i_{pk} & \text{Otherwise} \end{cases}$$

$$i_{Lk} = \begin{cases} (1 - m_{Lk})i_{pk} & \text{if } m_k \geq \lambda \\ (1 - m_{Lk})i_{pk} & \text{Otherwise} \end{cases}$$

where  $i_{Hk}$  and  $i_{Lk}$  are the currents which pass respectively through the switches  $T_{MHk}$  and  $T_{MLk}$  of the  $k$ th leg.

Equation (2.13) shows how the value of the current  $i_{0k}$  depends on the duty-cycles of the upper and lower switches ( $m_{Hk}$ ,  $m_{Lk}$ ), as well as from the output phase currents  $i_{pk}$ .

Introducing (2.10) and (2.11) in (2.12), it is possible to obtain the expression of the currents as a function of the modulating signals  $m_k$  and the ratio of the voltage capacitors as:

$$\begin{aligned} i_{Hk} &= \begin{cases} \left(\frac{m_k - \lambda}{1 - \lambda}\right) i_{pk} & \text{if } m_k \geq \lambda \\ 0 & \text{Otherwise} \end{cases} \\ i_{0k} &= \begin{cases} \left(\frac{1 - m_k}{1 - \lambda}\right) i_{pk} & \text{if } m_k \geq \lambda \\ \frac{m_k}{\lambda} i_{pk} & \text{Otherwise} \end{cases} \\ i_{Lk} &= \begin{cases} 0 & \text{if } m_k \geq \lambda \\ \left(1 - \frac{m_k}{\lambda}\right) i_{pk} & \text{Otherwise} \end{cases} \end{aligned} \quad (2.13)$$

For a compact formulation of the unbalancing current expression, is needful to introduce the following variables:

$$S_k = \begin{cases} +1 & \text{if } m_k \geq \lambda \\ -1 & \text{Otherwise} \end{cases} \quad (2.14)$$

By replacing (2.14) in (2.13), and according to (2.6), it is possible to obtain the following compact expression of  $i_{0k}$ :

$$i_{0k} = \frac{1 + S_k[1 - 2(m_0 + n_k)]}{1 + S_k(1 - 2\lambda)} i_{pk} \quad (2.15)$$

The current  $i_0$  can be evaluated as:

$$i_0 = \sum_{k=1}^N \frac{1 + S_k[1 - 2(m_0 + n_k)]}{1 + S_k(1 - 2\lambda)} i_{pk} \quad (2.16)$$

As (2.5) states that the voltage imbalance of the input capacitors depends on  $i_0$ , (2.16) shows that it can be indirectly controlled through  $m_0$ , which is the degree of freedom used by the proposed strategy to control the voltage balancing.

It is possible to rewrite (2.16) as:

$$i_0 = \sum_{k=1}^N \frac{1 + S_k(1 - 2n_k)}{1 + S_k(1 - 2\lambda)} i_{pk} - \sum_{k=1}^N \frac{S_k 2m_0}{1 + S_k(1 - 2\lambda)} i_{pk} \quad (2.17)$$

Solving (2.17) for  $m_0$ , considering the fundamental relation  $\sum_{k=1}^N i_{pk} = 0$ , leads to the following explicit expression of  $m_0$ :

$$m_0 = \frac{\sum_{k=1}^N \frac{i_{pk}}{1 + S_k(1 - 2\lambda)} - \frac{2S_k n_k}{1 + S_k(1 - 2\lambda)} i_{pk} + \frac{S_k}{1 + S_k(1 - 2\lambda)} i_{pk} - i_0}{2 \sum_{k=1}^N \frac{S_k}{1 + S_k(1 - 2\lambda)} i_{pk}} \quad (2.18)$$

After some steps it is possible to obtain the following compact form of (2.18):

$$m_0 = \lambda - \frac{\sum_{k=1}^N \frac{(2S_k n_k)}{1 + S_k(1 - 2\lambda)} i_{pk} + i_0}{2 \sum_{k=1}^N \frac{S_k}{1 + S_k(1 - 2\lambda)} i_{pk}} \quad (2.19)$$

In the most common conditions, the two capacitor voltages are constant and equal to each other. In this case, the value of  $\lambda$  assumes a constant value of 0.5, and the current  $i_0$  must be equal to zero. It is important to underline that the value of  $\lambda$  does not affect the maximum output voltage of the converter.

Introducing the previous considerations, (2.19) can be rewritten in the following simplified version:

$$m_0 = \frac{1}{2} - \frac{\sum_{k=1}^N S_k n_k i_{pk}}{\sum_{k=1}^N S_k i_{pk}} \quad (2.20)$$

Equation (2.20) asserts that  $m_0$  is the sum of the constant  $\frac{1}{2}$  and a fluctuating term that depends on the coefficients  $S_k$  and the power exchanged by the phases, when the voltages across the two capacitors are equal. Solving (2.20) is not straightforward because the parameters  $S_k$  introduce an interaction. In fact, the values of  $S_k$  depend on  $m_k$  that rely, for (2.6), on  $m_0$ . Consequently, to solve this problem it is necessary to introduce other constraints.

As long as  $m_0$  varies within the range presented in (2.21) it is possible to write the following inequality [38]:

$$\begin{aligned}
 m_{0\ DPWM-MIN} &= - \min_{k=1, \dots, N} \left\{ \sum_{\rho(\text{odd})=1}^{N-2} \frac{\bar{v}_\rho}{E_{DC}} \cdot \bar{\alpha}_k^\rho \right\} \leq m_0 \\
 &\leq 1 - \max_{k=1, \dots, N} \left\{ \sum_{\rho(\text{odd})=1}^{N-2} \frac{\bar{v}_\rho}{E_{DC}} \cdot \bar{\alpha}_k^\rho \right\} = m_{0\ DPW-MAX}
 \end{aligned} \tag{2.21}$$

The *DPWM* (Discontinuous Pulse-Width Modulation) in (2.21) are two of the modulation strategies that will be compared in this thesis with the proposed solution.

In the case that all  $s_k$  are equal, the current  $i_0$  does not depend on  $m_0$ , but only on the phase currents and voltages because, when all  $s_k$  are equal to 1 or -1,  $m_0$  is respectively equal to 1 or 0. According to (2.16), substituting the respective value of  $m_0$ , it is possible to provide the expression of  $i_0$  when all  $s_k$  is equal to 1 ( $i_{0+}$ ) and when all  $s_k$  is equal to -1 ( $i_{0-}$ ).

$$i_{0+} = -\frac{1}{1-\lambda} \sum_{k=1}^N i_{Pk} n_k \tag{2.22}$$

$$i_{0-} = \frac{1}{\lambda} \sum_{k=1}^N i_{Pk} n_k \tag{2.23}$$

When the voltages of the two capacitors are equal ( $\lambda = \frac{1}{2}$ ) the two currents,  $i_{0+}$  and  $i_{0-}$ , are opposite to each other. Also, the absolute value of  $i_0$  is proportional to the power delivered to the load. On the other hand, if the values of the functions  $s_k$  are not equal, (2.16) shows that current  $i_0$  depends on  $m_0$ , the phase currents  $i_{Pk}$  and  $n_k$ .

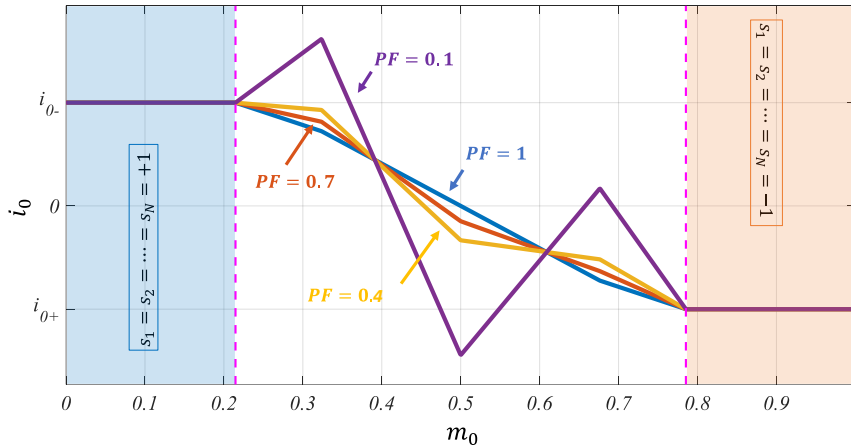


Figure 2.3 Example of trends of  $i_0$  as a function of the zero-sequence  $m_0$  for a five-phase inverter.

Fig. 2.3 shows the trend of  $i_0$  as a function of  $m_0$  with different value of the load Power Factor (PF) for a five-phase inverter. This function is a piecewise line whose slope changes abruptly as soon as the configuration of the variables  $s_1, \dots, s_N$  changes.

As shown in (2.5), in order to keep the capacitor voltages constant,  $i_0$  must be zero. Fig. 2.3 shows that a value of  $m_0$  that makes  $i_0$  equal to zero always exists. As can be seen, the solution may not be unique, or it may not satisfy the modulation constraints depending on the working conditions.

To find the solution of (2.20) it is necessary to find the admissible combinations of values  $s_1, \dots, s_N$ . To solve this problem, let us suppose that the signals  $n_k$  are ordered in descending order so that

$$n_1 > n_2 > \dots > n_F > \dots > n_N \quad (2.24)$$

and  $F$  is the index of the lowest modulating signal that is greater than or equal to  $\lambda$ :

$$m_F > \lambda \quad (2.25)$$

$$m_{F+1} < \lambda \quad (2.26)$$

where  $F$  must be an integer number in the range  $[1, N - 1]$ .

Under this assumption the coefficients  $s_k$  are not all equal. It results that  $s_k$  is equal to 1 for  $k \leq F$  and equal to  $-1$  for  $k > F$ . Consequently, if the sum of the load currents is zero, it is possible to write the following relationship:

$$\sum_{k=1}^N i_{pk} = \sum_{k=1}^F i_{pk} + \sum_{k=F+1}^N i_{pk} = 0 \quad (2.27)$$

Eq. (2.19) can be rewritten as:

$$m_0 = \lambda - \frac{\sum_{k=1}^F \frac{n_k}{(1-\lambda)} i_{pk} - \sum_{k=F+1}^N \frac{n_k}{\lambda} i_{pk} + i_0}{\sum_{k=1}^F \frac{i_{pk}}{(1-\lambda)} - \sum_{k=F+1}^N \frac{i_{pk}}{\lambda}} \quad (2.28)$$

After some steps, is possible to simplify (2.28) as:

$$m_0 = \lambda - \frac{(\lambda - 1) \sum_{k=1}^N n_k i_{pk} + \sum_{k=1}^F n_k i_{pk} + i_0 (1 - \lambda) \lambda}{\sum_{k=1}^F i_{pk}} \quad (2.29)$$

Equation (2.29) shows that, for each value of  $F$  in the range  $[1, N - 1]$ , it is possible to find a value for  $m_0$ .

A flow chart of the algorithm is shown in Fig. 2.4.

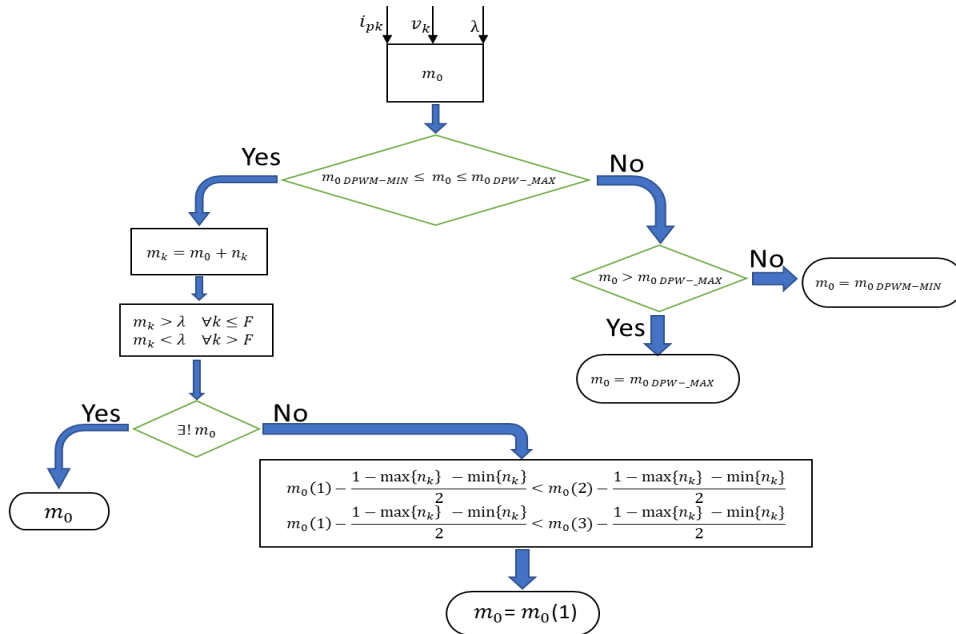


Figure 2.4 Simple representation of the proposed algorithm for  $m_0$  calculation.

As inputs, it takes  $i_{pk}$ ,  $v_k$ ,  $\lambda$  and with (2.29) calculates the value of  $m_0$  after calculating the values of  $S_k$ . The result of (2.29) can be multiple; all the solutions must satisfy the constraint of modulation (2.21), and if one or more solutions do not verify it, they will be deleted. If all solutions do not confirm the constraint,  $m_0$  will be taken equal to the nearest limit in the modulation range. Among all the solutions that confirm the constraint is necessary to verify that the modulating signals obtained by the value of  $m_0$  taken as output of the algorithm, refer to the same start conditions identified by (2.25) and (2.26). If, at this point, more than one solution is available, the answer taken is the one that has the less distance to the space vector pulse width modulation (SVPWM) [39] algorithm which is commonly recognised as a modulation strategy with good performance, and it is taken as a reference for a comparison.

## 2.2 Control Scheme for Voltage Balance

The control scheme that allows controlling the voltage of the input capacitors, through the measurements of the voltages of the lower and upper capacitors, that are already available for correct modulation, is shown in Fig. 2.5.

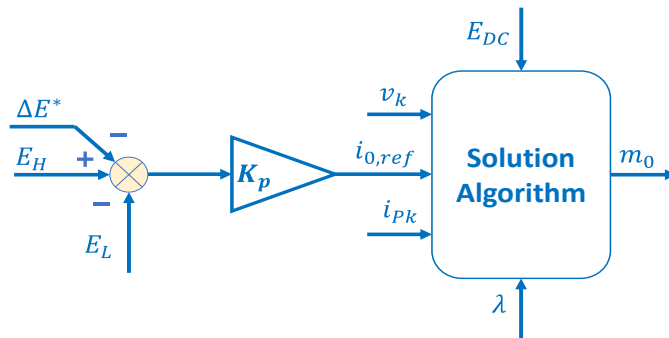


Figure 2.5 Control scheme for the voltages of the DC capacitors.

The reference value,  $\Delta E^*$  is equal to  $E_H - E_L$  and acts as the desired voltage imbalance value. To increase the value of  $E_H$  compared to  $E_L$ , the current  $i_0$  must be positive and, vice versa, to increase the value of  $E_L$  compared to  $E_H$ , the current  $i_0$  must be negative, according to the convention adopted in Fig. 2.1. Finally, to maintain  $E_H - E_L$  constant, the current  $i_0$  must be zero. Therefore, the reference value for the current  $i_{0,ref}$  is calculated as follows:

$$i_{0,ref} = -K_p[\Delta E^* - (E_H - E_L)] \quad (2.30)$$

The proportional gain  $K_p$  affects the transient response of the system. Replacing (2.30) in (2.5), one finds the first order differential equation (2.31), whose time constant is  $C/K_p$ , which ensures the convergence of  $E_H - E_L$  to  $\Delta E^*$  with an exponential transient.

$$(E_H - E_L) - \frac{C}{K_p} \frac{d}{dt}(E_H - E_L) = \Delta E^* \quad (2.31)$$

The requested current  $i_{0,ref}$ , generated by (2.30), is the input of the algorithm represented in Fig. 2.5, that allows to obtain the value of  $m_0$  that guarantees the request voltage reference  $\Delta E^*$ .

### 2.3 Domain Without Low-Frequency Voltage Oscillations

The input capacitors are subjected to different stress which can reduce their operational life. During the converter operations, high-frequency voltage harmonics arise due to the switch commutations and low-frequency voltage oscillations can take place owing to imbalance problems. The high-frequency harmonics are unavoidable, but a suitable choice of  $m_0$  can eliminate the low frequency harmonics. If the modulation index is lower than a threshold value that depends on the number of phases, the reference voltage vectors, the output phase currents, and the load power factor in each subspace, a proper value of  $m_0$ , selected according with (2.19), allows to eliminate the low-frequency harmonics and thus reduce the voltage stress on the input capacitors.

Due to the large number of variables, it is not possible to find a simple description of this domain, but it can be plotted under the assumptions that only the voltage vector space one  $\bar{v}_1$  and the current vector space one  $\bar{i}_1$  are different from zero, and the input DC capacitors are balanced ( $\lambda = 0.5$ ). The resulting boundaries of the modulation index  $MI$  have been numerically calculated and illustrated in Fig. 2.6 as a function of the number of phases  $N$ , and the displacement angle between  $\bar{v}_1$  and  $\bar{i}_1$ .

The modulation index  $MI$  shown in Fig. 2.6 is defined as the ratio between the magnitude of the required voltage vector  $\bar{v}_1$  and the maximum voltage available in a three-phase inverter.

$$MI = \frac{|\bar{v}_1|}{E_{DC}/\sqrt{3}} \quad (2.32)$$

The higher the fundamental power factor, the higher the modulation index  $MI$  that can be reached while keeping the input capacitor voltages balanced.

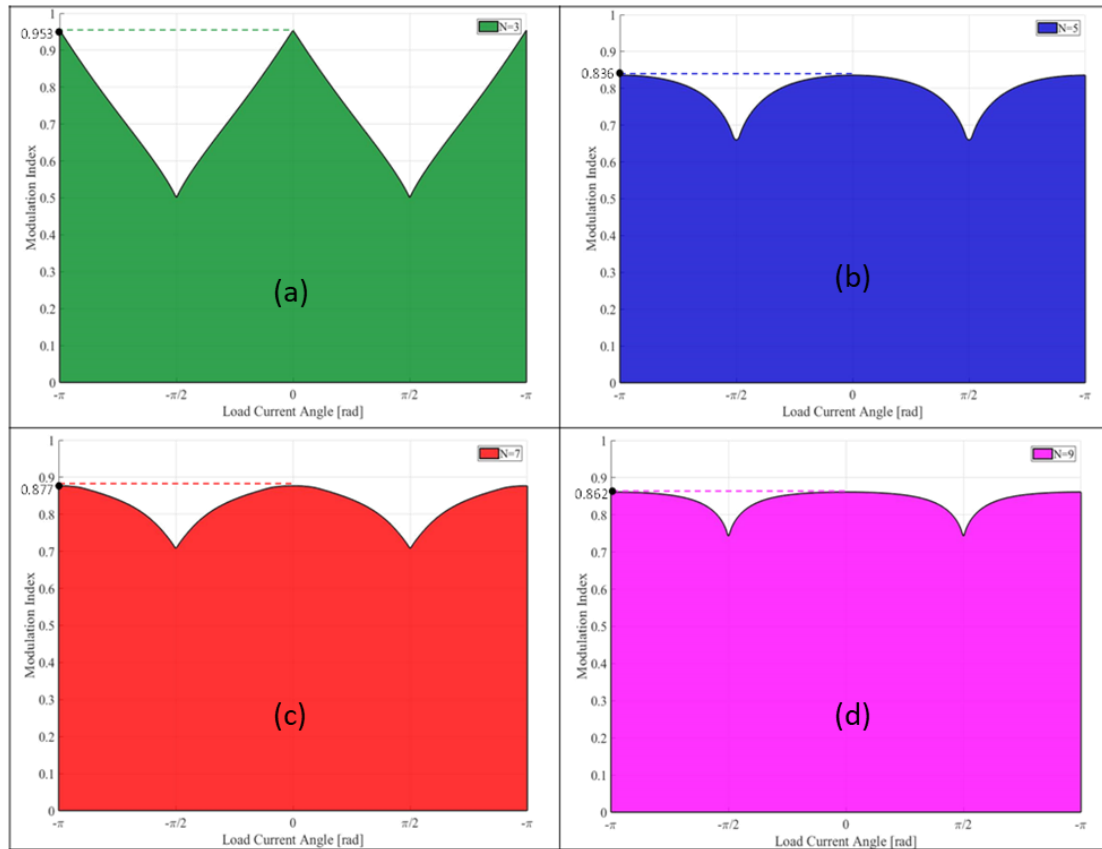


Figure 2.6 Boundaries of the operating zone where the voltages of the input capacitors can be balanced without significant voltage ripple for three-phase (a), five-phase (b), seven-phase (c) and nine-phase (d) inverters.

As the number of phases increases, in sinusoidal steady-state operating conditions, the highest modulation index ensuring the voltage balance becomes less dependent on the fundamental power factor, but the maximum modulation index  $MI$  that guarantees the linear modulation range decreases. If the modulation index exceeds the value given by the curve of Fig. 2.6, for a given number of phases and a given displacement angle of the current, the developed algorithm keeps the input capacitors balanced on average, although a low-frequency voltage oscillation appears, which is the smallest possible in compliance with the voltage limits.

In order to investigate the amplitude of this low-frequency oscillations on the input capacitor voltages, it is necessary to introduce a new index,  $Q_0$ , which represents the imbalance charge of the capacitors in a fundamental period  $T$ , normalized by  $T |\bar{i}_1|$ :

$$Q_0 = \frac{\int_0^T |i_0| dt}{T |\bar{i}_1|}. \quad (2.33)$$

It is straightforward to verify that  $Q_0$  is related to the variation of the quantity  $C (E_H - E_L)$ , as given in (2.5), over the time interval  $[0, T]$ .

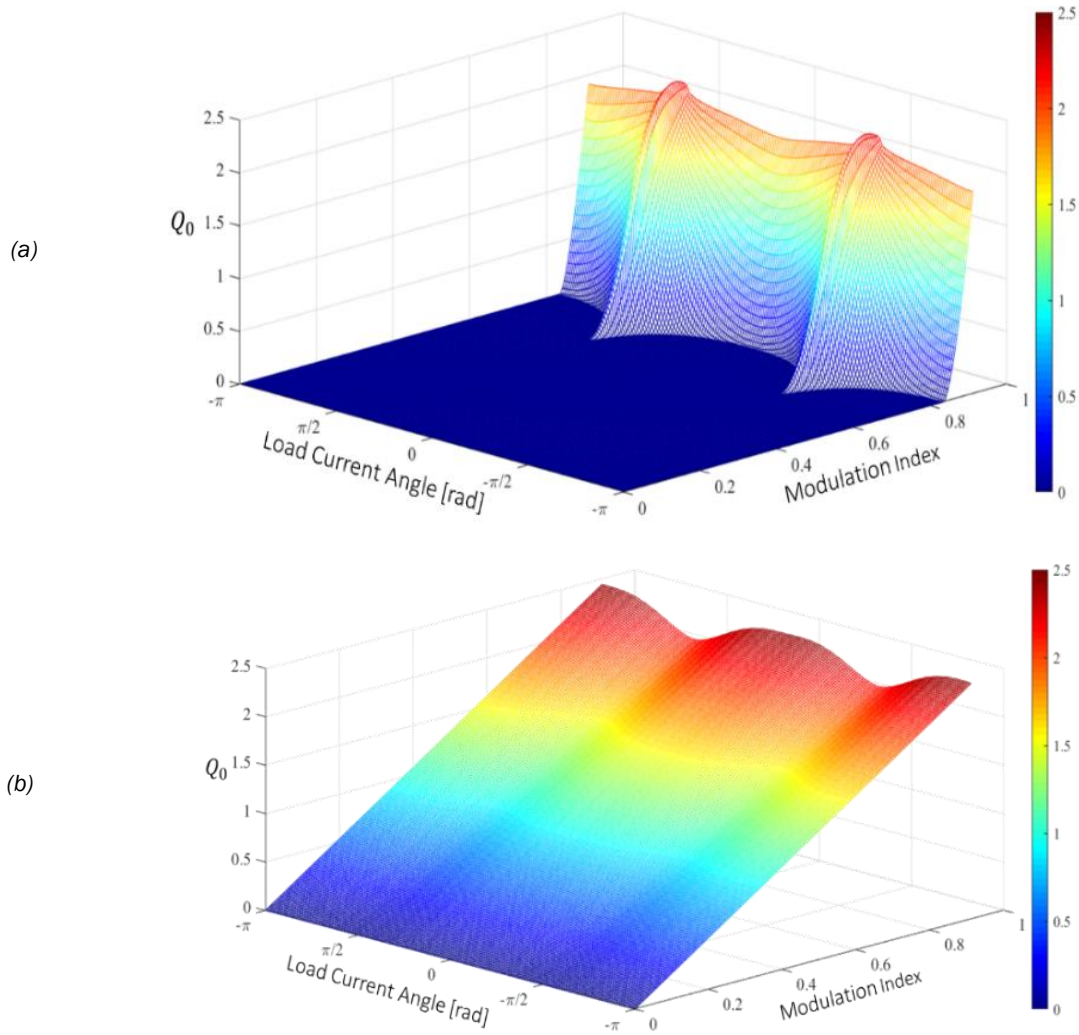


Figure 2.7 Equivalent electric charge exchanged by the DC capacitors over a period of the output voltage in a five-phase inverter with the proposed optimized modulation (a) and with SVPWM (b).

Fig. 2.7 shows the amplitude of  $Q_0$  as a function of the modulation index and load power factor for a five-phase inverter, under the assumption that the load currents and voltages are sinusoidal (only  $\bar{v}_1$  and  $\bar{i}_1$  are assumed to be different from zero). As can be seen, in Fig. 2.7(a),  $Q_0$  achieved by the proposed solutions is zero for low values of the modulation index and increases for the higher values of the modulation index. The oscillations that are generated in case of higher modulation index, also compared with the SVPWM modulation (b), is the smallest as possible because in these conditions, the value of  $m_0$  that is calculated by (2.19) is out of the range imposed by (2.21) and the nearest value is the boundary of the range. Fig. 2.7(b) shows the results obtained in the same operating conditions with SVPWM modulation. In this case, a voltage oscillation is present for any modulation index other than zero, and the amplitude of the oscillations is always greater than the voltage oscillations introduced by the proposed solution under the same operating conditions.

## 2.4 Experimental Results

In order to validate the developed solution, several tests have been carried out with a three-level five-phase T-type inverter. To test the behavior of the control scheme in a practical application a test bench was set up in the LEMAD laboratory of Bologna, as shown in Fig. 2.8.

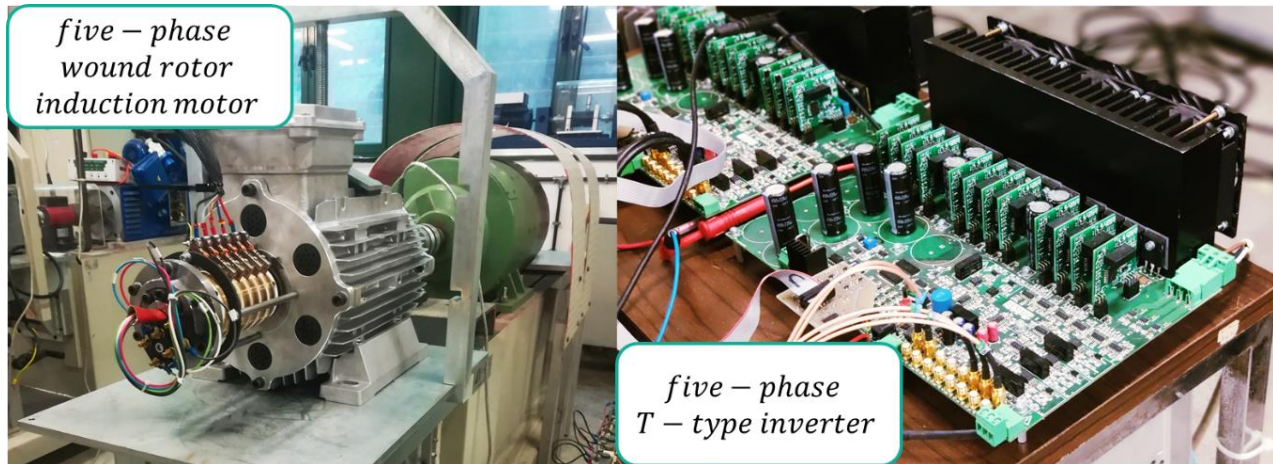


Figure 2.8 Experimental setup.

The three-level NPC T-type inverter was connected to a five-phase induction motor and a rotor field-oriented control scheme was used, with a closed-control loop for adjusting the motor speed, measured by an incremental encoder. A block diagram of the control scheme, that was implemented on a TMS320F28335 development board, produced by Texas Instruments, is shown in Fig. 2.9. Different kinds of modulation techniques were tested to confirm the efficiency of the proposed solution.

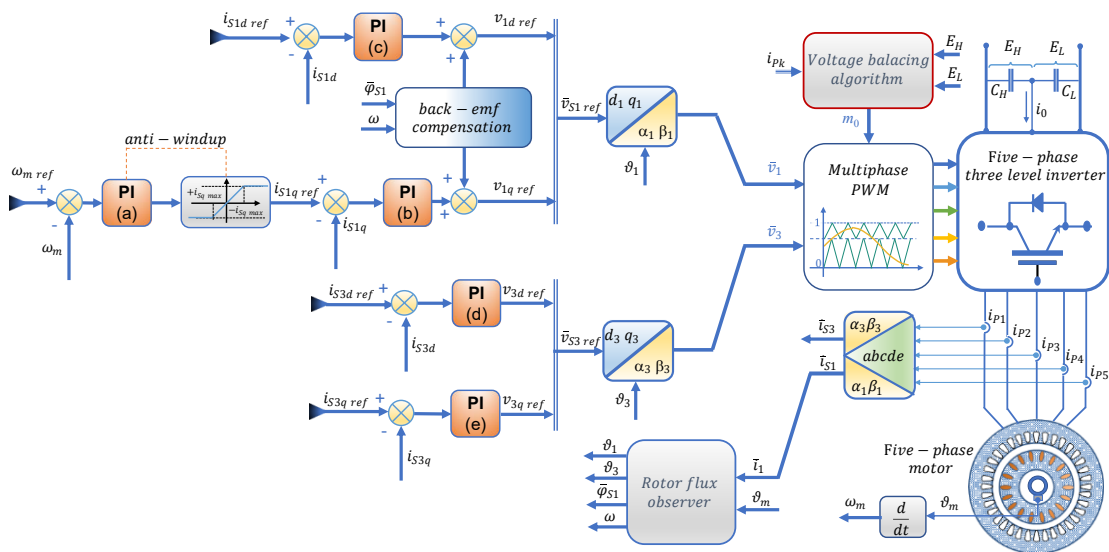


Figure 2.9 Control scheme of the five-phase induction motor drive with voltage balancing algorithm.

The motor parameters are shown in Table 2.1 while the inverter parameters are in Table 2.2.

| Parameters of the Five-Phase Induction Machine     |                            |
|--|----------------------------|
| $\omega_{m, rated} = 15.7 \text{ rad/s (150 rpm)}$ | $p = 3$                    |
| $R_S = 1.7 \ \Omega$                               | $R_R = 2.03 \ \Omega$      |
| $L_{S1} = 410 \text{ mH}$                          | $L_{S3} = 68 \text{ mH}$   |
| $L_{R1} = 399 \text{ mH}$                          | $L_{R3} = 65.8 \text{ mH}$ |
| $M_1 = 362 \text{ mH}$                             | $M_3 = 35 \text{ mH}$      |

Table 2.1 Parameters of the Five-Phase Induction Machine.

| Parameters of the Five-Phase three-level T-type inverter |                               |
|--|-------------------------------|
| MOSFET $I_{max} = 36 \text{ A}$                          | $E_{DC} = 120 \text{ V}$      |
| Switching frequency = 5 kHz                              | dead time = 2.6 $\mu\text{s}$ |
| $C_H = C_L = 750 \ \mu\text{F}$                          |                               |

Table 2.2 Parameters of the Five-Phase three-level T-type inverter.

To validate the proposed solution some experimental tests were carried out. The solution has also been compared with the SVPWM technique.

In Fig. 2.10, the results of the compared test in steady-state conditions at low speed (100 rpm) are reported. In the first part of the time interval shown in Fig. 2.10,  $m_0$  is selected according to the SVPWM technique, whereas, in the second part, the proposed balancing control technique is activated. In light blue and red the variation of the DC-link capacitor voltages  $E_H$  and  $E_L$  respect to  $E_{DC}/2$  are shown. When the SVPWM technique is used (left side), the voltages of the input capacitors fluctuate at five times the fundamental frequency, whereas the proposed balancing technique (right side) keeps them almost constant. The remaining small oscillations are due to the inverter dead times and nonlinearities. As can be seen, the waveform of  $m_0$  is significantly different in the two tests, but the output phase current is almost sinusoidal in both cases because, from (2.6), the zero-sequence component  $m_0$  is a degree of freedom.

Note that, low speed operating conditions are more demanding than high speed ones.

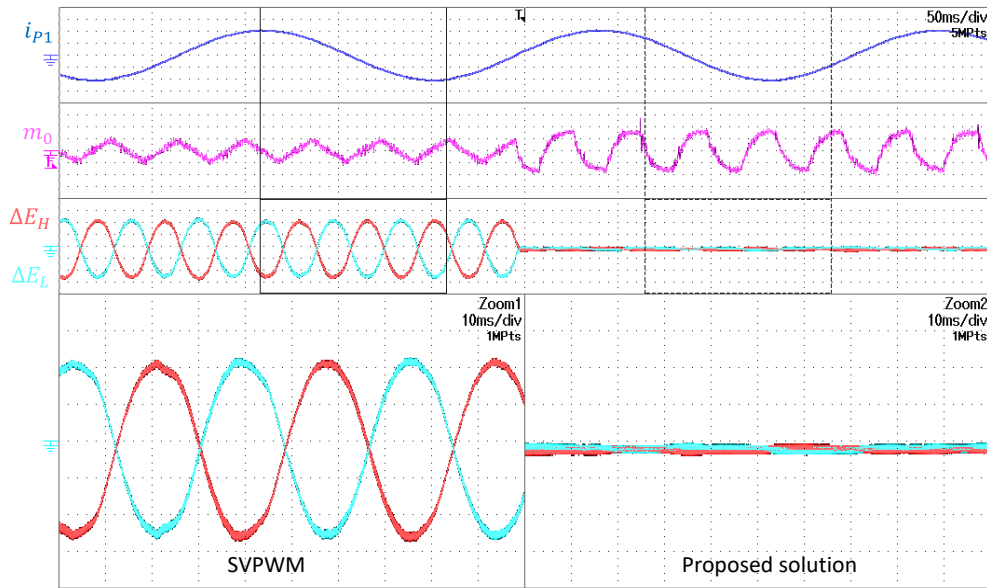


Figure 2.10 Waveforms of the DC-link capacitor voltages and current  $i_{p1}$  of a three-level five-phase electric drive at 100 rpm with SVPWM (left side) and the proposed solution (right side). Phase current  $i_{p1}$  (2 A/div), zero sequence component of modulation signals  $m_0$  (0.1/div), variation of the DC-link capacitor voltages  $E_H$  and  $E_L$  respect to  $E_{DC}/2$  (2 V/div).

Subsequently, the capability of the proposed control algorithm to unbalance the voltage capacitor for a desired value  $\Delta E^*$  has been verified. In Fig. 2.11, an imbalance between the two capacitors of 15V and then 30V is shown.

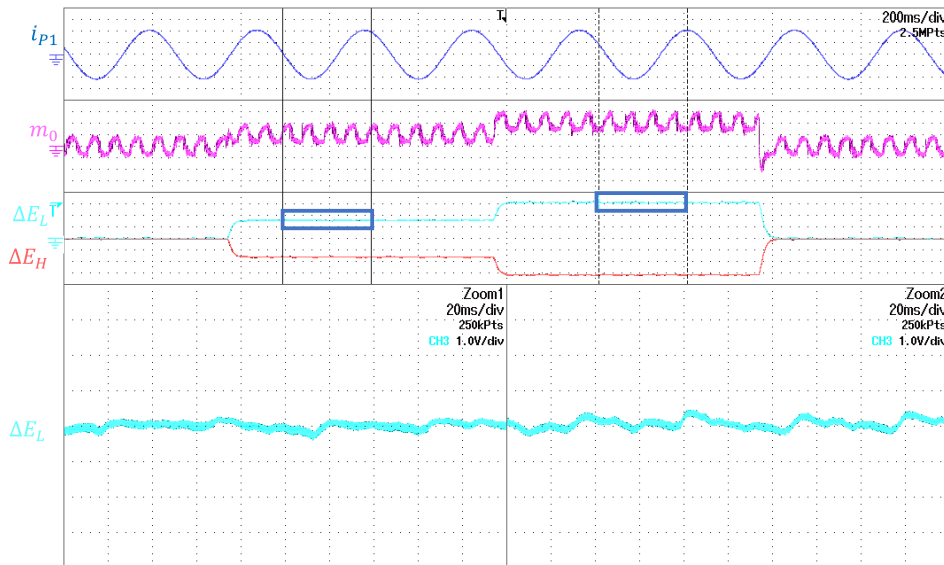


Figure 2.11 Imbalance of the DC-link capacitor voltages. Phase current  $i_{p1}$  (1 A/div), zero-sequence component of the modulating signals  $m_0$  (0.02/div), variation of the DC-link capacitor voltages  $E_H$  and  $E_L$  from  $E_{DC}/2$  (5 V/div).

In response to a request of voltage imbalance of the DC capacitors, obtained through a set point  $\Delta E^*$  different from zero, the waveform of  $m_0$  changes consequently to pursue the reference value. Also in this conditions ( $\lambda \neq 0.5$ ), the output phase current is almost sinusoidal and the voltages of the two capacitors do not show significant oscillations. This feature of the control system can be exploited in some applications where the power sharing of the sources is needed, in reason of their characteristics, without affecting the output of the system.

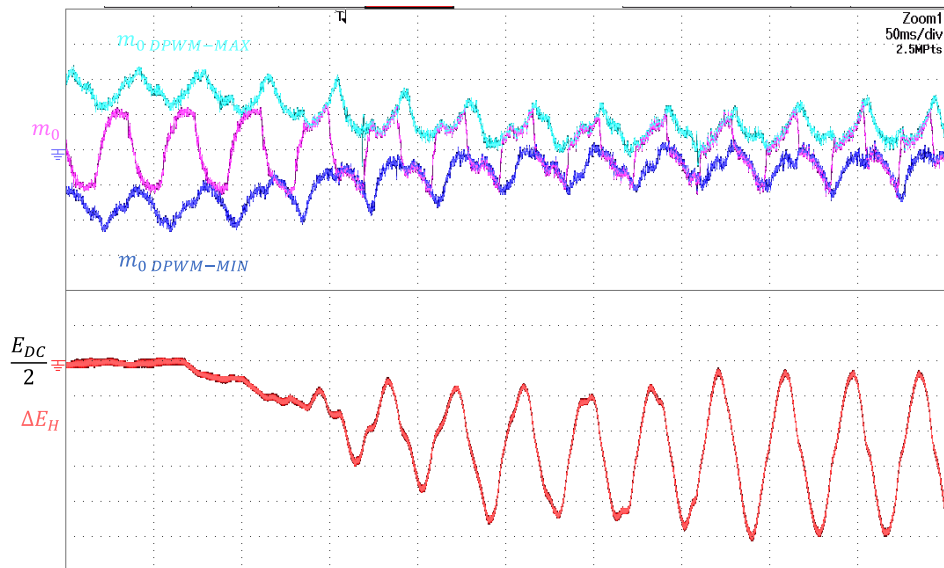


Figure 2.12 Waveform of  $m_0$  when the DC-link voltage of a three-level five-phase electric drive rotating at 100 rpm decreases from 120 V to 80 V. Zero sequence component of modulation signals  $m_0$  (0.2/div). Variation of the DC-link capacitor voltage  $E_L$  respect to  $E_{DC}/2$  (4 V/div).

As described in the previous sections, the balancing of the voltages is guaranteed by choosing a proper value of  $m_0$  in the specific work conditions. When the exact solution of  $m_0$  that annuls the oscillations is not available, the voltages present some oscillations. This situation is represented in Fig. 2.12 where the internal control variable  $m_{0 DPWM-MAX}$ ,  $m_{0 DPWM-MIN}$  and  $m_0$  are shown.

In particular, Fig. 2.12 shows the behaviour of the inverter when the modulating index exceeds the threshold value that allows balancing the input capacitors. The DC-link voltage is lowered from 120V to 80V. If the modulation index is sufficiently low, the voltages of the capacitors remain constant. Conversely, if  $m_0$  reaches the boundaries of the linear modulation (2.21), a voltage oscillation arises. As specified by the theory, in this case, the fluctuation of the voltages is as low as possible.

To verify this statement, other experimental tests were carried out. A comparison was made between the proposed solution and the SVPWM modulations that is taken as reference. The tests are made with the same DC-link voltage and, to reach the limit in the proposed modulation, a speed transient was performed. In these operation conditions, the modulation index was high, and the correct value of  $m_0$  was not applicable.

In Fig. 2.13, a comparison between the SVPWM (a) and the proposed solution (b) at two different speeds are shown. When the speed is low, the proposed solution is more efficient than the SVPWM modulation. In these conditions, as also shown in Fig. 2.10, the proposed solution annuls the voltage oscillation without affecting the system's output. The interesting case is when the speed increase, and consequently the modulation index becomes greater. In these conditions, the correct value of  $m_0$ , which is the proposed algorithm's output, is not applicable. Some voltage oscillations arise, but those voltage oscillations are lower than those generated by the standard technique.

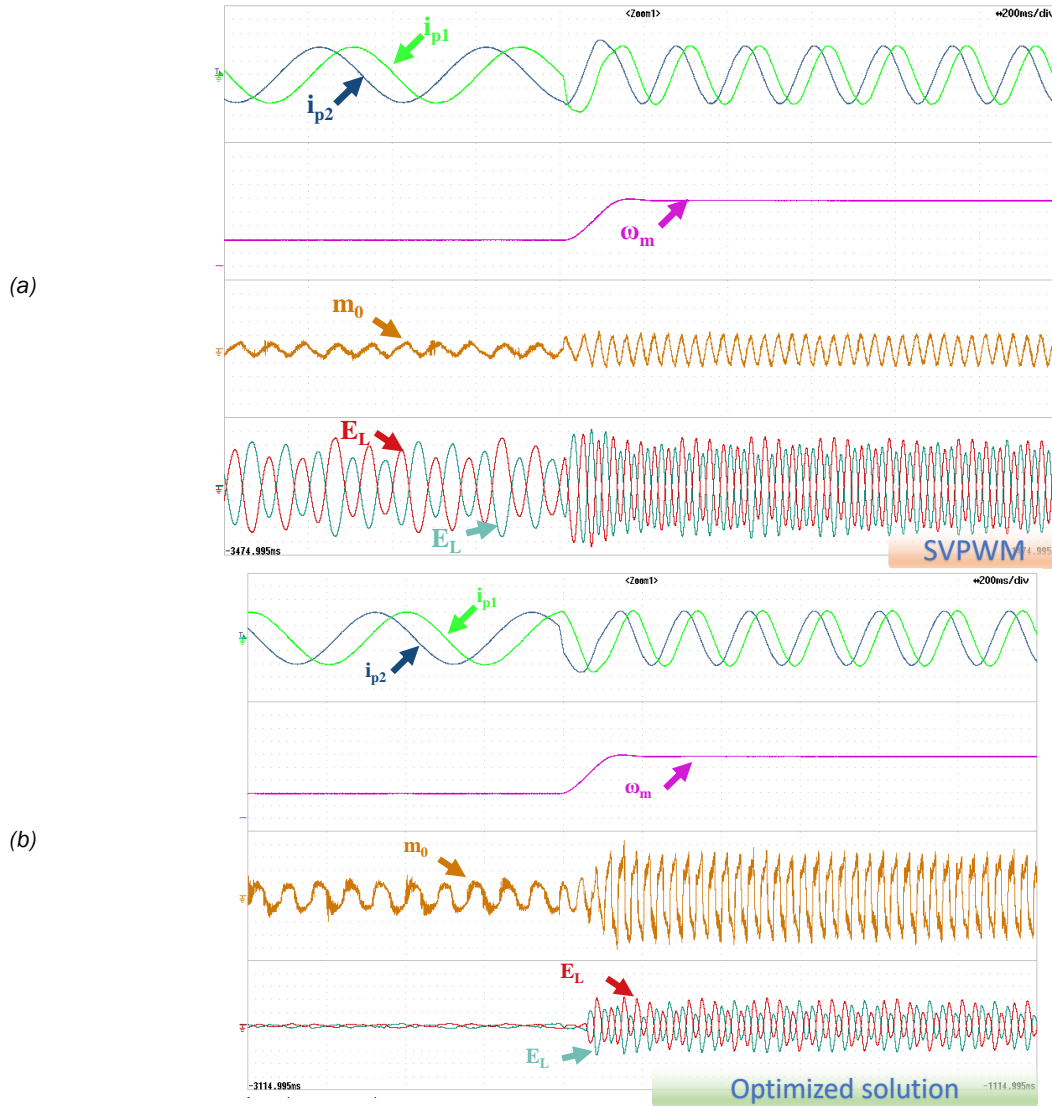


Figure 2.13. Speed transient of the three-level five-phase induction motor drive from 50 rpm to 120 rpm with SVPWM (a) and with the proposed modulation strategy (b). Phase currents  $i_{p1}$  and  $i_{p2}$  (2 A/div), rotor speed (25 rpm/div), zero-sequence component of modulating signals  $m_0$  (0.2/div), variation of the DC-link capacitor voltages  $E_H$  and  $E_L$  with respect to  $E_{DC}/2$  (2 V/div).

Finally, some tests were carried out in different stress conditions, obtained with the degrees of freedom provided by the multi-phase technology, to confirm the proposed solution general validity.

The capability of the algorithm to keep the capacitor voltages constant even if the control system involves subspaces other than the fundamental one has been subsequently verified. In Fig. 2.14, it is possible to observe the waveform of the inverter currents when a third-order harmonic current circulates by applying the voltage vector  $\bar{v}_3$  to the load. The injection of a third-order harmonic current can be used to increase the torque density both in multi-phase induction machines [40], [41] and surface mounted permanent magnet machines [42], [43]. As can be seen, the capacitor voltage balancing is ensured also in this operating condition.

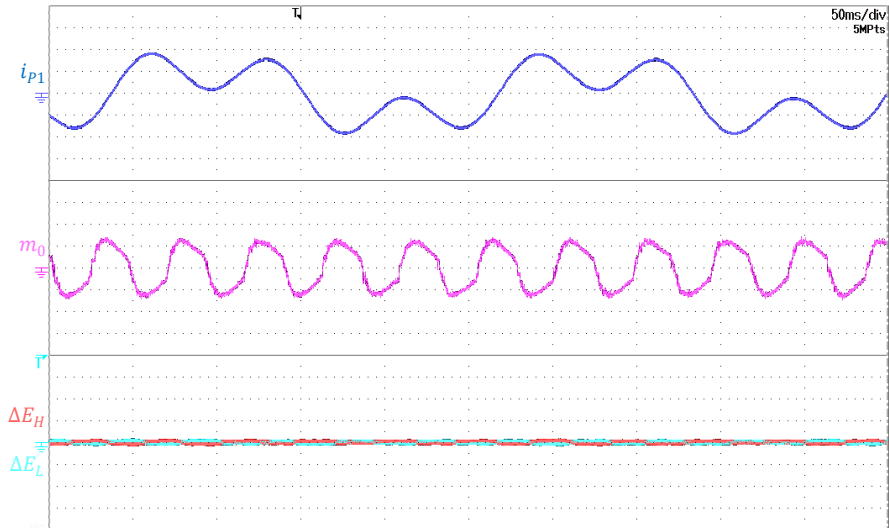


Figure 2.14 Third harmonic injection. Phase current  $i_{p1}$  (2 A/div), zero-sequence component of modulating signals  $m_0$  (0.1/div), variation of the DC-link capacitor voltages  $E_H$  and  $E_L$  from  $E_{DC}/2$  (4 V/div).

In order to verify the behaviour of the control algorithm in case of a phase fault, a further test has been carried out. Multi-phase machines are well-known for their fault tolerance capabilities. Therefore, the electric drive has been tested while the control system is forced to keep the current  $i_{p1}$  equal to zero to simulate an open phase fault. For this task, the control system must control the current vectors in all subspaces. Among the different fault-tolerant techniques, the control strategy that minimizes the stator Joule losses has been used, which has been thoroughly investigated in literature [44].

Fig. 2.15 shows that the voltages of the input capacitors are equal to one another, and their voltage ripple is negligible although the current of phase 1 is zero.

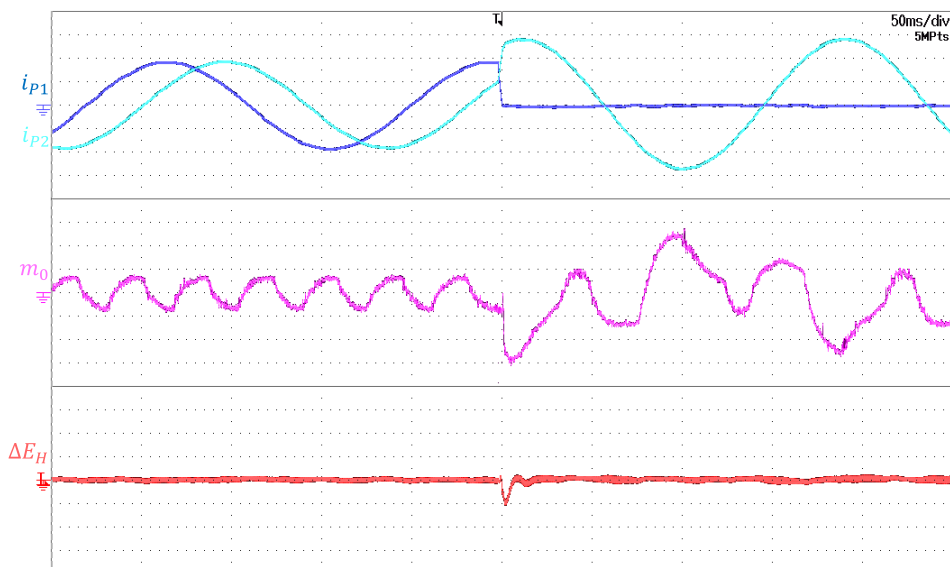


Figure 2.15 Behaviour of the multilevel inverter when the current of phase 1 is kept equal to zero to simulate an open-phase fault. Phase currents (2 A/div), zero-sequence component of the modulating signals  $m_0$  (0.2/div), variation of the DC-link capacitor voltages  $E_H$  from  $E_{DC}/2$  (4 V/div).

## 2.5 Conclusions

In this chapter a modulation technique that allows avoiding low-frequency voltage oscillations of the DC-link capacitors in multi-phase multilevel NPC T-type inverters has been presented.

The solution has a general validity and can be applied to a multi-phase inverter with an odd generic number of phases, under the assumption that the load is star-connected with a single isolated neutral point. The algorithm can also be used for a control system that involves subspaces different from the fundamental one.

For an automotive application, the two DC-bus capacitors can be replaced by two batteries. Due to the ability of the proposed solution to guarantee the correct operation of the inverter even when the voltage levels of the two sources are different, the proposed solution can be used to implement the power-sharing of the sources.

The multilevel converter can be used in automotive application in order to increase the number of levels of the traction motor voltage, and reduce the voltage of the single battery pack [45].

The algorithm operates on a degree of freedom that is available in all system, three-phase or multi-phase, and provides the proper value of  $m_0$  for balancing the voltages. The admissible range of  $m_0$  has been analysed.

The algorithm's limits, which have been obtained by numeric simulations for a different number of phases, have been emphasized. The limits are functions of the modulation index and the load power factor.

Finally, the results of some experimental tests carried out on a five-phase induction motor drive have been presented to demonstrate the effectiveness of the developed algorithm in transient and steady-state operating conditions, in the case of an open-phase fault, and operating conditions requiring a current harmonic injection.

The experimental tests have confirmed the validity of the proposed solution. The proposed control technique can annul the low frequency voltage oscillation on the DC-link capacitors when the modulation index is under the modulation limits. The experimental tests have also confirmed that the algorithm provides the best solution, compared to the SVPWM, also when the request is over the limits.



## Chapter 3

# *Detection and Estimation of Magnet Demagnetization in Six- Phase Permanent Magnet Synchronous Motor*

*Multiphase motor drives play a crucial role in high-reliability applications where fault tolerance is an essential requirement to guarantee the operation in critical conditions. In these applications it is very important to check the status of the machine, detect and locate faults.*

*In Permanent Magnet Synchronous Motor (PMSM) the state of health of the rotor magnets can prejudice the behaviour of the machine. The detection of partial demagnetization is a challenging problem that allows to guarantee an appropriate reliability of the machine*

*In this chapter, an analytical study for magnets with parallel magnetization has been developed. A technique able to estimate the length of the pole arc of the rotor magnets has been presented in order to evaluate the state of health of the machine.*

*Experimental tests on a six-phase PMSM with two independent three-phase star-connected stator windings has been performed to verify the feasibility of the proposed technique.*

### 3.1 Permanent Magnet Synchronous Motor

Permanent magnet machines are often used for demanding applications, which require a high torque/current ratio as well as a high-power density. Consequently, online monitoring systems of operating conditions are required.

Due to their inherent characteristics, PMSMs are generally used in applications that do not require a wide range of flux weakening operations. This includes micro-mobility applications such as bicycles, scooters and skateboards. In these motors, investing in high quality permanent magnets increases the performance, efficiency and power density of the motor.

PMSMs are prone to a wide range of faults, such as short circuits, demagnetization, and mechanical faults. Typically, the magnet demagnetization is due to a high magnetic field generated by the stator windings in event of over-currents or short circuits. If the stator magnetic field is greater than the intrinsic coercivity of the magnets, the demagnetization process is irreversible [46]. The demagnetization is often a consequence of several stress factors, such as temperature, intermittent mechanical forces, and corrosion. It is well-known that NdFeB magnets have poor thermal characteristics and are susceptible to corrosion, while rare-earth magnets can partially lose their magnetization level due to fabrication cracks [47].

This thesis analyzes an asymmetrical six-phase Surface Mounted PMSM, which has two independent three-phase star-connected stator windings  $A_1, A_2, A_3$  and  $B_1, B_2, B_3$ , rotated by  $30^\circ$  degrees relative to each other (Fig. 3.1). The mathematical model of this type of electric machine take advantage from the VSD, as previously described in Chapter 1.

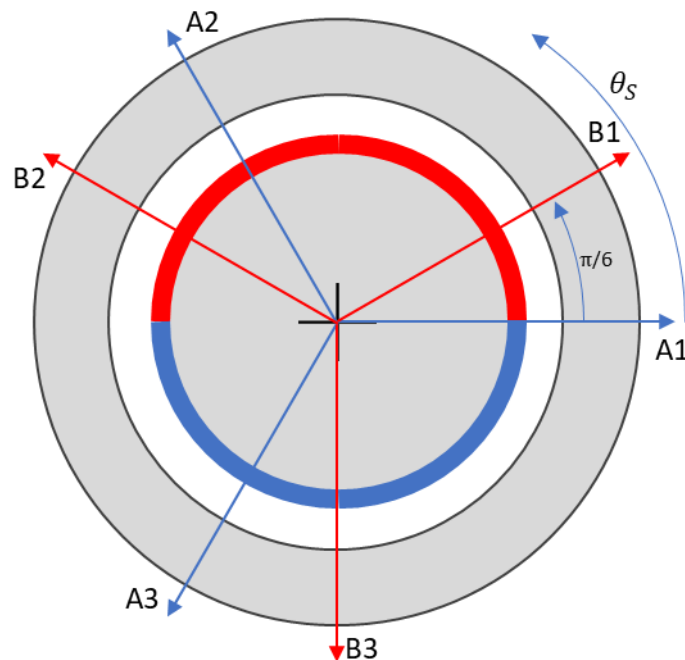


Fig. 3.1 Six-phase PMSM with a spatial shifting of  $\frac{\pi}{6}$  between three-phase windings.

### 3.2 Effect of Demagnetization

Changes in magnet strength and demagnetization of magnets can be caused mainly by two factors:

- Over temperature;
- Overcurrent.

The temperature effect, often reversible, doesn't represent a real danger for the machine's health but reduces temporarily the coercivity of the magnet. Only if the temperature of the magnet exceeds the Curie temperature the demagnetization effect is irreversible. As the temperature increases, the intrinsic coercivity of the magnet decreases. Fig. 3.2 shows the magnetic characteristic for Neodymium-Iron-Boron magnets which are the most used for PMSMs.

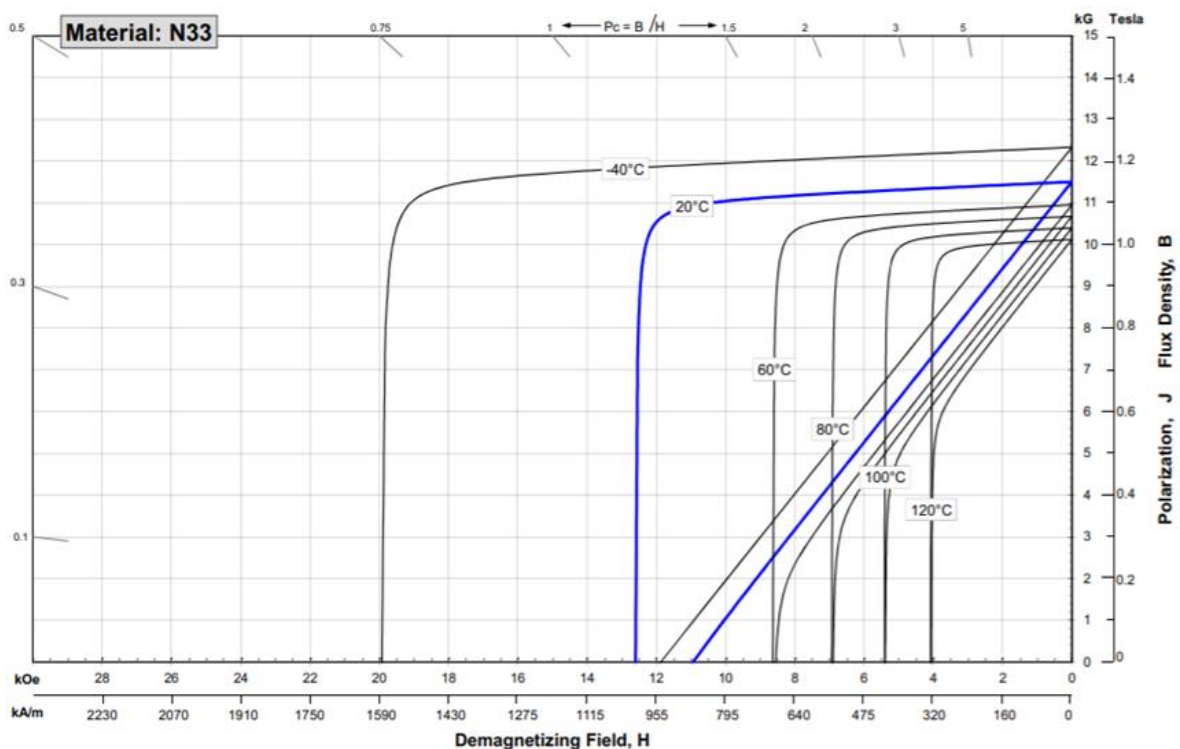


Fig.3.2 Demagnetization curves at various temperatures. [Arnold magnetic technologies].

The overcurrent can be produced by an inter-turn short circuit of stator windings or a heavy overload. In these conditions, there are strong magnetic fields that can reduce the magnetic properties of the rotor magnets. If the magnetic field exceeds the limit of the magnet's coercivity, the magnet loses its magnetic properties. As shown in Fig. 3.2 the limit of the magnet's coercivity depends on the temperature, therefore at high temperature the overcurrent which demagnetizes the magnet decreases.

In this thesis only demagnetization caused by overcurrent is considered. To initially simplify and explain the concept of the demagnetization, only a single pole pair and a linearized representation of the rotor magnets with full pitch is considered.

In Fig. 3.3, the d-q synchronous reference frame and the direction of the two components of the magnetic flux generated by the rotor magnets and the stator windings are represented. The d axis is aligned with the centre of the magnets, and the q axis is shifted by 90° electrical degrees from the d axis. This reference frame is used for field-oriented control where all the control variables are described by constant variables over time.

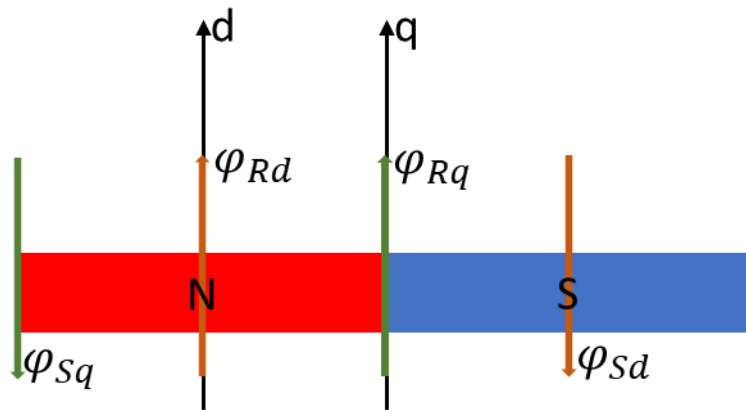


Fig. 3.3 Cross section of the rotor magnets and representation of the synchronous reference adopted.

During the motor operations, the directions of the two components of the magnetic flux generated by the stator are drawn in Fig. 3.3. In overload conditions, the current exceeds the nominal value. The current overload is commonly caused by an anomalous value of the q component of the current while the d component is set to zero. The increase of the q component of the flux generates an intense magnetic field near the edges of magnets.

The intense magnetic field generated in this condition leads to a small demagnetization in the portion of the north or south magnets near the border. The intense magnetic field leads to a local demagnetization because the q component of the magnetic field, as shown in Fig. 3.3, crosses the north and the south of two adjacent magnets. This field, depending on the direction, demagnetizes one of the two poles. The demagnetized portion of the magnet increases as the magnetic field increases.

Typically, magnets do not cover the entire pole arc, therefore, the demagnetization due to the overcurrent affects only a small section of the magnets.

The assumed simplifying hypothesis for analysing the partial demagnetization phenomena is that the demagnetized parts of the magnets are equivalent to air for magnetic purposes. The main effect of demagnetization can be seen as an asymmetrical reduction in the length of both magnets (North and South).

One of the possible representations of the fault is the one illustrated in Fig. 3.4 where the angles  $\gamma_1$  and  $\gamma_2$  indicate the edge of the magnets and where the rotor system reference frame is taken in the middle of the healthy magnet.

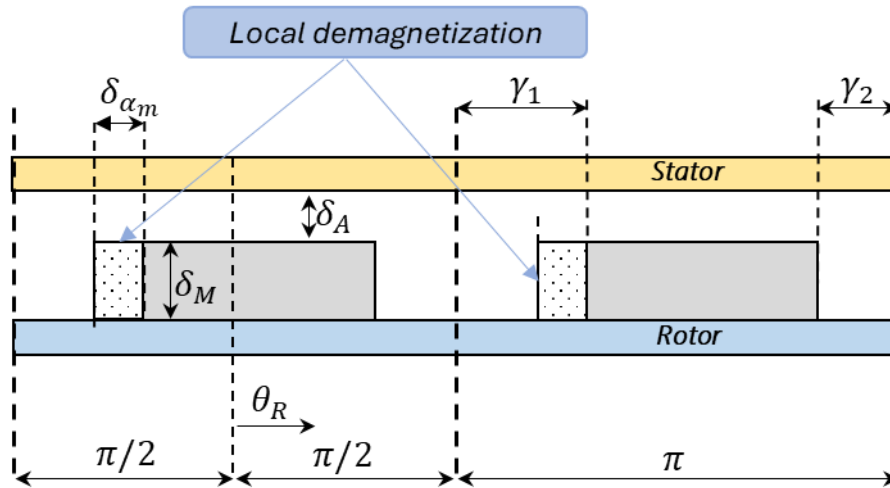


Fig. 3.4 Schematic drawing of a pair of rotor permanent magnets in healthy ( $\alpha_1 = \alpha_2 = \alpha$ ), and demagnetized ( $\alpha_1 > \alpha_2$ ) conditions.

The pole arc of the surface-mounted permanent magnets, in healthy conditions is equal to  $\pi - 2\gamma_2$  because in healthy conditions  $\gamma_1$  and  $\gamma_2$  are equal. This angle represents the shortening angle of the magnets, which is chosen at the design stage to reduce the effect of some magnetic field harmonics at the air gap.

The demagnetization fault reduces the magnet active section by increasing  $\gamma_1$ . Consequently, the length of the magnet is reduced by an angle equal to  $\gamma_1 - \gamma_2$ .

### 3.3 Diagnostic Algorithm

This section defines a strategy for detecting demagnetization in six-phase permanent magnet synchronous motors. To define a strategy, it is necessary analyse the form factor function  $f$  expressed by (1.114), which describes the shortening factor of the magnets for magnets with parallel magnetization.

Expression (1.114) give a singularity when it is necessary to analyse the first harmonic for machines with one pole pairs. In the case of magnets with parallel magnetization and full pitch, in a machine with one pole pairs, the magnets produce a perfectly sinusoidal field. In this machine the other harmonics are present only when the partial demagnetization of the magnets occurs or when the length of the magnets is less than the full pitch of the polar arc.

The expression (1.115) for the first harmonic of a machine with a single pole pair can be evaluated with equation (1.108) and (1.115) introducing  $\rho = 1$  and  $p = 1$ . With these simplifications the shortening factor for the first harmonic can be written as:

$$f(\gamma_1, \gamma_2, 1, 1) = \frac{\pi}{2} - \frac{\gamma_1 + \gamma_2}{2} + \frac{j}{4} \left[ e^{-j2(\frac{\pi}{2} - \gamma_2)} - e^{-j2(-\frac{\pi}{2} + \gamma_1)} \right] \quad (3.1)$$

Generally, equations (1.116) and (3.1) provide complex solutions but, choosing a particular reference frame centred to the middle of the magnet, as shown in Fig. 3.4, the imaginary component is equal to zero.

The representation of the function  $f$  is shown in Fig. 3.5. The figure describes the real part of (3.1) and (1.115) for a machine with one pole pair. As previously mentioned, when the rotor magnets have a full pitch length, only the first harmonic is different from zero. It is possible to consider the function  $f$  as a shortening factor of the rotor magnets with parallel magnetization. The trend of the harmonic coefficient of  $f$  is shown in Fig 3.5. The harmonics components are reported in p.u. respect the value of the first harmonic in case of full pitch length.

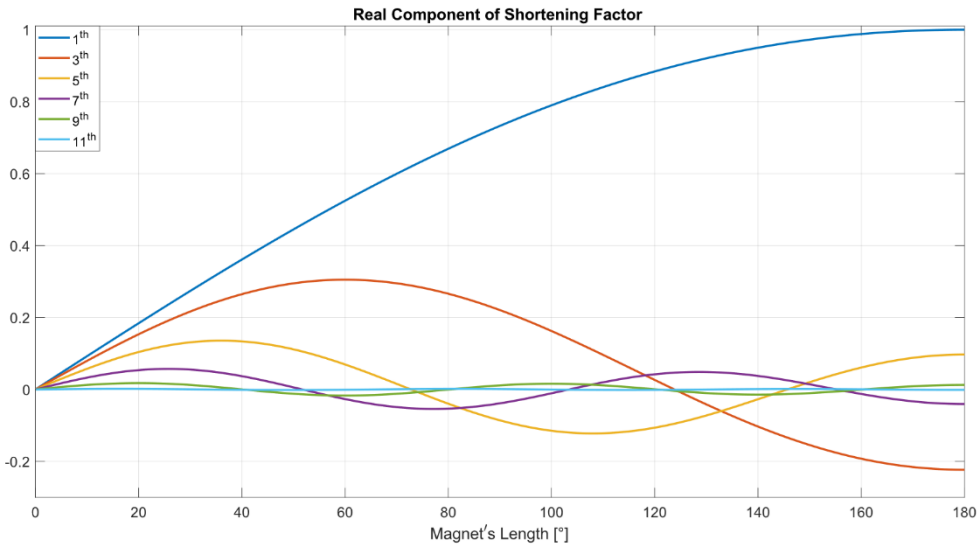


Fig. 3.5 Harmonic coefficient of the shortening factor of the rotor magnets for a two-pole machine with parallel magnetization.

As can be seen, when the magnet length cover the entire polar arc ( $180^\circ$ ), only the first harmonic is present.

When the length of the rotor magnets is less than the full pitch also the other harmonics are produced by the magnets. As can be seen, only the first harmonic follows a monotone trend in the range  $[0, \pi]$ , whereas all the other assume both positive and negative values.

As known by the design relationships, the mechanical length of the magnets that maximize the  $\rho^{th}$  harmonic amplitude is equal to  $\frac{\pi}{\rho}$ . In the range  $[0, \pi]$ , the  $\rho^{th}$  harmonic has  $\frac{\rho}{2}$  periods. The amplitude of the harmonic coefficient follows an almost sinusoidal trend.

The proposed diagnostic algorithm can be deduced by observing Fig. 3.5. For each magnet length there is a specific value of harmonics produced by the magnets. By observing the amplitude of a

specific harmonic, it is possible to determine the state of health of the rotor magnets and found the portion of magnets lost during the fault.

The proposed solution is based on the observation of the fifth harmonic produced by the magnets. This harmonic is mapped into sub-space five, whose current space vector is usually imposed equal to zero by the motor control system.

With a Proportional Integral (PI) regulator implemented in a reference frame synchronous with this harmonic the amplitude of the back-Electro Motive Force of the machine can be estimated.

The voltage equation of the machine expressed for subspace five (1.136) is reported here.

$$\bar{v}_{S5} = R_s \bar{i}_{S5} + \frac{d\bar{\varphi}_{S5}}{dt} \quad (3.2)$$

When  $\bar{i}_{S5}$  is set to zero,  $\bar{v}_{S5}$  represents the magnet's contribution.

The motor control scheme sets to zero the stator current space vector  $\bar{i}_{S5}$ . Under these conditions, the outputs of the PI regulators of the space five measure the machine's back-EMF.

The motor back-EMF depends not only on the harmonic coefficient of the rotor but also on the winding factor of the stator. The stator winding factor is evaluated with the relations (1.11) (1.12) (1.13).

In the LEMAD laboratory there are two six-phase PMSMs with the same stator structure but with a different length of the rotor magnets. This experimental set-up allows to simulate a partial demagnetization fault. The magnets length in the first machine is 150 electrical degrees and in the other, which represents the faulty machine, 130 electrical degrees. When the local demagnetization of the rotor magnet occurs, the control system reference frame is no longer centred to middle of the magnetic field produced by the rotor magnets. That means that the function  $f$  has both the real and imaginary contribution in this condition. To overcome this problem, it is convenient to evaluate the trend of the module of the function  $f$  (1.114). When the local demagnetization of the rotor magnet occurs, the synchronous reference frame of the control system must be rotated, and the previous reference system can no longer be used due to the magnetic dissymmetry of the fault. This rotation prevents function  $f$  from having complex solutions, but it can be avoided as the amplitude of function  $f$  is considered.

To understand how the proposed solution works it is necessary to analyse the fifth harmonic of the shortening factor of the rotor magnets for a machine with two pole pairs expressed by (1.114).

Taking the reference frame of the system centre to the middle of the rotor magnets with full pitch, as shown in Fig. 3.4, and considering the magnet demagnetization asymmetry, the shortening factor has a real and imaginary component.

The trend of the real part of the fifth harmonic of (1.114) for a machine with two pole pairs when the stator winding factor is taken into account, is shown in Fig. 3.6.

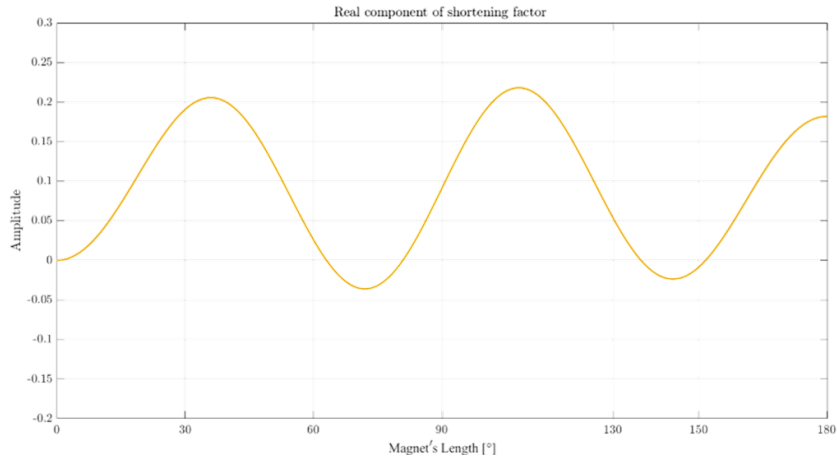


Fig. 3.6 Real component of the fifth harmonic coefficient for a motor with two pole pairs when a rotor magnet demagnetization occurs.

The corresponding imaginary component is shown in Fig. 3.7.

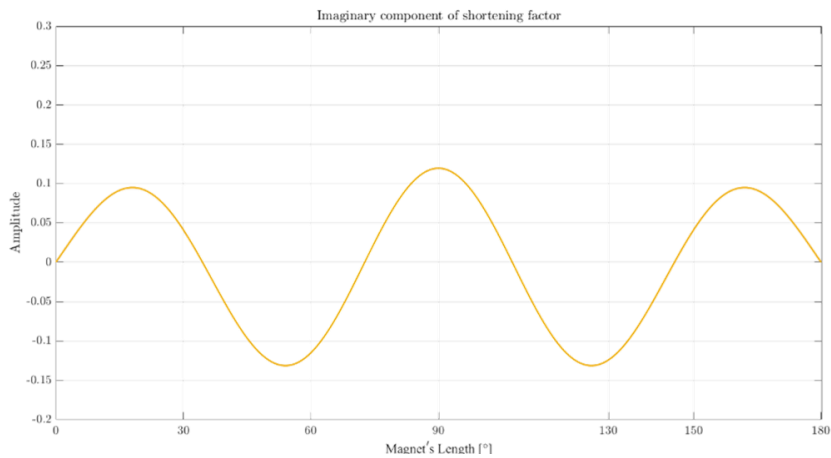


Fig. 3.7 Imaginary component of the fifth harmonic coefficient for a motor with two pole pairs when a rotor demagnetization occurs.

It is also possible to evaluate the module of the fifth harmonic of the shortening factor of the rotor magnets, as shown in Fig. 3.8.

It is possible to observe that none of the three components is monotonous in the range of interest for this machine [130°,155°] which complicates the determination of the length of the magnet in this interval.

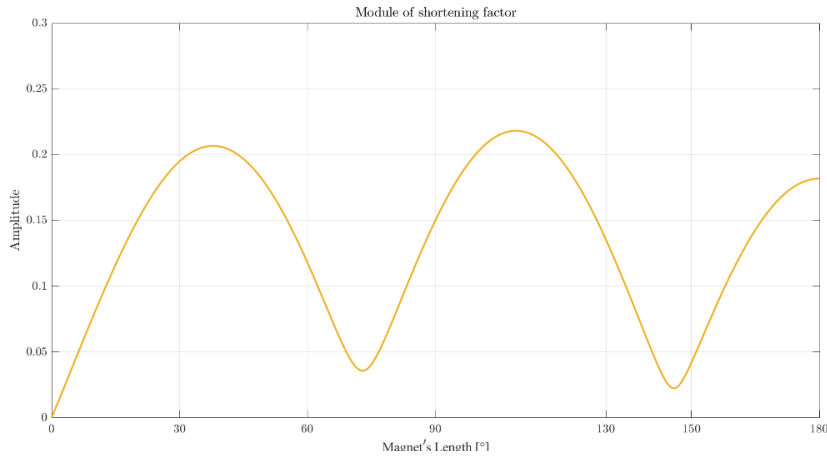


Fig. 3.8 Module of the fifth harmonic factor for a motor with two pole pairs when a rotor demagnetization occurs.

The trend of the module, Fig. 3.8, contains part of the information contained into the real and imaginary components. For this reason, the module of the fifth harmonic of the shortening factor of the rotor magnets has been used to detect the local demagnetization in the proposed algorithm.

To obtain a bijective trend in the interval  $[150^\circ, 130^\circ]$  it is necessary to add the value of the function  $f$  when the magnet is healthy ( $150^\circ$ ). With this expedient a new monotone function in a wider range can be obtained.

The compensated function is calculated as:

$$f(\gamma_1, \gamma_2, 2,5) = f(\gamma_1, \gamma_2, 2,5) - f(15,15,2,5) \tag{3.3}$$

The comparison between the compensated curve and the effective curve is reported in Fig. 3.9.

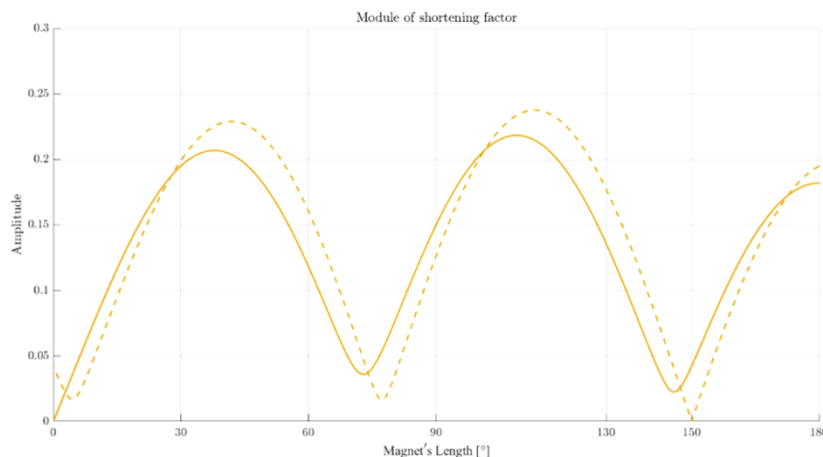


Fig. 3.9 Comparison between the module of the fifth harmonic factor before the compensation (solid line) and after the compensation (dashed line) of the point at  $150^\circ$ .

As can be seen, the compensated curve, the dashed line in Fig. 3.9, is monotonous in the interval  $[110^\circ, 150^\circ]$  that means that, if it is known the value of  $|\bar{\varphi}_{s5}|$  it is possible to determine the arch of the magnet and the lost portion of the magnet after the fault with an appropriate PI regulator.

### 3.4 Control Scheme

This section presents the control scheme capable of detecting the demagnetization of the rotor magnets and estimating the severity of the fault. Fig. 3.10 shows the motor control scheme.

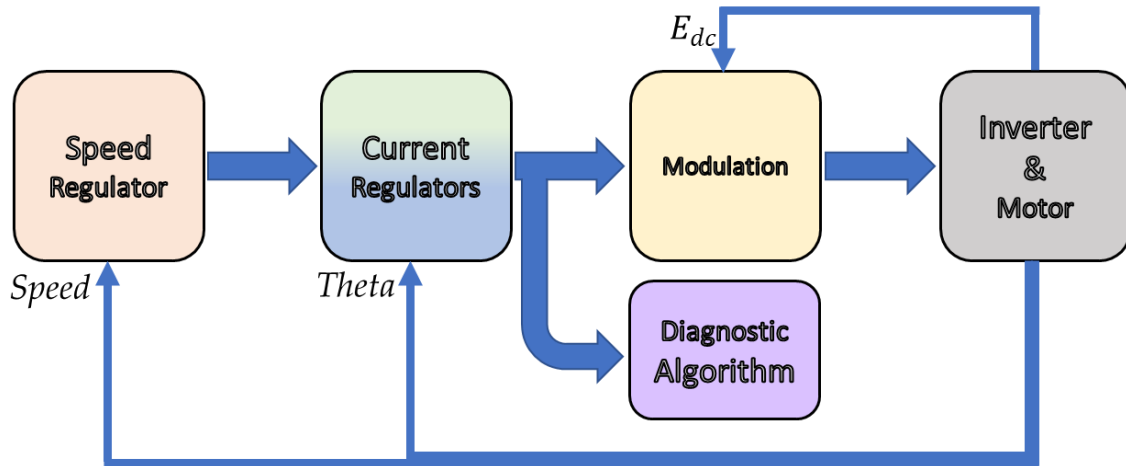


Fig. 3.10 Control scheme of the six-phase PMSM.

The control scheme has been divided into fundamental blocks, Speed Regulator, Current Regulators, Diagnostic Algorithm, Modulation and Inverter and Motor.

#### 3.4.1 Speed Regulator

The block diagram of Fig. 3.11 illustrates the speed controller (a). In cascaded control, the bandwidth of the outer loop should be lower than the bandwidth of the inner loop. The torque contribution is controlled by a traditional direct field oriented control scheme implemented in a reference frame aligned with the rotor flux  $\bar{\varphi}_{R1}$ . The error between the reference speed  $\omega_{m,ref}$  and the actual one is sent to the PI controller (a), which generates the setpoint  $i_{S1q,ref}$ . The setpoints  $i_{S1d,ref}$ ,  $i_{S5d,ref}$ ,  $i_{S5q,ref}$  are fixed to zero in order to annul the current in sub-space five.

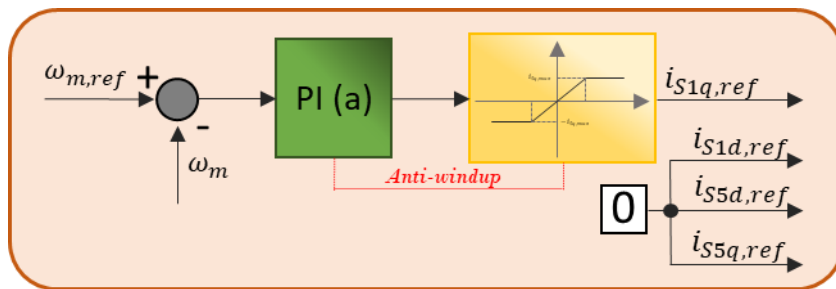


Fig. 3.11 Speed regulator.

### 3.4.2 Current Regulators

The measured phase currents were transformed with the appropriate Clarke and Park transformation to obtain the current space vector in the d-q reference. The measured current is compared with the reference current generated by the speed regulator to obtain the current error. Each component of the current error is supplied in input to the PI regulators. For space one, the current error is annulled by the PI regulators (b) (c) (d) (e), while for space five, the current error is cancelled by the PI regulators (f) (g) (h) (i). The outputs of the PI regulators enter in the following block to compensate the Back-emf to increment the dynamic response of the PI. Finally, the voltage space vectors  $\bar{V}_{S1dq}$  and  $\bar{V}_{S5dq}$  are composed as sum of different harmonic components.

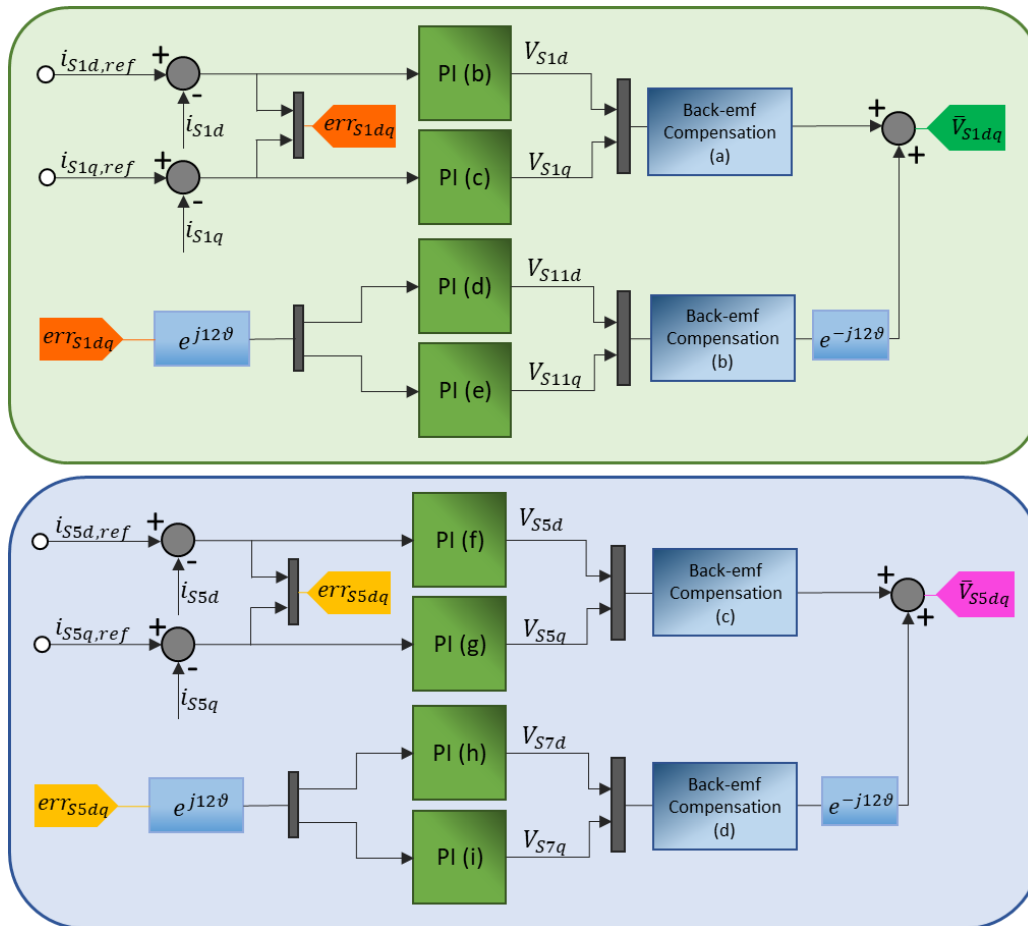


Fig. 3.12 Current regulators of sub-space one and five.

### 3.4.3 Diagnostic Algorithm

The voltage space vector  $\bar{V}_{S5dq}$  is used to analyse the motor state of health with the diagnostic algorithm shown in Fig. 3.13.

The fifth harmonic of the magnets flux is obtained dividing the voltage space vector  $\bar{V}_{S5dq}$  by the angular speed  $\omega$ . The feedforward compensation of the flux produced by the healthy motor increases the response dynamics of the diagnostic algorithm and aligns the reference system.

As previously shown, the function that describes the magnets flux can have real and imaginary components if the reference frame is not aligned to the centre of the magnetic field produced by the magnets. To avoid this the module of the function has been used.

The estimated magnetic flux and the reference magnetic flux of the magnet model are used to obtain the flux error. This error is the input of the PI regulator which provides the value of the angular length of rotor magnets  $\theta_{mag}$ . The length of the magnet is used by the magnetic model to calculate the reference flux.

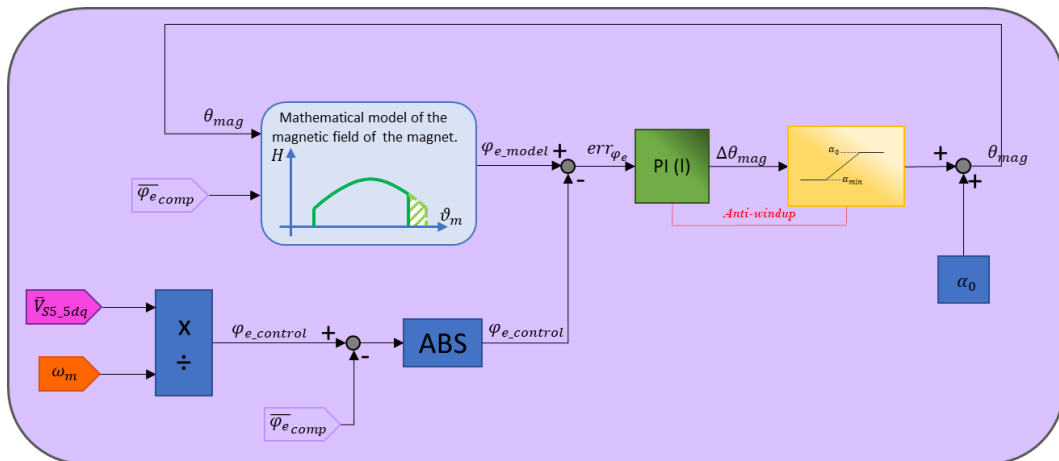


Fig. 3.13 Diagnostic algorithm.

### 3.4.4 Modulation Block

The modulating signals can be synthesized through a pulse-width modulation technique in a special block shown in Fig. 3.14. The SVPWM block ensures the operation of the inverter in the linear modulation region [48].

The mechanical position of the rotor is measured by an incremental encoder, while the mechanical speed is obtained as the derivative of the mechanical angle.

The actual value of the current space vectors has been obtained by measuring the stator phases current.

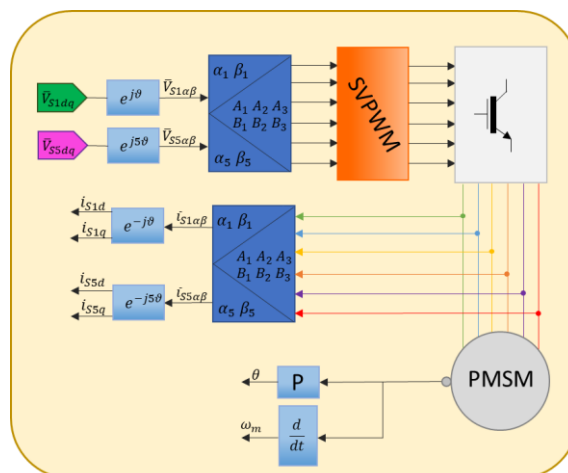


Fig. 3.14 Modulation and transformation blocks.

### 3.5 Experimental Results

In order to validate the proposed diagnostic algorithm, some tests have been carried out at the LEMAD laboratory of Bologna. For the tests, two six-phase PMSMs prototypes, have been used, The prototypes shown in Fig. 3.5 have the same stator characteristics, and the rotors have the same type of magnets but with different length. The first motor is the healthy one and its parameters are listed in Table. 3.1. The second motor has the same parameters of Table. 3.1, but the pole arc of the rotor magnets has been reduced by  $10^\circ$  under all poles for simulating the demagnetization fault.

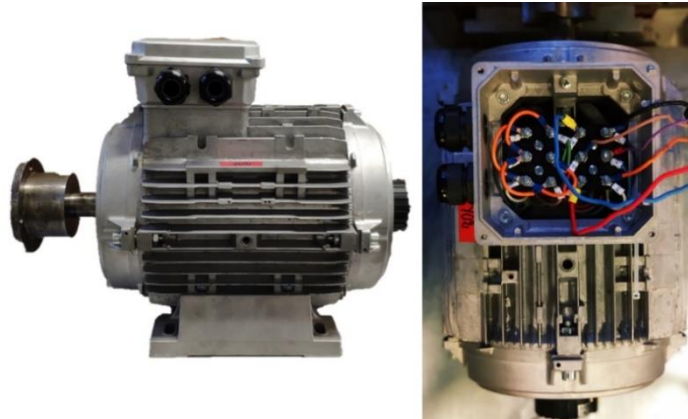


Fig. 3.15 Machine prototypes of PMSMs.

|                     |               |                         |          |
|---------------------|---------------|-------------------------|----------|
| Phase resistance    | 0.36 $\Omega$ | Magnet pole-arc         | 75.0°    |
| Pole number         | 4             | Magnet radial thickness | 4 mm     |
| Phase inductance    | 1.44 mH       | Magnetization type      | Parallel |
| Stator inner radius | 150 mm        | Rated Speed             | 1000 Rpm |
| Stator outer radius | 240 mm        |                         |          |
| Slot number         | 48            |                         |          |

Tab. 3.1 Parameters of the Six-Phase Surface Mounted PMSM.

Fig. 3.16 shows the waveforms of the electromotive force at no-load operating conditions (1000 rpm) of the healthy motor (a) and the faulty one (b). The corresponding trajectories of the electromotive force space vectors  $\bar{e}_{s1}$ ,  $\bar{e}_{s3}$ , and  $\bar{e}_{s5}$  in the  $\alpha$ - $\beta$  plane are included.

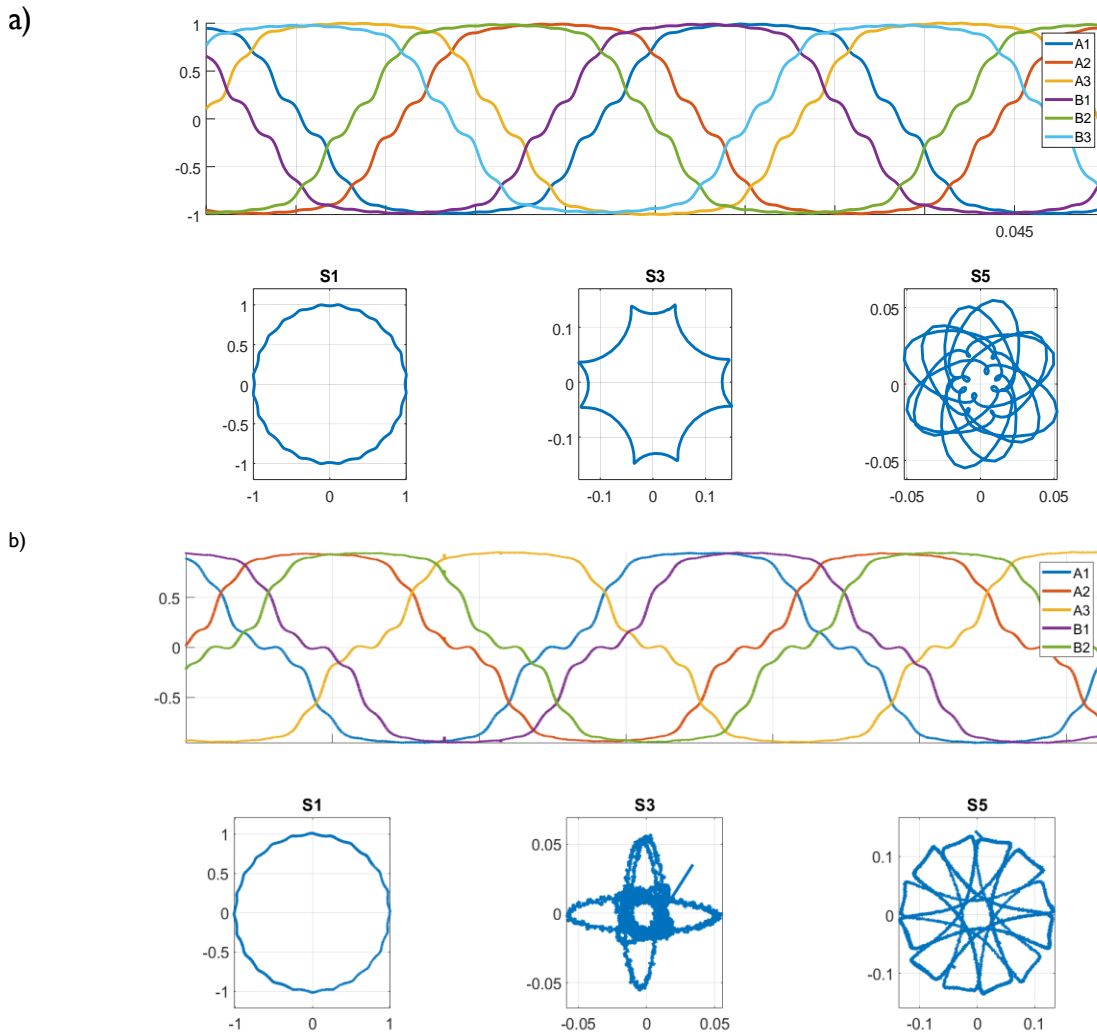


Fig.3.16 Experimental waveforms of the back-emfs in healthy conditions (a) and with partial demagnetization (b), and representation of the corresponding space vectors in sub-spaces 1, 3 and 5.

### 3.6 Experimental Tests on the Healthy Machine

In order to validate the effectiveness of the proposed method, Fig. 3.17 shows the activation of the proposed algorithm for the detection and evaluation of the partial demagnetization of the rotor magnets when the machine operates at 1000 RPM with 10 Nm.

After the activation of the diagnostic algorithm, the length of the rotor magnets is estimated, as can be seen by the blue line in Fig. 3.17 obtained by using the dSPACE for evaluating the trend of the internal variables. The estimated length is 145 electrical degrees. In this condition, the machine is healthy, and the algorithm has an error of just 2.5 mechanical degrees, which may be due to various factors not taken into consideration.

To demonstrate the validity of the proposed solution for the estimation of the pole arc length of the rotor magnets some tests have been carried out to stress the algorithm in different operating conditions.

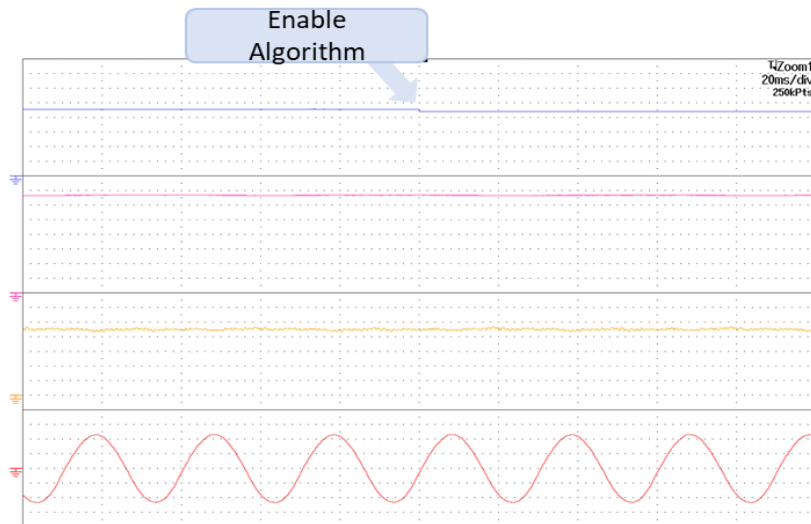


Fig. 3.17. Activation of the diagnostic algorithm at 1000 rpm with 10 Nm. Estimation of the pole arc of the rotor magnets ( $10^\circ/\text{div} + 100^\circ$  of offset), rotor speed (150 rpm/div), current  $i_{sq1}$  (1A/div), phase current  $i_{B1}$  (2A/div).

Fig. 3.18 shows a torque transient to verify the insensitivity of the proposed solution to the variation of the phase currents. The required torque rapidly changes, from 10 Nm to working near no-load conditions. The torque variation can be observed from the variation of the current  $i_{sq1}$ , the orange line in Fig. 3.18, that is proportional to the motor torque.

As can be seen, also in this condition, the algorithm can correctly estimate the pole arc length of the rotor magnets without significant variations during the torque transient.

This confirms the insensitivity of the proposed solution to the phase currents variation. This means that the control system is able to keep the current space vector five equal to zero in each condition and the outputs of the PI regulators analysed by the algorithm represent the effective back-EMF of the machine.

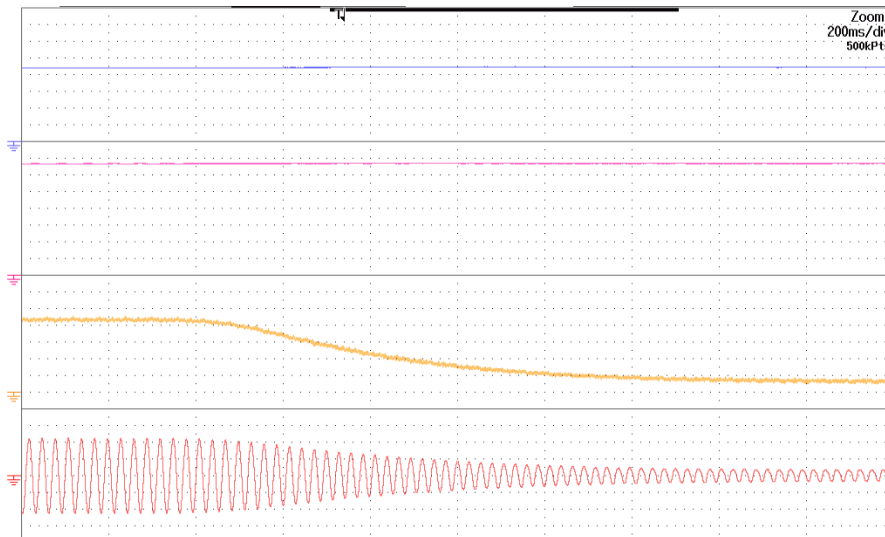


Fig. 3.18. Torque transient from 10 Nm to 2 Nm. Estimation of the pole arc of the rotor magnets ( $10^\circ/\text{div} + 100^\circ$  of offset), rotor speed (150 rpm/div), current  $i_{sq1}$  (1A/div), phase current  $i_{B1}$  (2A/div).

The experimental tests found that the minimum speed that allows for estimating the length of the magnet is 300 rpm. Below this speed, the output of PI regulators is so low that the effect of the inverter non-linearities does not allow to correctly estimate the back-EMF.

The algorithm has been tested during a speed transient from 300 rpm to 1000 rpm. Under these test conditions, the load torque changes as the rotor speed changes.

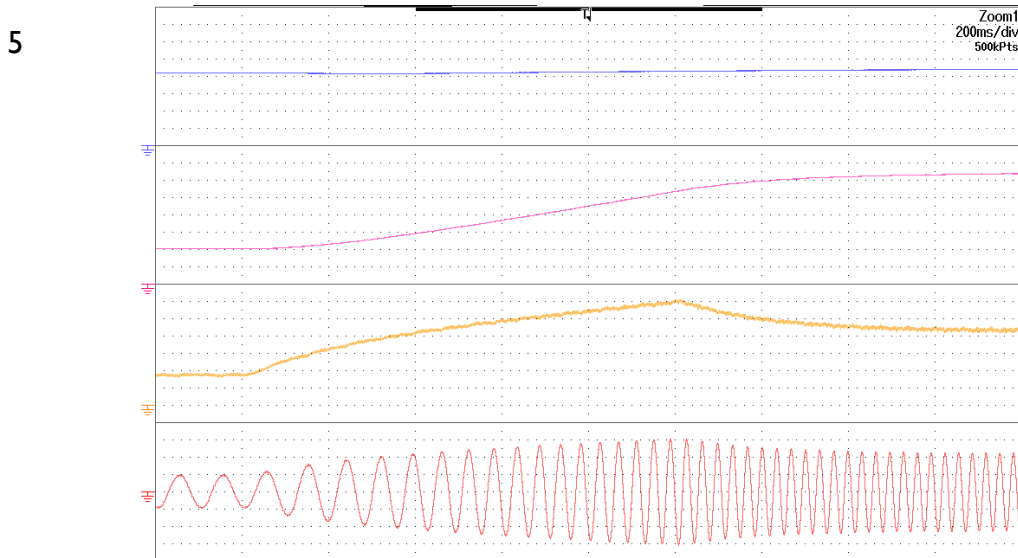


Fig. 3.19. Speed transient from 300 rpm to 1000 rpm. Estimation of the pole arc of the rotor magnets ( $10^\circ/\text{div} + 100^\circ$  of offset), rotor speed ( $150 \text{ rpm}/\text{div}$ ), current  $i_{sq1}$  ( $1\text{A}/\text{div}$ ), phase current  $i_{B1}$  ( $2\text{A}/\text{div}$ ).

Fig. 3.19 shows how the algorithm is insensitive to the variation of rotor speed. During the speed transient, the rotor magnet's pole arc value presents a little variation due to the regulator dynamic. In this condition, the PI must keep zeroing the current space vector five to obtain the estimation of the flux generated by the rotor's magnets.

### 3.7 Experimental Tests on the Faulty Machine

To obtain the correct test conditions, the alignment of the faulty machine was changed to obtain the same alignment used with the healthy machine. In particular, the alignment of the reference frame used by the control system has been rotated by half of the demagnetization angle. Under these conditions, the proposed algorithm must estimate the value of the magnet portion lost during the fault and rotate the reference frame of the control system to ensure the correct alignment.

The first test carried out on the faulty machine (Fig. 3.20), has been the enabling of the proposed algorithm to detect and evaluate the partial demagnetization of the rotor magnets when the machine works at 1000 rpm with 10 Nm.

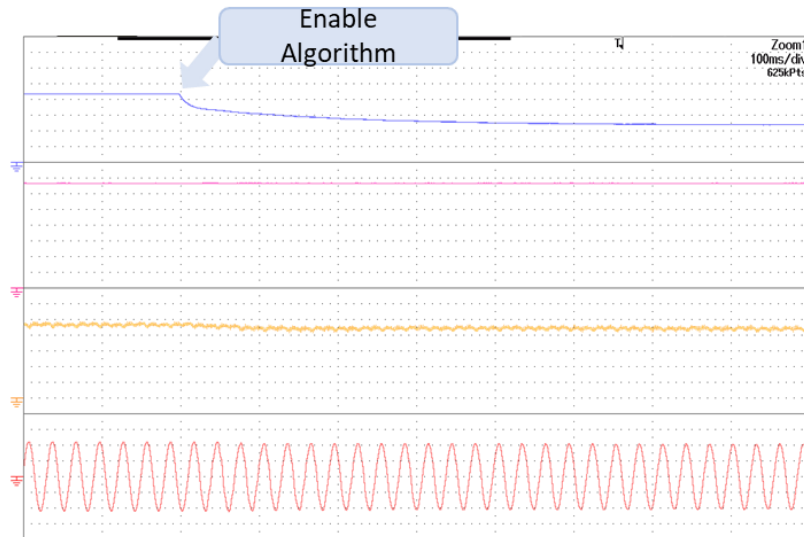


Fig. 3.20. Activation of the diagnostic algorithm at 1000 rpm with 10 Nm. Estimation of the pole arc of the rotor magnets ( $10^\circ/\text{div} + 100^\circ$  of offset), rotor speed ( $150 \text{ rpm}/\text{div}$ ), current  $i_{sq1}$  ( $1 \text{ A}/\text{div}$ ), phase current  $i_{B1}$  ( $2 \text{ A}/\text{div}$ ).

After a rapid transient following the activation due to the PI dynamics, the algorithm provides the correct pole arc of the rotor magnets. At the same time, the reference frame alignment is rotated by an angle equal to half of the demagnetization angle, as already mentioned.

The new alignment affects the value of  $i_{sq1}$ . After the activation of the algorithm the current  $i_{sq1}$  decreases until it reaches the condition of maximum ratio Nm / A as shown in Fig. 3.20.

Also in this case some tests for validating the proposed solution in different work conditions have been carried out. Fig. 3.21 shows the torque transient in the same operating condition of the test described in Fig. 3.19.

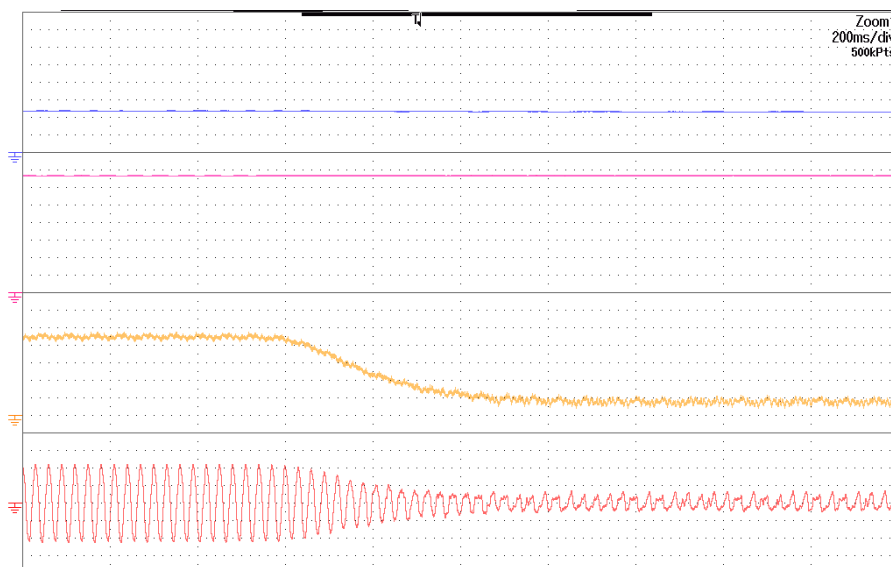


Fig. 3.21. Torque transient from 10 Nm to 2 Nm. Estimation of the pole arc of the rotor magnets ( $10^\circ/\text{div} + 100^\circ$  of offset), rotor speed ( $150 \text{ rpm}/\text{div}$ ), current  $i_{sq1}$  ( $1 \text{ A}/\text{div}$ ), phase current  $i_{B1}$  ( $2 \text{ A}/\text{div}$ ).

The value of the estimated pole arc of the rotor magnet doesn't change significantly during the torque transient. The algorithm estimates a pole arc equal to 125 electrical degrees in the transition from full-load to a no-load operating conditions. This result corresponds to a demagnetization angle equal to 20 electrical degrees (or 10 mechanical degrees).

The last test, described in Fig. 3.22, is a speed transient at full-load from 300 rpm to 1000 rpm.

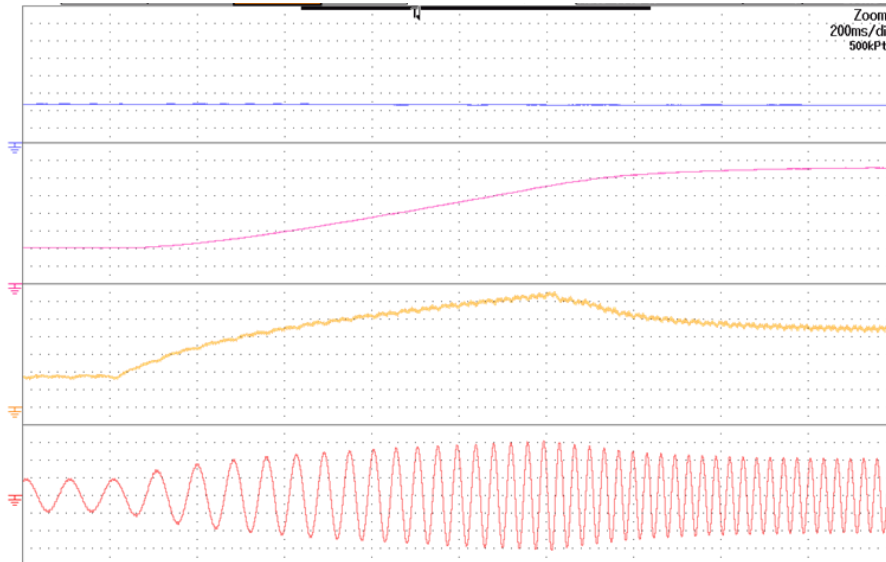


Fig.3.22. Speed transient from 300 rpm to 1000 rpm. Estimation of the pole arc of the rotor magnets ( $10^\circ/\text{div} + 100^\circ$  of offset), rotor speed ( $150\text{ rpm}/\text{div}$ ), current  $i_{sq1}$  ( $1\text{A}/\text{div}$ ), phase current  $i_{B1}$  ( $2\text{A}/\text{div}$ ).

Also in this case the algorithm proved to be insensitive to the speed variation. Only a little variation due to the PI dynamic is appreciable, that does not alterate the estimation of the pole arc length of the magnet as shown by the blue line in Fig. 3.22.

### 3.8 Conclusions

*In this chapter an algorithm able to estimate the length of the pole arc of the rotor magnets in a six-phase PMSM machine has been presented.*

*An analytically study of the rotor magnetic field has been illustrated.*

*The algorithm exploits the analysis of the harmonics produced by the rotor magnets and evaluates the motor back-EMF.*

*Finally, some test have been carried out in stationary and transient conditions on two six-phase PMSMs prototypes to validate the proposed solution.*

*The speed limit that allows the algorithm to work correctly is 300 rpm.*

*The experimental tests confirmed the validity of the proposed solutions. The proposed algorithm can estimate the correct length of the pole arc of the rotor magnets in different operating conditions.*

# Chapter 4

## *Overmodulation Strategies for Five-Phase Inverters*

*This chapter aims to fully analyse all available possibilities of modulation for five-phase inverters. A definition of the new region that expands the traditional linear modulation region, known from three-phase systems, is presented. The new region is called extended linear modulation because it allows obtaining an extended linear modulation region by using the degrees of freedom available in multi-phase systems. Furthermore, a generalisation for a five-phase inverter of the principal and consolidated overmodulation techniques is presented. All the proposed solutions are analysed with the space vector decomposition.*

*Experimental tests have validated the domain of the proposed extended linear modulation region on a five-phase induction motor. Other experimental tests have been carried out to compare the different modulation techniques analysed. A comparison of the distortion introduced by the different techniques is shown.*

*The proposed solution is valid for a five-phase motor drive where the control system acts on the quantities in the  $\alpha_1 - \beta_1$  plane, whereas the quantities in the  $\alpha_3 - \beta_3$  are set to zero. The presented solution allows to fully exploit the voltage of the DC-bus and improve the performance of the multi-phase drives.*

## 4.1 Overmodulation

The voltage domain of multi-phase converters includes two overmodulation regions. The first one, which is here called the extended linear region, has no counterpart in three-phase inverters. It is defined as the operating condition where the converter can generate the reference voltage vector in  $\alpha_1 - \beta_1$  space, but the voltage vectors in the auxiliary spaces cannot be kept at zero.

The second operating area is the so-called overmodulation region, where the match between the reference voltage in  $\alpha_1 - \beta_1$  space and the actual voltage can be only approximative.

In the overmodulation region, the inverter fully exploits the dc-link voltage, which can provide a significant voltage improvement in motor drive applications. As a consequence, to operate in the overmodulation region, a low-frequency distortion in the output voltages is introduced. In this case, an output filter can be added to reduce the harmonics of the output current and enhance the exploitation of the dc-bus [49].

For this reason, different strategies have been developed to better approximate the reference voltage space vector and to improve the performance of the motor drive [50], [51].

## 4.2 Modulation Regions in Five Phase Inverters

To describe all the available modulation regions in five-phase inverters, it is necessary to define the modulating signals.

$$m_{k,ref} = m_0 + \frac{V_{kref}}{E_{DC}} \quad k = 1, 2, 3, 4, 5. \quad (4.1)$$

where  $E_{DC}$  is the DC-link voltage and  $V_{kref}$  is the reference load voltage of the  $k^{th}$  phase and  $m_0$  is the homopolar component of the modulating signals.

To not incur into overmodulation, the modulating signals must satisfy the following constraints:

$$m_k \in [0,1] \quad \forall k \quad (4.2)$$

First of all, the limits of the linear modulation region must be determined. In other words, the greatest magnitude of the voltage space vector in  $\alpha_1 - \beta_1$  plane should be evaluated for each angle, when the voltage space vector in  $\alpha_3 - \beta_3$  plane is fixed to zero.

By applying the definitions of space vectors and zero-sequence component presented in the first chapter to the modulating signals  $m_k$  ( $k=1, \dots, 5$ ) of the inverter legs of a five-phase inverter, it is possible to define the zero-sequence component  $m_0$  and the multiple space vectors  $\bar{m}_1$  and  $\bar{m}_3$ .

$$\bar{m}_1 = \frac{2}{5} [m_1 + m_2 \bar{\alpha}_5^1 + m_3 \bar{\alpha}_5^2 + m_4 \bar{\alpha}_5^3 + m_5 \bar{\alpha}_5^4] \quad (4.3)$$

$$\bar{m}_3 = \frac{2}{5} [m_1 + m_2 \bar{\alpha}_5^3 + m_3 \bar{\alpha}_5^1 + m_4 \bar{\alpha}_5^4 + m_5 \bar{\alpha}_5^2] \quad (4.4)$$

$$m_0 = \frac{2}{5} [m_1 + m_2 + m_3 + m_4 + m_5] \quad (4.5)$$

where:

$$\bar{\alpha}_5 = e^{\frac{j2\pi}{5}} \quad (4.6)$$

The inverse transformation is:

$$m_k = m_0 + \bar{m}_1 \cdot \bar{\alpha}_5^{(k-1)} + \bar{m}_3 \cdot \bar{\alpha}_5^{3(k-1)} \quad k = 1, 2, 3, 4, 5. \quad (4.7)$$

The relationships between modulating signals and reference phase voltages, in terms of space vectors and zero-sequence components, are the following:

$$\bar{m}_{\rho,ref} = \frac{\bar{v}_{\rho,ref}}{E_{DC}} \quad \rho = 0, 1, 3. \quad (4.8)$$

To obtain the maximum magnitude of the modulating signal space vector  $\bar{m}_1$  in the  $\alpha_1 - \beta_1$  plane, for each argument, when the voltage space vector  $\bar{m}_3$  is fixed to zero is necessary to verify the (4.2) constrain. Conditions (4.2) can be satisfied only if the following constraints are valid:

$$|m_h - m_k| \leq 1 \quad \forall h, \forall k | h \neq k \quad (4.9)$$

These inequalities should be verified for each value of  $k$  and  $h$  and assert that the maximum distance among the modulating signals must not exceed 1. To proceed with the analysis, it is useful to sort the signals  $m_k$  ( $k = 1, 2, \dots, 5$ ) in ascending order. Let L, D, M, U and H (from the initials of the words low, down, medium, up, high) be the indexes of the ordered modulating signals so that

$$m_L \leq m_D \leq m_M \leq m_U \leq m_H \quad (4.10)$$

By using this notation, it is straightforward to prove that (4.9) is equivalent to:

$$m_H - m_L \leq 1 \quad (4.11)$$

In other words, a converter operates in the linear modulation region if the difference between the highest ( $H^{th}$ ) and lowest ( $L^{th}$ ) modulating signal is lower than one and the value of  $m_0$  is chosen in compliance with the constraints.

The expression (4.11) can be used to find the limit of the linear modulation region. Introducing the inverse transformation of the space vector of the modulating signal  $\bar{m}_1$  in (4.11) leads to:

$$\bar{m}_1 \cdot (\bar{\alpha}_5^{(H-1)} - \bar{\alpha}_5^{(L-1)}) \leq 1 \quad (4.12)$$

By drawing in the plane the five vectors  $\bar{\alpha}_5^{k-1}$  (where  $k=1, 2, 3, 4, 5$ ) and their respective opposite, it is possible to detect ten sectors that are identified by a specific pair of vectors  $\bar{\alpha}_5^{(L-1)}$  and  $\bar{\alpha}_5^{(H-1)}$ .

The equality obtained from (4.12), evaluated in the first sector and introducing (4.6), assumes the following expression:

$$\bar{m}_1 \cdot (e^0 - e^{j\frac{6\pi}{5}}) = 1 \quad (4.13)$$

Eq. (4.13) describes the projection of the vector  $\bar{m}_1$  on a segment with slope equal to  $\frac{\pi}{10}$ .

With some geometric considerations, it is possible to observe that the segment described by (4.13) and shown in Fig. 4.1 represents one side of a regular decagon. The internal angles of a regular decagon are equal to  $2\frac{\pi}{5}$ , which is half of the value of the supplementary angle of the slope angle of the red segment in Fig. 4.1.

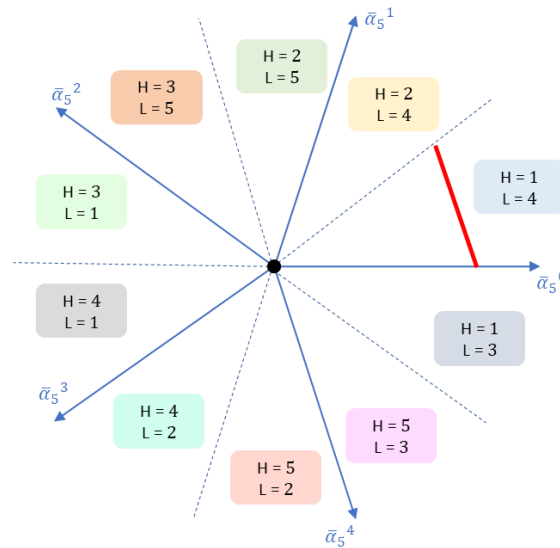


Figure 4.1. Definition of the ten sectors in the complex plane.

By generalizing the concept for each sector, it is possible to obtain the regular decagon shown in Fig. 4.2, where each side is described by (4.12). The regular decagon of Fig. 4.2 represents the limit of the linear modulation region in the  $\alpha_1 - \beta_1$  plane when only the space vector  $\bar{m}_1$  is different to zero. The length of the green arrow, that connects the origin to the vertex of the decagon is equal to 0.5528.

The maximum circle inscribed to the regular decagon is the blue circle shown in Fig. 4.2. The radius of the circle, which is represented by the blue arrow in Fig. 4.2, is obtained by the following relationship [52]:

$$r_1 = \frac{1}{2 \cos\left(\frac{\pi}{10}\right)} \quad (4.14)$$

As long as the modulating signal space vector  $\bar{m}_1$  remains within the regular decagon of Fig. 4.2, and the voltage space vector  $\bar{v}_3$  is fixed to zero, the inverter operates in the linear modulation region.

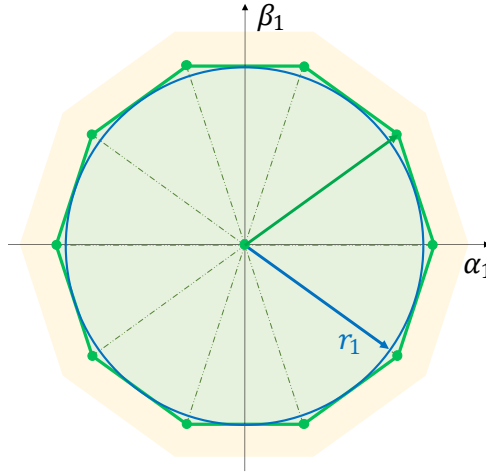


Figure 4.2. Limits of the linear modulation region for five-phase inverters.

Equation (4.11) represents the necessary and sufficient condition for linear modulation. It can be used to evaluate the effect of the  $m_0$  component on the linear modulation region. Equation (4.11) can be rewritten, by exploiting the inverse Clarke transformation, in the following form:

$$m_0(1 - 1) + \bar{m}_1 \cdot (\bar{\alpha}_5^{(H-1)} - \bar{\alpha}_5^{(L-1)}) + \bar{m}_3 \cdot (\bar{\alpha}_5^{3(H-1)} - \bar{\alpha}_5^{3(L-1)}) \leq 1 \quad (4.15)$$

The effect of the variation of  $m_0$  is a rigid translation of all the modulating signals, therefore  $m_0$  cannot change the respective distance between the modulating signals which would allow affecting the range of modulation. Some values of  $m_0$  can be used to optimize some characteristics of the converter, such as the switching losses [53], the spectrum of the output current [54], [55], the sizing of the dc-link capacitors, and the common-mode current [56]. Conversely,  $\bar{m}_3$  can be selected to extend the boundaries of the admissible domain of  $\bar{m}_1$ .

### 4.3 Extended Linear Modulation Region

In general, in multi-phase inverters, the additional degrees of freedom allow reaching the greatest magnitude of the fundamental space vector  $\bar{m}_1$  for each argument by introducing an adequate space vector in an auxiliary plane to verify the inequality (4.9).

In five-phase inverters, the space vector  $\bar{m}_3$  can be used to increase the linear modulation range of the space vector  $\bar{m}_1$ . As already stated, this gives rise to a new zone, not available in three-phase systems, called extended linear modulation region.

This region, in  $\alpha_1 - \beta_1$  plane, is located between the linear modulation region and the overmodulation region. In this region, the vector  $\bar{m}_1$  can follow the reference if an appropriate space vector  $\bar{m}_3$  is used to satisfy (4.15).

In general, for a given value of  $\bar{m}_{1,\text{ref}}$  several values of  $\bar{m}_{3,\text{ref}}$  satisfy (4.15). In the following, the solution with the lowest magnitude of  $\bar{m}_3$  is selected. Consequently, the voltage distortion, which is related to  $|\bar{m}_3|$ , is minimized.

The following two complex constant are introduced:

$$\begin{aligned}\bar{A}_{1,H,L} &= \bar{\alpha}_5^{(H-1)} - \bar{\alpha}_5^{(L-1)} \\ \bar{A}_{3,H,L} &= \bar{\alpha}_5^{3(H-1)} - \bar{\alpha}_5^{3(L-1)}\end{aligned}\quad (4.16)$$

Taking (4.16) into account, (4.15) can be rewritten as:

$$\bar{m}_3 \cdot \bar{A}_{3,H,L} \leq 1 - \bar{m}_1 \cdot \bar{A}_{1,H,L} \quad (4.17)$$

The modulating signal space vector  $\bar{m}_3$  can be decomposed along two orthogonal directions, respectively parallel and orthogonal to the complex constant  $\bar{A}_{3,H,L}$ , as shown in (4.18).

$$\bar{m}_3 = \bar{A}_{3,H,L}(\lambda + j\mu) \quad (4.18)$$

where  $\lambda$  and  $\mu$  are the degrees of freedom of  $\bar{m}_3$ . The magnitude of  $\bar{m}_3$  can be expressed as follows:

$$|\bar{m}_3| = |\bar{A}_{3,H,L}| \sqrt{(\lambda^2 + \mu^2)} \quad (4.19)$$

Substituting (4.18) in (4.17) leads to

$$\bar{A}_{3,H,L}(\lambda + j\mu) \cdot \bar{A}_{3,H,L} \leq 1 - \bar{m}_1 \cdot \bar{A}_{1,H,L} \quad (4.20)$$

From (4.20), it is possible to get the admissible value of  $\lambda$ :

$$\lambda \leq \frac{1 - \bar{m}_1 \cdot \bar{A}_{1,H,L}}{|\bar{A}_{3,H,L}|^2} \quad (4.21)$$

According to (4.17), the numerator of (4.21) is negative outside the linear modulation region, while the denominator is indeed positive. Therefore, the value of  $\lambda$  that minimizes the amplitude of  $\bar{m}_3$  in (4.18) is the upper bound of (4.21):

$$\lambda = \frac{1 - \bar{m}_1 \cdot \bar{A}_{1,H,L}}{|\bar{A}_{3,H,L}|^2} \quad (4.22)$$

To determine the value of  $\mu$ , it is necessary to verify that the selected  $\bar{m}_3$  does not change the order of the modulating signals assumed in (4.10), namely H is the index of the highest modulating signal, and L is the index of the lowest modulating signal. In practice, it is sufficient to verify that  $m_H$  is higher than the neighbouring value  $m_U$ , and  $m_L$  is lower than the neighbouring value  $m_D$ :

$$\begin{cases} m_H \geq m_U \\ m_L \leq m_D \end{cases} \quad (4.23)$$

Taking into account the inverse Clarke transformation, (4.23) can be rewritten as:

$$\begin{cases} \bar{m}_{1,ref} \cdot \bar{\alpha}_5^{(H-1)} + \bar{m}_{3,ref} \cdot \bar{\alpha}_5^{3(H-1)} \geq \bar{m}_{1,ref} \cdot \bar{\alpha}_5^{(U-1)} + \bar{m}_{3,ref} \cdot \bar{\alpha}_5^{3(U-1)} \\ \bar{m}_{1,ref} \cdot \bar{\alpha}_5^{(L-1)} + \bar{m}_{3,ref} \cdot \bar{\alpha}_5^{3(L-1)} \leq \bar{m}_{1,ref} \cdot \bar{\alpha}_5^{(D-1)} + \bar{m}_{3,ref} \cdot \bar{\alpha}_5^{3(D-1)} \end{cases} \quad (4.24)$$

For convenience, the following auxiliary constants are introduced:

$$\begin{aligned} \bar{A}_{1,H,U} &= \bar{\alpha}_5^{(H-1)} - \bar{\alpha}_5^{(U-1)} \\ \bar{A}_{3,H,U} &= \bar{\alpha}_5^{3(H-1)} - \bar{\alpha}_5^{3(U-1)} \\ \bar{A}_{1,L,D} &= \bar{\alpha}_5^{(L-1)} - \bar{\alpha}_5^{(D-1)} \\ \bar{A}_{3,L,D} &= \bar{\alpha}_5^{3(L-1)} - \bar{\alpha}_5^{3(D-1)} \end{aligned} \quad (4.25)$$

Substituting (4.18) and (4.25) in (4.24) leads to the subsequent inequalities:

$$\begin{cases} \bar{A}_{3,H,L}(\lambda + j\mu) \cdot \bar{A}_{3,H,U} \geq -\bar{m}_{1,ref} \cdot \bar{A}_{1,H,U} \\ \bar{A}_{3,H,L}(\lambda + j\mu) \cdot \bar{A}_{3,L,D} \leq -\bar{m}_{1,ref} \cdot \bar{A}_{1,L,D} \end{cases} \quad (4.26)$$

By isolating the variable  $\mu$ , (4.26) can be rewritten as:

$$\begin{cases} \mu(j\bar{A}_{3,H,L} \cdot \bar{A}_{3,H,U}) \geq -\bar{m}_{1,ref} \cdot \bar{A}_{1,H,U} - \lambda(\bar{A}_{3,H,L} \cdot \bar{A}_{3,H,U}) \\ \mu(j\bar{A}_{3,H,L} \cdot \bar{A}_{3,L,D}) \leq -\bar{m}_{1,ref} \cdot \bar{A}_{1,L,D} - \lambda(\bar{A}_{3,H,L} \cdot \bar{A}_{3,L,D}) \end{cases} \quad (4.27)$$

The system of linear inequalities (4.27) identifies a range of values for  $\mu$ . Let  $\mu_{max}$  and  $\mu_{min}$  be respectively the upper and lower ends, which means:

$$\mu_{min} \leq \mu \leq \mu_{max} \quad (4.28)$$

If  $\mu_{max}$  is positive and  $\mu_{min}$  is negative, choosing  $\mu$  equal to zero minimizes the magnitude of  $\bar{m}_3$ . Conversely, if  $\mu_{max}$  and  $\mu_{min}$  are both positive (or negative),  $\mu$  must be chosen equal to the lowest absolute value between them.

When  $\bar{m}_1$  is on the boundary of the extended linear region, the interval  $[\mu_{min}, \mu_{max}]$  collapses into a single point, and the solution of (4.17) is unique. This operating condition is remarkable as it corresponds to the situation in which the two highest modulating signals  $m_H$  and  $m_U$  are both equal to 1, and the two lowest modulating signals  $m_L$  and  $m_D$  are zero [31]:

$$\begin{cases} m_H = m_U \\ m_L = m_D \end{cases} \quad (4.29)$$

Taking the inverse Clarke transformation into account, according to (4.26), (4.29) can be rewritten as:

$$\begin{cases} \bar{m}_{3,ref} \cdot \bar{A}_{3,H,U} = -\bar{m}_{1,ref} \cdot \bar{A}_{1,H,U} \\ \bar{m}_{3,ref} \cdot \bar{A}_{3,L,D} = -\bar{m}_{1,ref} \cdot \bar{A}_{1,L,D} \end{cases} \quad (4.30)$$

In order to simplify the resolution of the system (4.30), it is convenient to decompose the vector  $\bar{m}_{3,ref}$  on two components that are respectively orthogonal to  $\bar{A}_{3,H,U}$  and  $\bar{A}_{3,L,D}$ , as expressed in (4.31):

$$\bar{m}_{3,ref} = C_1 j\bar{A}_{3,H,U} + C_2 j\bar{A}_{3,L,D} \quad (4.31)$$

By introducing (4.31) into (4.30), it is possible to obtain the value of the two coefficients  $C_1$  and  $C_2$  and, subsequently, the expression of  $\bar{m}_{3,ref}$  that allows  $\bar{m}_{1,ref}$  to reach its maximum magnitude.

$$\begin{cases} C_1 j\bar{A}_{3,H,U} \cdot \bar{A}_{3,H,U} + C_2 j\bar{A}_{3,L,D} \cdot \bar{A}_{3,H,U} = -\bar{m}_{1,ref} \cdot \bar{A}_{1,H,U} \\ C_1 j\bar{A}_{3,H,U} \cdot \bar{A}_{3,L,D} + C_2 j\bar{A}_{3,L,D} \cdot \bar{A}_{3,L,D} = -\bar{m}_{1,ref} \cdot \bar{A}_{1,L,D} \end{cases} \quad (4.32)$$

Owing to the properties of the scalar product, from (4.32) it is possible to achieve the following relationships:

$$\begin{cases} C_2 = \frac{\bar{m}_{1,ref} \cdot \bar{A}_{1,H,U}}{j\bar{A}_{3,H,U} \cdot \bar{A}_{3,L,D}} \\ C_1 = \frac{-\bar{m}_{1,ref} \cdot \bar{A}_{1,L,D}}{j\bar{A}_{3,H,U} \cdot \bar{A}_{3,L,D}} \end{cases} \quad (4.33)$$

By substituting (4.33) in (4.31) leads to:

$$\bar{m}_{3,ref} = j \frac{(\bar{m}_{1,ref} \cdot \bar{A}_{1,H,U})\bar{A}_{3,L,D} - (\bar{m}_{1,ref} \cdot \bar{A}_{1,L,D})\bar{A}_{3,H,U}}{j\bar{A}_{3,H,U} \cdot \bar{A}_{3,L,D}} \quad (4.34)$$

The maximum magnitude of the space vector  $\bar{m}_1$  for each possible argument, obtainable when the space vector  $\bar{m}_3$  is used to extend the range of modulation, can be determined by (4.11) and rewritten as:

$$\bar{m}_1 \cdot \bar{A}_{1,H,L} + \bar{m}_3 \cdot \bar{A}_{3,H,L} \leq 1 \quad (4.35)$$

The (4.35) must be valid in each region of the  $\alpha - \beta$  plane.

Processing the second term of the first member of (4.34) and introducing (4.17) leads to:

$$\frac{(\bar{m}_1 \cdot \bar{A}_{1,H,U})j\bar{A}_{3,L,D} - (\bar{m}_1 \cdot \bar{A}_{1,L,D})j\bar{A}_{3,H,U}}{j\bar{A}_{3,H,U} \cdot \bar{A}_{3,L,D}} \cdot \bar{A}_{3,H,L} \quad (4.36)$$

The (4.36) can be simplified by introducing two constant quantities  $C_1$  and  $C_2$  defined as:

$$C_1 = \frac{j\bar{A}_{3,L,D} \cdot \bar{A}_{3,H,L}}{j\bar{A}_{3,H,U} \cdot \bar{A}_{3,L,D}} \quad (4.37)$$

$$C_2 = -\frac{j\bar{A}_{3,H,U} \cdot \bar{A}_{3,H,L}}{j\bar{A}_{3,H,U} \cdot \bar{A}_{3,L,D}}$$

By introducing (4.34) and (4.37) into (4.15), it is possible to write:

$$\bar{m}_1 \cdot (\bar{A}_{1,HL} + C_1\bar{A}_{1,H,U} + C_2\bar{A}_{1,L,D}) = 1 \quad (4.38)$$

The order of the modulating signals in each sector has been defined by (4.10) and, since  $\bar{m}_3$  does not change the order, the following constraints occur:

$$\bar{A}_{1,H,U} \cdot j\bar{A}_{1,HL} = \bar{A}_{1,L,D} \cdot j\bar{A}_{1,HL} \quad (4.39)$$

$$\bar{A}_{3,L,D} \cdot j\bar{A}_{3,H,L} = \bar{A}_{3,H,U} \cdot j\bar{A}_{3,H,L} \quad (4.40)$$

With this constraints it is possible to write:

$$(C_1\bar{A}_{1,H,U} + C_2\bar{A}_{1,L,D}) \cdot j\bar{A}_{1,HL} = 0 \quad (4.41)$$

From (4.41) it is trivial to verify that:

$$C_1 = -C_2 \quad (4.42)$$

So, with this considerations, the (4.38) can be rewritten as:

$$(1 + K)\bar{m}_1 \cdot \bar{A}_{1,HL} = 1 \quad (4.43)$$

Equation (4.43) is analogous to (4.15) therefore, as done for (4.15), it is possible to show that it represents a regular decagon that is shown in Fig. 4.3.

The distance between the center and the vertex of the decagon, which represents the maximum modulation index  $|\bar{m}_1|$ , is evaluated as:

$$|\bar{m}_1| = \frac{2}{5} \left[ 1 + 2 \cos \left( \frac{2\pi}{5} \right) \right] \quad (4.44)$$

To obtain the radius  $r_2$  of the circle inscribed in the decagon, it is sufficient to multiply (4.44) for  $\cos \left( \frac{\pi}{10} \right)$  in order to obtain the apothem, that is

$$r_2 = \frac{2}{5} \left[ 1 + 2 \cos \left( \frac{2\pi}{5} \right) \right] \cos \left( \frac{\pi}{10} \right) \quad (4.45)$$

The region between the two regular decagons shown in Fig. 4.3 is called “extended linear modulation region”. When the space vector  $\bar{m}_1$  moves out of the outer decagon, the inverter operates in the extended overmodulation region.

In Fig. 4.3 all the available modulation regions for five-phase inverter and the relative radius are reported.

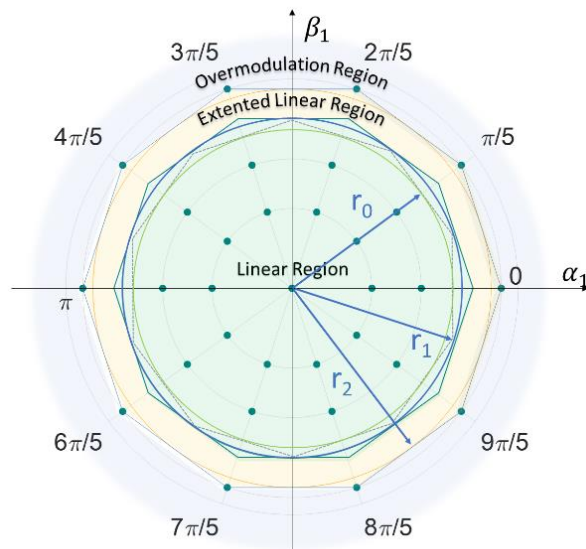


Fig.4.3 Modulation regions in a five-phase inverter.

## 4.4 Overmodulation Region

The last region left to be analysed is the overmodulation region. In overmodulation conditions, the generated vectors  $\bar{m}_1$  and  $\bar{m}_3$  are different from the reference vectors  $\bar{m}_{1,ref}$  and  $\bar{m}_{3,ref}$ . In particular,  $\bar{m}_1$  cannot cover a circular path at steady state. Since  $\bar{m}_1$  controls the current vector in the fundamental subspace, which is in turn related to the magnetic field in the air gap, a certain level of torque ripple is unavoidable. In these operating conditions, the voltage reference  $\bar{m}_{3,ref}$  is equal to (4.34), as this value allows maximizing the amplitude of  $\bar{m}_{1,ref}$ .

In the overmodulation region many different techniques are available. The generalizations to five-phase inverters of the Minimum Phase Error (MPE), the Minimum Distance (MD), and Bolognani's modulation (Bs), [32], [57], [58] generally used for three-phase inverters, are presented hereafter.

### 4.4.1 Minimum Phase Error

The MPE overmodulation method, shown in Fig. 4.4, divides the modulating signal  $m_{k,ref}$  of each inverter leg by a normalization factor, which does not affect either the phase angles of the space vectors  $\bar{v}_1$  and  $\bar{v}_3$  or the ratio of their magnitudes, but only the respective amplitudes, so that the modulating signals fit the interval  $[0,1]$ . The modified modulating signals are obtained according to the following relationships:

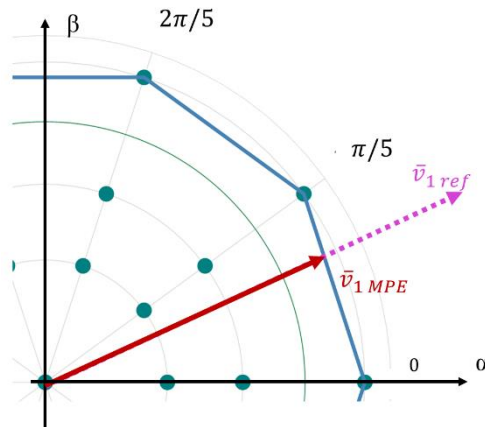


Fig. 4.4. Generation of the output voltage vector starting from the reference voltage  $\bar{v}_{1,ref}$  according to the minimum phase error strategy ( $\bar{v}_{1,MPE}$ ).

$$m_k = \frac{m_{k,ref} - m_{L,ref}}{m_{H,ref} - m_{L,ref}} \text{ for } k = 1, \dots, 5 \quad (4.46)$$

where the index H and L are the same defined in (4.10).

It can be verified that this solution leads to a reduction of the harmonic distortion of the phase currents compared to the other considered techniques.

The maximum modulation index, defined as the ratio of the magnitude of the voltage  $\bar{v}_1$  and the dc-link voltage  $E_{DC}$  (4.47) can be evaluated with the Fourier series decomposition.

$$MI = \frac{|\bar{v}_1|}{E_{DC}} \quad (4.47)$$

To obtain the maximum value of MI it is sufficient to analysed the first harmonic of the output phase voltage. For the symmetry of the system it is convenient to explore the voltage of the first phase in the range  $\left[0, \frac{\pi}{2}\right]$ .

The phase one voltage, obtained using only the voltage space vector one, in the range  $\left[0, \frac{3\pi}{10}\right]$  is represented by the following expression:

$$V_1 = \begin{cases} \max\{|\bar{m}_1|\} \left\{ \left[ \cos\left(\frac{\pi}{5}\right) - 1 \right] \frac{5\theta}{\pi} + 1 \right\} & 0 \leq \theta \leq \frac{\pi}{5} \\ \max\{|\bar{m}_1|\} \left\{ \left[ \cos\left(\frac{2\pi}{5}\right) - \cos\left(\frac{\pi}{5}\right) \right] \left( \theta - \frac{\pi}{5} \right) \frac{5}{\pi} + \cos\left(\frac{\pi}{5}\right) \right\} & \frac{\pi}{5} \leq \theta \leq \frac{2\pi}{5} \\ \max\{|\bar{m}_1|\} \left\{ \left[ \cos\left(\frac{3\pi}{5}\right) - \cos\left(\frac{2\pi}{5}\right) \right] \left( \theta - \frac{2\pi}{5} \right) \frac{5}{\pi} + \cos\left(\frac{2\pi}{5}\right) \right\} & \frac{2\pi}{5} \leq \theta \leq \frac{3\pi}{5} \end{cases} \quad (4.48)$$

where the value of  $\max\{|\bar{m}_1|\}$  is expressed by (4.44).

The first harmonic of the voltage Fourier series decomposition in the interval  $\left[0, \frac{\pi}{2}\right]$  allows obtaining the maximum value of the minimum phase error strategy as:

$$MI_{MPE \max} = \frac{5(\sqrt{5} - 1)}{\pi^2} \approx 0.626 \quad (4.49)$$

As with three-phase inverters, the multi-phase MPE technique does not lead to a pure square wave operation even at a very high modulation index.

#### 4.4.2 Minimum Distance

The Minimum Distance overmodulation technique, shown in Fig. 4.5, minimizes the error (distance) between the requested voltage vector and the voltage vector generated by the inverter (in the fundamental subspace). Remarkably, the modulating signals can be calculated easily even for a five-phase inverter. Initially, it is necessary to calculate the zero-sequence component  $m_0$  of the desired voltage vector with the following expression:

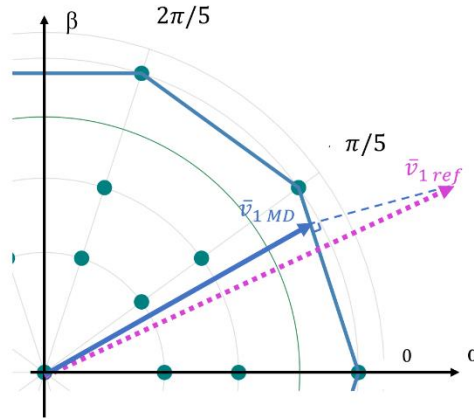


Fig.4.5. Generation of the output voltage vector starting from the reference voltage  $\bar{v}_{1,ref}$  according to the minimum distance strategy ( $\bar{v}_{1,MD}$ ).

$$m_0 = \frac{1 - n_H - n_L}{2} \quad (4.50)$$

where the generic  $n_k$  is defined as:

$$n_k = \bar{m}_{1,ref} \cdot \bar{\alpha}_5^{(k-1)} + \bar{m}_{3,ref} \cdot \bar{\alpha}_5^{3(k-1)} \quad \text{for } k = 1, \dots, 5, \quad (4.51)$$

and  $\bar{m}_{3,ref}$  is given by (4.34).

Then, the  $k^{\text{th}}$  modulating signal is calculated as:

$$m_k = m_0 + n_k \quad (4.52)$$

and is clamped in the range  $[0,1]$ . In the overmodulation region, the two highest modulating signals are equal to 1, while the two lowest modulating signals are equal to 0.

It is possible to demonstrate that this procedure leads to the lowest magnitude error of  $\bar{v}_{1,ref}$ .

The modulating signal space vectors  $\bar{m}_{1,ref}$  and  $\bar{m}_1$  are defined as follows:

$$\bar{m}_1 = \frac{2}{5} (m_H \bar{\alpha}_H + m_U \bar{\alpha}_U + m_M \bar{\alpha}_M + m_D \bar{\alpha}_D + m_L \bar{\alpha}_L) \quad (4.53)$$

$$\bar{m}_{1,ref} = \frac{2}{5} (m_{H,ref} \bar{\alpha}_H + m_{U,ref} \bar{\alpha}_U + m_{M,ref} \bar{\alpha}_M + m_{D,ref} \bar{\alpha}_D + m_{L,ref} \bar{\alpha}_L) \quad (4.54)$$

In the overmodulation region,  $\bar{m}_{3,ref}$  is chosen according to (4.34). Consequently, (4.29) ensures that  $m_{H,ref}$  is equal to  $m_{U,ref}$ , and  $m_{L,ref}$  is equal to  $m_{D,ref}$ . Also,  $m_{H,ref}$  must be greater than

one, while  $m_{L,ref}$  must be lower than zero. Therefore,  $m_H$  and  $m_U$  are clamped to 1, while  $m_D$  and  $m_L$  are clamped to 0. The only modulating signal in the range  $[0,1]$  is  $m_{M,ref}$ , which coincides with  $m_M$ . Then, (4.53) and (4.54) can be rewritten as follows:

$$\bar{m}_1 = \frac{2}{5} (m_H \bar{\alpha}_5^H + m_U \bar{\alpha}_5^U + m_M \bar{\alpha}_5^M) \quad (4.55)$$

$$\bar{m}_{1,ref} = \frac{2}{5} (m_{H,ref} \bar{\alpha}_5^H + m_{H,ref} \bar{\alpha}_5^U + m_{M,ref} \bar{\alpha}_5^M + m_{L,ref} \bar{\alpha}_5^D + m_{L,ref} \bar{\alpha}_5^L) \quad (4.56)$$

The voltage error is

$$\overline{\Delta m}_1 = \bar{m}_{1,ref} - \bar{m}_1 = \frac{2}{5} [(m_{H,ref} - 1)(\bar{\alpha}_5^H + \bar{\alpha}_5^U) + m_{L,ref}(\bar{\alpha}_5^D + \bar{\alpha}_5^L)] \quad (4.57)$$

The voltage error is the smallest when  $\overline{\Delta m}_1$  is orthogonal to the boundary of the overmodulation region. This condition can be written as follows:

$$\overline{\Delta m}_1 \cdot (\bar{\alpha}_5^H + \bar{\alpha}_5^L) = 0 \quad (4.58)$$

where  $\bar{\alpha}_H + \bar{\alpha}_L$  is the direction of the side of the regular decagon.

Since it can be shown that:

$$(\bar{\alpha}_5^H + \bar{\alpha}_5^U) \cdot (\bar{\alpha}_5^H + \bar{\alpha}_5^L) = (\bar{\alpha}_5^D + \bar{\alpha}_5^L) \cdot (\bar{\alpha}_5^H + \bar{\alpha}_5^L) \quad (4.59)$$

(4.58) becomes:

$$(m_{H,ref} + m_{L,ref} - 1)(\bar{\alpha}_5^H + \bar{\alpha}_5^U) \cdot (\bar{\alpha}_5^H + \bar{\alpha}_5^L) = 0 \quad (4.60)$$

Replacing (4.52) in (4.60) leads to the expression (4.50) of the zero-sequence component.

Eq. (4.59) can be rewritten as:

$$(\bar{\alpha}_5^U - \bar{\alpha}_5^D) \cdot (\bar{\alpha}_5^H + \bar{\alpha}_5^L) = 0 \quad (4.61)$$

where:

$$(\bar{\alpha}_5^U - \bar{\alpha}_5^D) = 2j \sin\left(\pi \frac{U-D}{5}\right) e^{j\frac{\pi}{5}(U+D-2)} \quad (4.62)$$

$$(\bar{\alpha}_5^H - \bar{\alpha}_5^L) = 2 \cos\left(\pi \frac{H-L}{5}\right) e^{j\frac{\pi}{5}(H+L-2)} \quad (4.63)$$

With the usual values of  $\bar{m}_3$ , the ordering of the modulating signals is so that  $H + L - U - D = 5n$ , with  $n \in [-1, 0, 1]$ . With this consideration, the exponent of (4.62) and (4.63) is the same and this guarantees that  $(\bar{\alpha}_5^U - \bar{\alpha}_5^D)$  is perpendicular to  $(\bar{\alpha}_5^H - \bar{\alpha}_5^L)$ . This proves that the error  $\bar{\Delta m}_1$  is the lowest.

Observing Fig. 4.5, it is evident that the technique of Minimum Distance, for high magnitude values of  $\bar{v}_{1,ref}$ , tends to the square wave.

So that, it is trivial to demonstrate that the maximum modulation index for the Minimum Distance, obtained when  $|\bar{v}_{1,ref}|$  tends to be infinite, becomes:

$$MI_{MD\ max} = \frac{2}{\pi} \approx 0.637 \quad (4.64)$$

#### 4.4.3 Bolognani's Modulation

Bolognani's modulation was introduced for the first time for three-phase systems in [58]. In its multi-phase counterpart, the output voltage vector in the overmodulation region is the one with the lowest phase error among the admissible vectors with the lowest magnitude error. In practice, whenever the requested voltage exceeds the extended linear region, represented by the decagon shown in Fig. 4.6, the output voltage is kept equal to the value that it has in the crossing point. If the requested voltage increases further, the inverter quickly tends to the square-wave operation that uses only the ten vectors placed on the vertices of the decagon. Among all the presented techniques, this is the only one that allows obtaining a square wave operation with a finite modulation index ( $MI_{ref} = 0.647$ ). In this case, it can be demonstrated that the value of the maximum modulation index is:

$$MI_{Bs\ max} = \frac{2}{\pi} \approx 0.637 \quad (4.65)$$

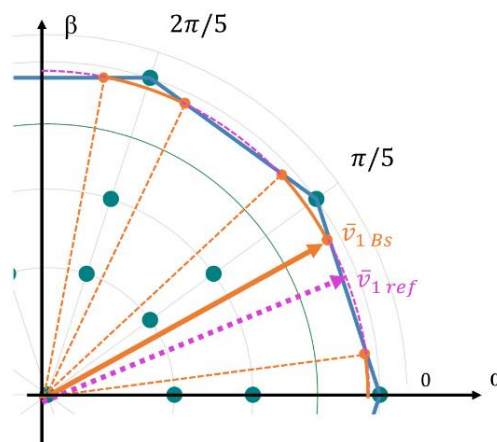


Fig. 4.6. Generation of the output voltage vector starting from the reference voltage  $\bar{v}_{1,ref}$  according to the multi-phase Bolognani's overmodulation ( $\bar{v}_{1,Bs}$ ).

In Fig. 4.7, MD, MDE, and Bs overmodulation strategies are compared with each other and with the traditional space vector pulse width modulation (SVPWM). Although SVPWM can be implemented as an SVM strategy, namely the one that uses two zero vectors, equally allocated in the middle and at the end of the switching pattern, it is considered as a carrier based centre-aligned pulse width modulation technique, whose zero-sequence component is given by (4.50) with  $\bar{v}_{3,ref}$  equal to zero [59]. If some of the resulting duty-cycles are outside the range [0,1], they are clipped to the interval edges.

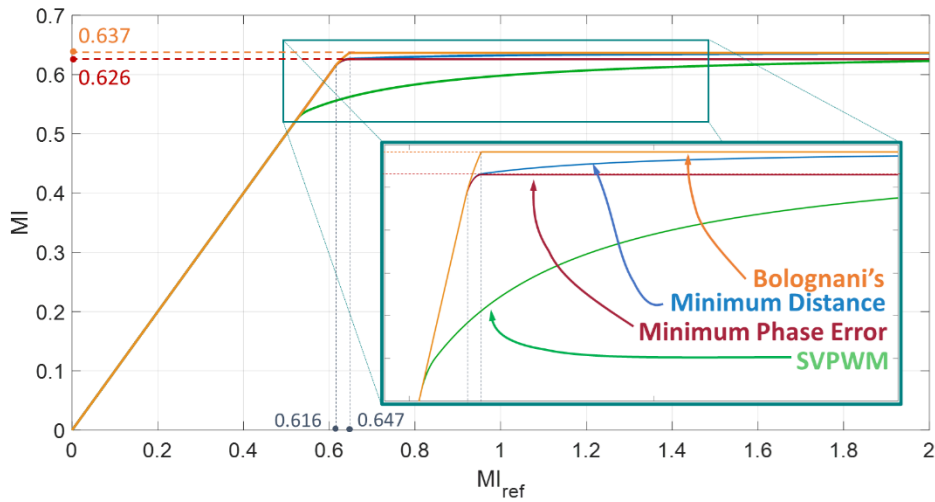


Fig. 4.7. Requested modulation index  $MI_{ref}$  versus actual modulation index  $MI$ .

In the graph of Fig. 4.7, the desired modulation index  $MI_{ref}$  is shown on the horizontal axis, while the actual modulation index  $MI$  is shown on the vertical axis. When the modulation index exceeds  $r_1$  (0.526), the SVPWM technique maintains  $\bar{v}_3$  equal to zero, thus causing a nonlinear relationship between  $\bar{v}_{1,ref}$  and the actual voltage  $\bar{v}_1$ . Conversely, by choosing a suitable value of the vector  $\bar{v}_3$ , it is possible to keep  $\bar{v}_1$  equal to the desired one,  $\bar{v}_{1,ref}$  in the extended linear region. When  $MI_{ref}$  exceeds  $r_2$  (0.616), the MD, MPE, and Bs overmodulation strategies have slightly different behaviours. While Bs strategy quickly converges to a square-wave operation, the convergence rate of MD strategy is slower. In contrast, the MPE strategy never reaches the pure square-wave operation and the maximum modulation index is slightly lower. The SVPWM strategy has the same performance as the MPE strategy but only for very high values of the modulation index (above 2.5). In conclusion, the highest voltage cannot be used as an indicator to compare the performance of the overmodulation algorithms with one another. Conversely, the linearity error of the modulation process, i.e., the difference between the desired voltage and the actual voltage, and the voltage quality appear to be particularly relevant because they can significantly affect the transient and steady-state response of an electric drive.

## 4.5 Experimental Result

In order to verify the capability of the proposed modulation strategy to extend the linear modulation region and analyse the behaviour of the overmodulation strategies for a five-phase inverters described above, an experimental setup has been prepared in the LEMAD laboratory of Bologna.

A five-phase wound-rotor induction motor and a five-phase IGBT inverter have been used for the tests. A picture of the experimental setup is shown in Fig. 4.8.

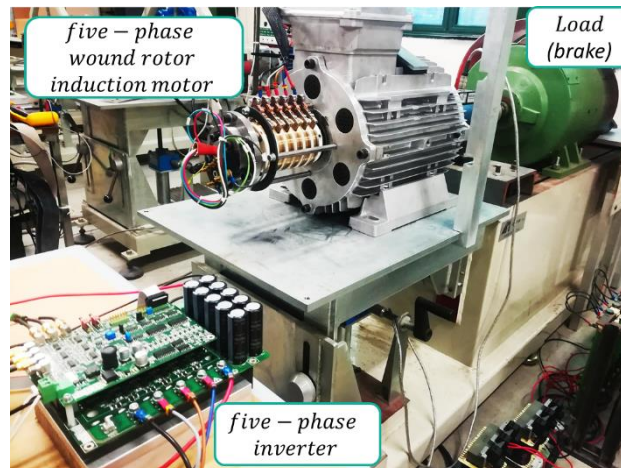


Fig. 4.8. Experimental setup of the electric drive composed by a five-phase wound-rotor induction machine and a five-phase inverter.

The motor is a 30-slots five-phase induction machine with three pairs of poles and distributed windings.

The parameters of the machine, experimentally determined, are listed in Table 4.1, whereas those of the inverter are shown in Table 4.2.

|                  |         |          |         |
|------------------|---------|----------|---------|
| Rated Speed      | 150 Rpm | $R_{R1}$ | 4.8 Ohm |
| $R_S$            | 1.7 Ohm | $R_{R3}$ | 4.8 Ohm |
| $L_{S1}$         | 411 mH  | $L_{R1}$ | 939 mH  |
| $L_{S3}$         | 68 mH   | $L_{R3}$ | 158 mH  |
| $M_1$            | 555 mH  | $M_3$    | 53 mH   |
| Pole pair number | 3       |          |         |

Tab. 4.1 Parameters of the five-phase wound-rotor induction machine.

|                     |              |
|---------------------|--------------|
| $I_{MAX\_IGBT}$     | 10 A         |
| $E_{DC}$            | 100 V        |
| Switching frequency | 5 kHz        |
| Dead Time           | 1.6 $\mu$ s  |
| DC-link capacitance | 1100 $\mu$ F |

Tab. 4.2 Parameters of the five-phase inverter.

The tests at steady state, such as the measurements of the voltage loci and current THD, have been carried out by using the inverter as a voltage source with an open-loop control. Conversely, a conventional rotor flux-oriented control scheme for induction motors has been used in the transient tests. The corresponding block diagram is shown in Fig. 4.9.

The PI controller (a), as shown in Fig. 4.9, adjusts the reference value for the torque-producing component of the stator current, depending on the actual speed error. The two PI controllers (b) and (c), track the current references of the components of the stator current in the  $d_1 - q_1$  reference frame, whose d-axis is aligned with the rotor flux vector. The reference stator voltage is obtained by combining the output signals of the previous controllers, compensated for the  $d_1 - q_1$  back-emfs, and expressing the resulting vector in the stationary reference frame  $\alpha_1 - \beta_1$ . The rotor flux in the fundamental subspace is estimated by means of a flux observer that integrates the rotor equation, while an incremental encoder measures the mechanical speed.

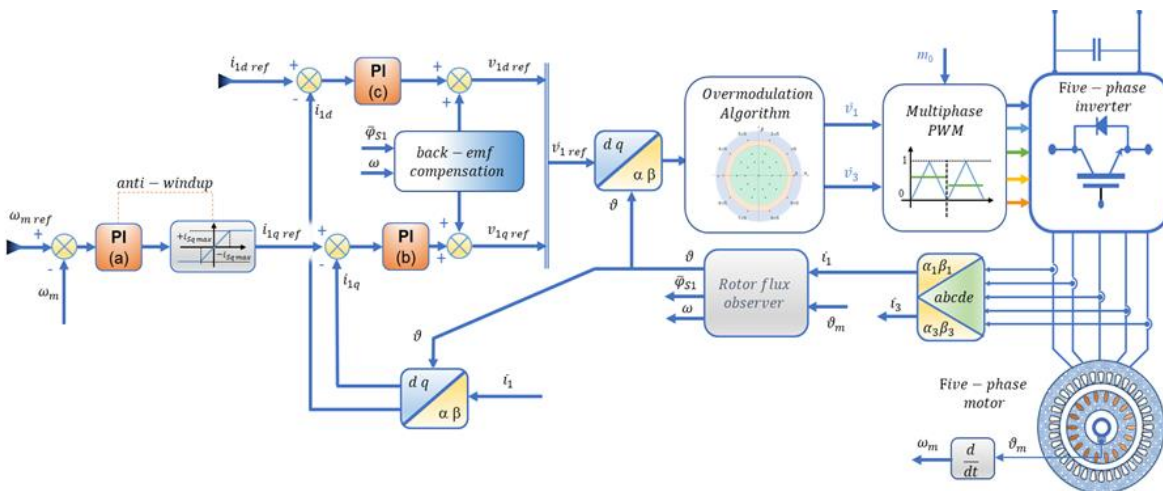


Fig. 4.9. Block diagram of the rotor field-oriented control scheme for the five-phase induction motor drive used in the experimental tests.

As can be seen, the current vector  $\bar{i}_3$  is not directly controlled and is free to change, its behaviour is indirectly affected by the over-modulation algorithm. Conversely, one could suspect that the current regulators might alter the trajectory of  $\bar{i}_1$ , since the bandwidth of the current controllers is greater than the frequency of the most significant overmodulation voltage harmonics (3, 7, 9, 11) at

the rated speed. However, since the inverter already operates in overmodulation, this compensation action is neither possible nor significant.

The first tests carried out are in steady state conditions to verify the possibility to work properly in the extended linear modulation region.

The range of extended linear modulation ( $0.523 < MI < 0.616$ ) has been divided into six parts and, for each of them, it has been done a test to obtain the loci of  $\bar{m}_1$  and  $\bar{m}_3$  and the waveforms of the real and imaginary parts of the space vector  $\bar{v}_{3,ref}$ . The results of the tests are reported in Fig. 4.10.

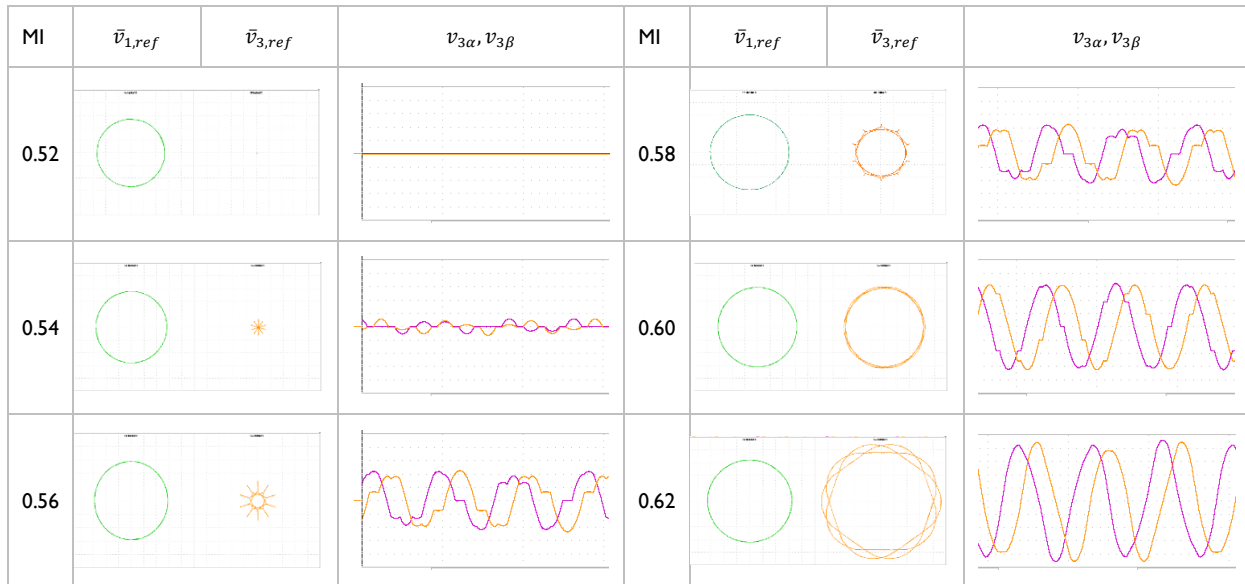


Fig. 4.10 Loci of space vector  $\bar{v}_{1,ref}$  (20 V/div) and  $\bar{v}_{3,ref}$  (4 V/div) in extended linear modulation region for different modulation indexes (50 ms/div).

As can be seen, the space vector related to the first harmonic of the magnetic field  $\bar{m}_1$  tracks a circular orbit, whereas the path of  $\bar{m}_3$  is more complicated and strongly dependent on the value of the modulation index MI, and its magnitude increases as the MI.

After that, a variable speed test, which passes through all the available modulation regions, has been carried out to evaluate the effect of the voltage injections on the phase currents of the machine. The results are shown in Figs. 4.11 and 4.12.

If the motor speed is less than about 100 rpm, the inverter operates in the linear region. Beyond this speed, the use of the space vector  $\bar{v}_{3,ref}$  allows operating in the extended linear modulation. As soon as the inverter enters into the extended linear modulation before, and in overmodulation region after, some modulating signals are forced to zero or to one for long periods, which causes a drastic reduction in the number of inverter commutations that is visible in the waveform of the pole voltages of the inverter. Consequently, when the converter operates in the extended linear modulation region, there is a significant reduction in the switching losses. The drawback is the presence of a distorted phase current, which gets worse as the modulation index rises.

The distortion of the phase current is analysed in Fig. 4.13, where, in a single image, the spectra of the phase current as a function of the modulation index for different modulation strategies are summarized.

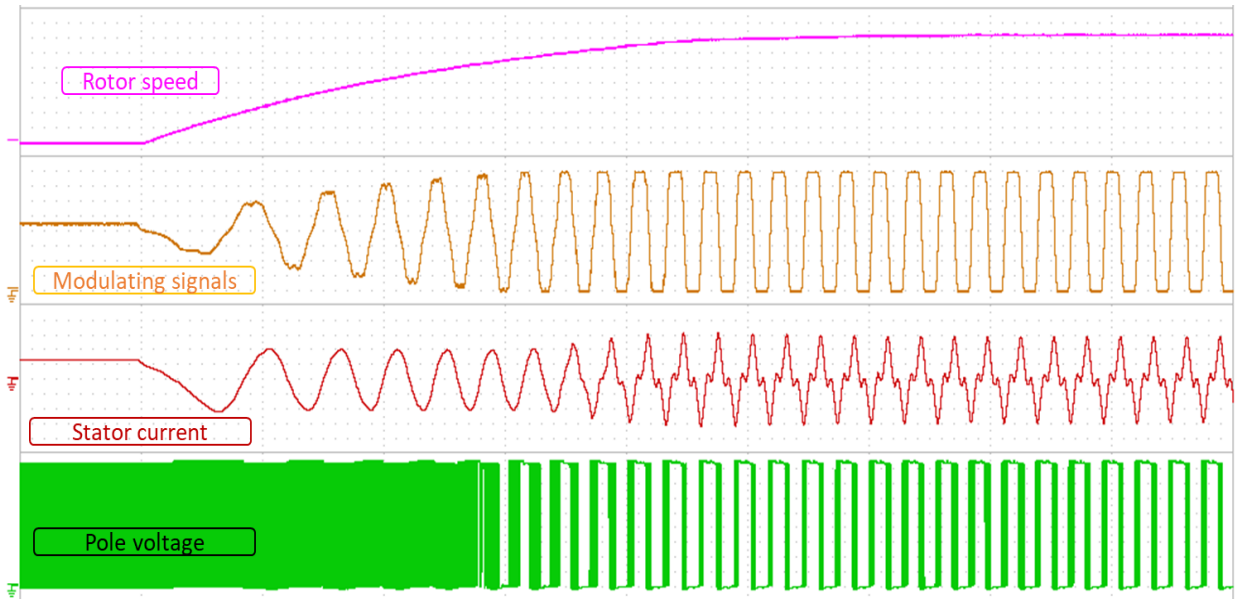


Fig. 4.11. Speed transient of the motor from 0 to 144 rpm. Mechanical speed  $\omega_m$  (20 rpm/div), modulating signal of phase 1 (0.125/div), current of phase 1 (2 A/div), and pole voltage  $v_{p1}$  of phase 1 (12 V/div).

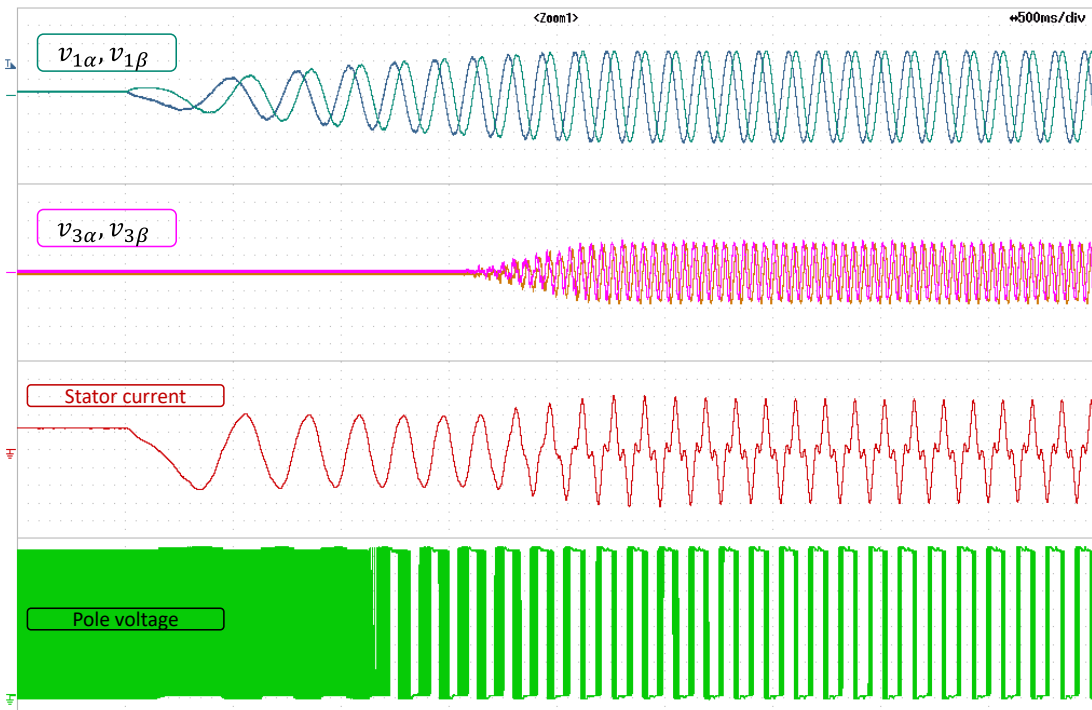


Fig. 4.12. Speed transient of the motor from 0 to 144 rpm. Waveforms of real and imaginary part of  $\bar{v}_{1,ref}$  (25 V/div) and  $\bar{v}_{3,ref}$  (10 V/div), current of phase 1 (2 A/div), and pole voltage  $v_{p1}$  of phase 1 (12 V/div).

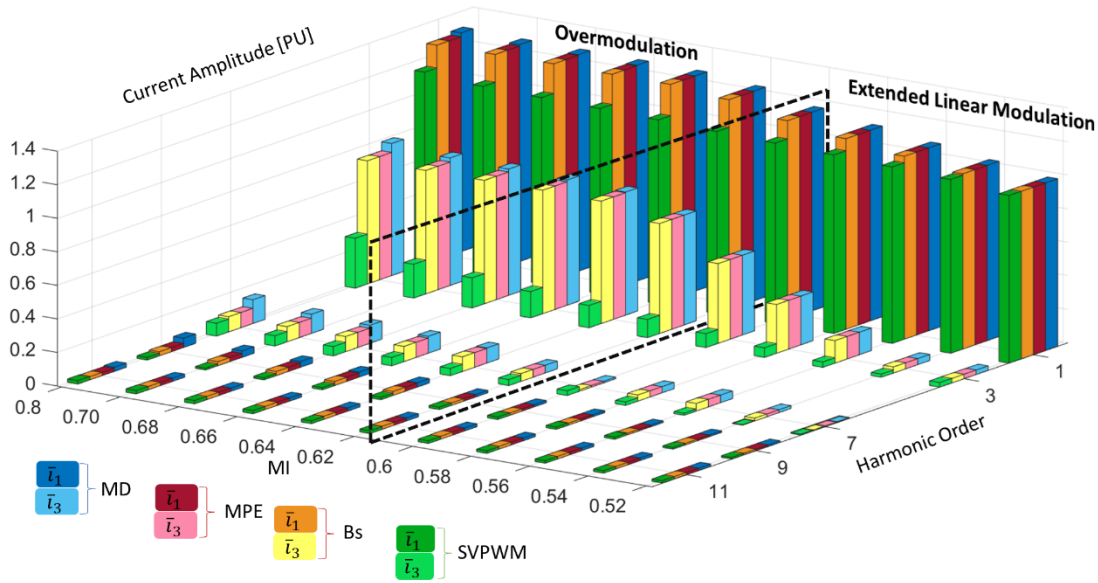


Fig. 4.13. Spectra of the phase current for different modulation indexes and different strategies.

The amplitude of the phase current is normalized by the current present at the boundary of the linear region. The harmonics produced by the space vector  $\bar{v}_1$  and those produced by  $\bar{v}_3$  have been plotted with different colours [60]. In the extended linear modulation region, the MD, MPE, and Bs techniques are equal, and the first harmonic increases linearly as a function of the modulation index. On the contrary, the fundamental harmonic of SVPWM is not a linear function of the modulation index, as already shown in Fig. 4.7. However, the use of vector  $\bar{v}_3$  generates the presence of the third and seventh harmonic components in the currents. Consequently, the total harmonic distortion (THD) of the stator current increases significantly. The extent of this distortion is strongly dependent on the electrical parameters of the machine.

The total harmonic distortion (THD) of the stator current detected during the tests, for all the overmodulation techniques previously mentioned, at different modulation index MI, is reported in Fig. 4.14.

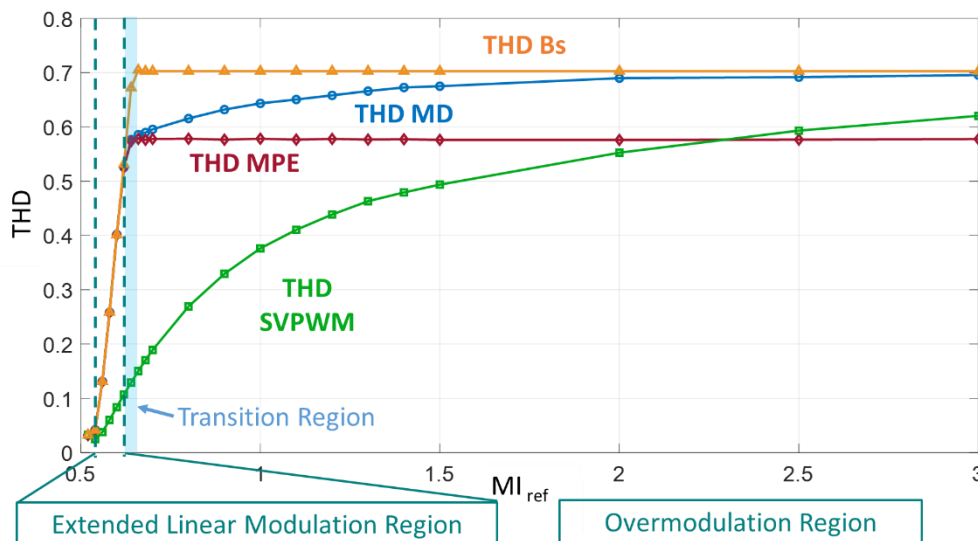


Fig. 4.14. THD of the stator current for different modulation regions as a function of the modulation index for all the overmodulation techniques under study.

Fig. 4.14 shows how the SVPWM modulation tends to resemble the MD technique for modulation indexes greater than 2.5, while the MPE technique does not rise any more after reaching the saturation level.

Subsequently, as already done for the extended linear modulation, tests for tracking the loci of  $\bar{v}_1$  and  $\bar{v}_3$  with different overmodulation techniques have been carried out.

In Fig. 4.15, the loci of  $\bar{m}_{1,ref}$ ,  $\bar{m}_1$  and  $\bar{m}_{3,ref}$ ,  $\bar{m}_3$  for two different modulation strategies, the Minimum Distance (MD) and the Minimum Phase Error (MPE), with five different modulation indexes, are reported to analyse the behaviour in the range of the overmodulation region. The modulation indexes adopted for the tests are: 0.62-0.64-0.66-0.68-0.70. It is possible to exchange the MD and MPE technique because, in this test, the dynamics is not evaluated. The maximum modulation index for the two strategies differs slightly and is not appreciable in these tests.

It can be seen that, the two overmodulation strategies presented (MD and MPE) draw the same trajectories for  $\bar{m}_1$  and  $\bar{m}_3$  in the complex planes  $\alpha_1 - \beta_1$  and  $\alpha_3 - \beta_3$ , respectively. What differentiates the modulation techniques is the speed with which the path is covered. For all these techniques, the actual space vector  $\bar{m}_1$  is constrained within a regular decagon, reaching the maximum value 0.626, while the reference  $\bar{m}_{1,ref}$ , continues to follow a circular trajectory. The space vectors  $\bar{m}_3$  and  $\bar{m}_{3,ref}$  follow a path with the shape of a star polygon.

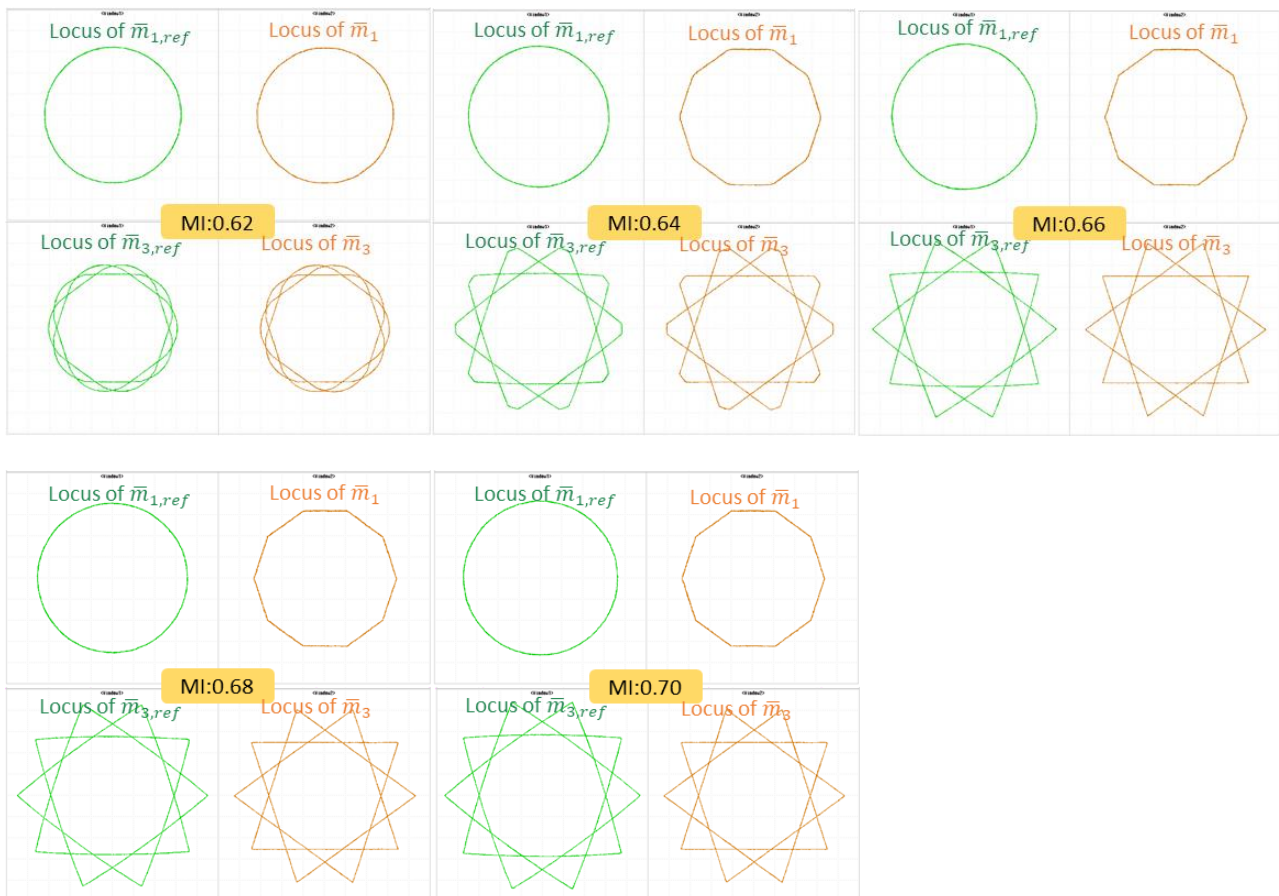


Fig. 4.15. Loci of  $\bar{m}_{1,ref}$  (20 V/div),  $\bar{m}_1$  (20 V/div),  $\bar{m}_{3,ref}$  (6 V/div),  $\bar{m}_3$  (6 V/div) in the overmodulation region with different values of the modulation index when using MD or MPE strategies.

The last tests carried out concern the speed transient of the electric drive when operating with different overmodulation strategies. In all tests, the parameters of the control system are unchanged, and the load torque is negligible. To guarantee the overmodulation operation, the speed setpoint is much greater than the rated speed, so the electric drive reaches the highest speed that is compatible with the available voltage. The modulation index increases up to 1.3, which is adopted as a saturation threshold for the current regulators shown in Fig. 4.9.

As can be seen in Fig. 4.14, the Bs technique shows the highest distortion of the stator current but, observing the result of the speed transient reported in Fig. 4.16, it produces the largest magnitude of the vector  $\bar{v}_1$ , which enables the motor to reach a higher speed (159 rpm/min).

The harmonic distortion produced by the MPE is lower and the final speed (149 rpm/min) is slightly lower than the one reached by the MD technique (156 rpm/min). The MD technique reaches a speed greater than the MPE technique because, as shown in Fig. 4.13, it reaches a modulation index greater. The MD modulation tends to the square wave operation for the highest modulation request. The value of the speed reached by the MD technique in this test is lower than the Bs technique because the modulation index adopted doesn't allow to get the square wave with the MD technique. The last technique analysed was the SVPWM technique. It can be noted that, it has the lowest harmonic content but the machine cannot go beyond 145 rpm/min because the current saturation PI is setting to 1.3. The saturation threshold of the current regulators doesn't allow to reach the square wave operation.

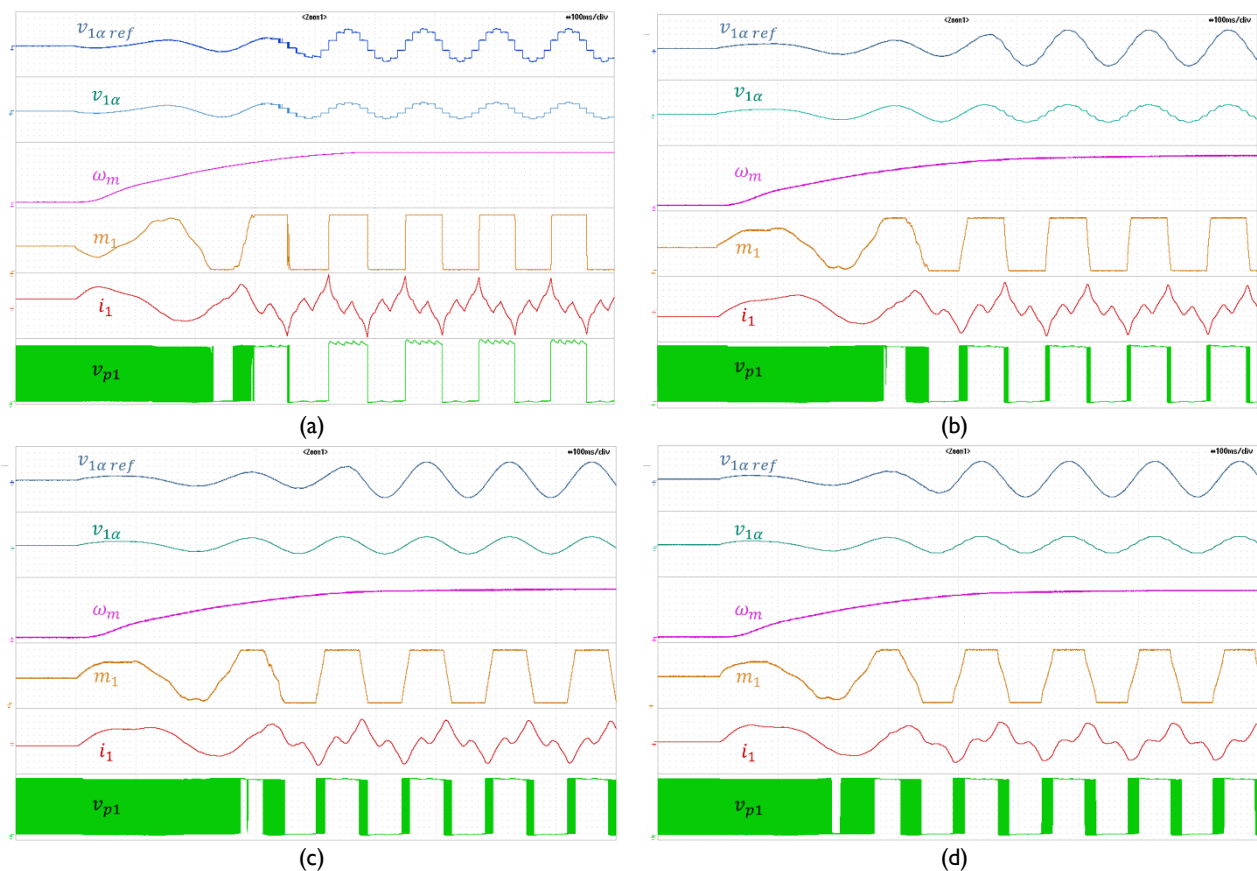


Fig. 4.16. Speed transients of the motor with different overmodulation strategies. (a) Bolognani's strategy. (b) MD strategy. (c) MPE strategy. (d) SVPWM strategy. Waveforms of  $v_{1,ref-\alpha}$  (50 V/div),  $v_{1-\alpha}$  (50 V/div), mechanical speed  $\omega_m$  (20 rpm/min/div), modulating signal  $m_1$  of phase 1 (0.125/div), current of phase 1 (2 A/div), and pole voltage  $v_{p1}$  of phase 1 (12 V/div).

## 4.6 Conclusion

Electric drives that operate into the overmodulation region to obtain a boost in dynamic performance of the motor are nowadays widespread.

In this chapter, it has been shown that, in multi-phase inverters, it is possible to define a new region, different from linear and overmodulation regions, in which it is possible to reach higher values of the modulation index as long as a certain level of voltage distortion is acceptable. This result can be achieved by applying a well defined voltage space vector of higher order, calculated by the analytical expression presented. The analysis developed in this chapter is entirely focused on carrier-based PWM and leads to a closed-form expression of the modulating signals in the extended linear region.

The presented solution allows extending the linear range of the converter by 17%.

Furthermore, in this chapter an extension to multi-phase systems of the well-known three-phase overmodulation methods has been presented.

If the reference voltage is outside the linear and extended linear operating regions, it is still possible to extend further the output voltage by 3–4% if one accepts the voltage distortion of the overmodulation operation.

Finally, in this chapter the performance of different overmodulation strategies has been compared by experimental tests. The strategies analysed are the minimum distance (MD), the minimum phase error (MPE), the Bolognani's modulation (Bs) and the traditional SVPWM modulation.

# Chapter 5

## *Model of Eighteen-Phase Squirrel Cage Induction Machine*

*In this chapter, the mathematical model of an eighteen-phase squirrel cage induction motor is obtained. This particular electric machine will be used for the development of an innovative variable-pole motor drive for traction applications. The pole number switching can be achieved electronically.*

*The machine initially proposed for this aim was a toroidally-wound induction motor with 36 stator independent phases. An example of this machine is presented in [61].*

*Subsequently, it has been decided to simplify the system by considering a more conventional eighteen-phase machine with full pitch stator coils.*

*The model takes into account up to the 35<sup>th</sup> spatial harmonic of the magnetic field in the air gap, and is based on the Vector Space Decomposition approach.*

*This activity is the result of part of a collaboration carried out with the KTH, Royal Institute of Technology in Stockholm.*

## 5.1 Magnetic Field

A representation of the cross-section of the considered eighteen phase two poles squirrel cage induction machine is shown in Fig. 5.1. As is possible to observe, the machine analysed has 36 stator slots and 28 rotor bars.

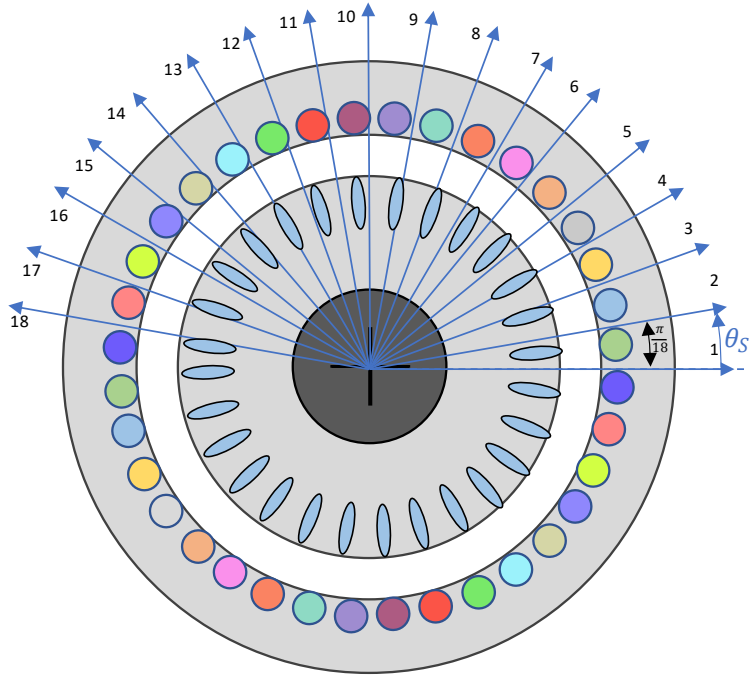


Figure 5.1. Cross section of the eighteen phase two poles squirrel cage induction machine, with the magnetic axes of the eighteen stator coils.

The stator winding is constituted by 18 coils, symmetrically distributed in the stator slots. The pitch of the coils is  $\pi$  mechanical radians. As shown in Fig. 5.1, the magnetic axes of the coils are rotated to each other of  $\pi/18$ , and a stator reference frame with angular coordinate  $\theta_s$  is defined.

The following relationship defines the angular position of the magnetic axis of the  $k^{th}$  phase:

$$\psi_{SK} = \frac{(k-1)\pi}{18} \text{ for } k = 1, 2, \dots, 18. \quad (5.1)$$

Considering the hypotheses reported in Cap.1, the magnetic field in the air gap is determined as the sum of two contributions, the magnetic field produced by the 18 stator coils and the magnetic field produced by the 28 rotor bars.

### 5.1.1 Magnetic Field Produced by the Stator Currents

According to (1.10), and observing the magnetic axis positions in Fig. 5.1, it is possible to obtain the following expression of the magnetic field in the air gap produced by the stator windings of the machine.

$$h_S(\theta_s, t) = \sum_{\rho \text{ odd}} \frac{N_s}{\pi \delta \rho} \sin\left(\rho \frac{\pi}{2}\right) \operatorname{Re} \left[ e^{-j\rho\theta_s} \left( \sum_{k=1}^{18} i_{Sk} e^{j\frac{(k-1)\pi\rho}{18}} \right) \right] \quad (5.2)$$

By introducing the complex constant  $\bar{\alpha}_{18} = e^{\frac{j\pi}{18}}$ , (5.2) can be rewritten as:

$$h_S(\theta_s, t) = \sum_{\rho \text{ odd}} \frac{N_s}{\pi \delta \rho} \sin\left(\rho \frac{\pi}{2}\right) \operatorname{Re} \left[ e^{-j\rho\theta_s} \left( \sum_{k=1}^{18} i_{Sk} \bar{\alpha}_{18}^{(k-1)\rho} \right) \right] \quad (5.3)$$

From (5.3), it is possible to define a Clarke transformation useful to represent the stator quantities of the specific machine under study. Therefore, the generic  $\rho^{\text{th}}$  stator current space vector for the eighteen-phase system can be expressed as:

$$\bar{i}_{S\rho} = \frac{1}{9} \sum_{k=1}^{18} i_{Sk} \bar{\alpha}_{18}^{(k-1)\rho} \quad \forall \rho \text{ odd} \quad (5.4)$$

It is possible to demonstrate that the number of independent space vectors is nine for the eighteen-phase system. The choice of which space vectors to consider in the analysis is a degree of freedom. According to (5.3) only the odd space vector are adopted because they are directly linked to the spatial harmonics of the magnetic field in the air gap.

The space vectors adopted to represent the eighteen-phase system are:  $\bar{i}_{S1}, \bar{i}_{S3}, \bar{i}_{S5}, \bar{i}_{S7}, \bar{i}_{S9}, \bar{i}_{S11}, \bar{i}_{S13}, \bar{i}_{S15}, \bar{i}_{S17}$ . Other space vectors can be chosen, but they are linear combinations of the selected ones.

It is possible to verify that the following relationships hold.

$$\bar{i}_{S1} = \bar{i}_{S\rho} \quad \text{for } \rho = 1, 19, 37, \dots \quad (5.5)$$

$$\bar{i}_{S3} = \bar{i}_{S\rho} \quad \text{for } \rho = 3, 21, 39, \dots \quad (5.6)$$

$$\bar{i}_{S5} = \bar{i}_{S\rho} \quad \text{for } \rho = 5, 23, 41, \dots \quad (5.7)$$

$$\bar{i}_{S7} = \bar{i}_{S\rho} \quad \text{for } \rho = 7, 25, 43, \dots \quad (5.8)$$

$$\bar{i}_{S9} = \bar{i}_{S\rho} \quad \text{for } \rho = 9, 27, 45, \dots \quad (5.9)$$

$$\bar{i}_{S11} = \bar{i}_{S\rho} \quad \text{for } \rho = 11, 29, 47, \dots \quad (5.10)$$

$$\bar{i}_{S13} = \bar{i}_{S\rho} \quad \text{for } \rho = 13, 31, 49, \dots \quad (5.11)$$

$$\bar{i}_{S15} = \bar{i}_{S\rho} \quad \text{for } \rho = 15, 33, 51, \dots \quad (5.12)$$

$$\bar{i}_{S17} = \bar{i}_{S\rho} \quad \text{for } \rho = 17, 35, 53, \dots \quad (5.13)$$

The inverse transformation can be written as:

$$i_{Sk} = Re \left[ \sum_{\rho=1}^{17} \bar{i}_{S\rho} \bar{\alpha}_{18}^{-\rho(k-1)} \right] \quad (5.14)$$

It is possible to verify the validity of the inverse transformation with the following procedure. Introducing (5.14) into (5.4) and remembering the Eulero trigonometric relationship (1.121) it is possible to write:

$$\bar{i}_{S\rho} = \frac{1}{18} \sum_{k=1}^{18} \sum_{l=1,3,5}^{17} [\bar{i}_{Sl} \bar{\alpha}^{-l(k-1)} + \bar{i}_{Sl}^* \bar{\alpha}^{l(k-1)}] \bar{\alpha}^{\rho(k-1)} \quad (5.15)$$

After few steps, (5.15) can be rewritten as:

$$\bar{i}_{S\rho} = \frac{1}{18} \sum_{l=1,3,5}^{17} \bar{i}_{Sl} \sum_{k=1}^{18} \bar{\alpha}^{(\rho-l)(k-1)} + \frac{1}{18} \sum_{l=1,3,5}^{17} \bar{i}_{Sl}^* \sum_{k=1}^{18} \bar{\alpha}^{(\rho+l)(k-1)} \quad (5.16)$$

where the second term of the second member is always null, instead the first is equal to 18 only when  $l = \rho$ , and null in any other case. This guarantees the validity of the inverse transformation.

Introducing (5.4) in to (5.3) leads to:

$$h_s(\theta_s, t) = \sum_{\rho(\text{odd})=1}^{\infty} 9 \frac{N_s}{\rho\pi\delta p} \sin\left(\rho \frac{\pi}{2}\right) \Re_e[\bar{i}_{S\rho} e^{-j\rho\theta_s}] \quad (5.17)$$

By comparing (5.17) with (1.19), it is possible to obtain the following relationships between the stator current space vectors and the corresponding stator magnetic field space vectors:

$$\bar{h}_{s\rho} = 9 \frac{N_s}{\pi \delta p} \frac{\sin\left(\rho \frac{\pi}{2}\right)}{\rho} \bar{i}_{s\rho} \quad (5.18)$$

Observing (5.18) it is important to underline that the  $\rho^{th}$  harmonic of the magnetic field is produced by the  $\rho^{th}$  current space vector.

### 5.1.2 Magnetic Field Produced by the Rotor Currents

The squirrel cage is here analysed according to an equivalent circuit defined by  $N_B$  loops. Each loop is composed by two adjacent bars and the portions of rings between them. In Fig. 5.2, the generic  $k^{th}$  loop of the rotor cage is shown. The general description of the current distribution in the rotor cage is based on the definition of 28 independent loop currents. A further loop current (flowing in one of the two rings) would be strictly necessary from a pure circuitual point of view. However, in absence of axial flux components, this component is null.

The  $k^{th}$  loop current  $i_{l(k)}$  is shown in Fig. 5.2 [62].

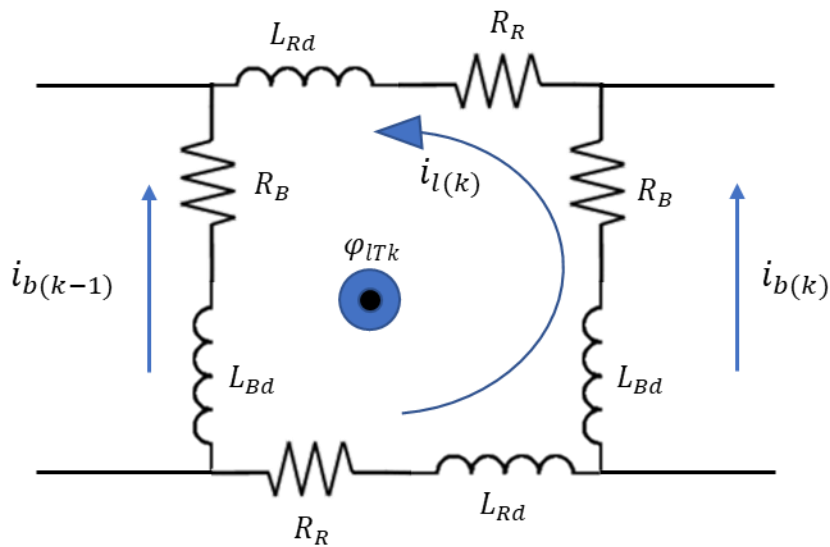


Fig. 5.2. Equivalent circuit of the  $k^{th}$  loop of the rotor cage.

$R_B$  is the resistance of a bar and  $L_{Bd}$  is the corresponding leakage inductance,  $R_R$  is the resistance of the portion of the ring between two adjacent bars and  $L_{Rd}$  is the corresponding leakage inductance. The mutual leakage inductances between different bars and between bars and rings are neglected in the analysis because considered not significant in a squirrel cage.

The magnetic axes of the 28 rotor loops are illustrated in Fig. 5.3.



By performing a spatial Fourier expansion of the magnetic field produced by the generic loop current, having  $\psi_{Rk}$  as magnetic axis, and summing the contributions of all the rotor loop currents, leads to:

$$h_R(\theta_R, t) = N_B \sum_{\rho=1}^{\infty} \frac{2}{\pi \delta \rho} \sin\left(\frac{\rho\pi}{N_B}\right) \Re_e \left[ \sum_{k=1}^{28} i_{l(k)} e^{j\rho\psi_{Rk}} e^{-j\rho\theta_R} \right] \quad (5.21)$$

In agreement with the definition of rotor reference frame shown in Fig. 5.3, the coordinates of the magnetic axis of all the loop currents can be expressed as follows:

$$\psi_{Rk} = \frac{2\pi}{28} (k-1) \quad (5.22)$$

Introducing (5.22), (5.21) becomes:

$$h_R(\theta_R, t) = N_B \sum_{\rho=1}^{\infty} \frac{2}{\pi \delta \rho} \sin\left(\frac{\rho\pi}{N_B}\right) \Re_e \left[ \sum_{k=1}^{28} i_{l(k)} e^{j\rho \frac{2\pi}{28} (k-1)} e^{-j\rho\theta_R} \right] \quad (5.23)$$

Once again, from (5.23), it is possible to define a Clarke transformation useful to represent the rotor quantities of the specific machine under study. Therefore, the generic  $\rho^{th}$  loop current space vector for the twenty-eight-phase system can be expressed as:

$$\bar{i}_{R\rho} = \frac{2}{28} \sum_{k=1}^{28} i_{l(k)} \bar{\alpha}_{28}^{\rho(k-1)} \quad (5.24)$$

where  $\bar{\alpha}_{28} = e^{j\frac{2\pi}{28}}$ .

The inverse transformation can be written as:

$$i_{l(k)} = \operatorname{Re} \left[ \sum_{\rho=1}^{27} \bar{i}_{R\rho} \bar{\alpha}_{28}^{-\rho(k-1)} \right] \quad (5.25)$$

The magnetic field produced by the rotor currents can be expressed as:

$$h_R(\theta_R, t) = \sum_{\rho=1}^{\infty} \Re_e [\bar{h}_{R\rho} e^{-j\rho\theta_R}] \quad (5.26)$$

where:

$$\bar{h}_{R\rho} = \frac{28}{\pi \delta \rho} \sin\left(\frac{\rho\pi}{N_B}\right) \bar{i}_{R\rho} \quad (5.27)$$

### 5.1.3 Air Gap Magnetic Field

The total magnetic field in the air gap can be obtained as the sum of stator and rotor contributions, in the same reference frame, as shown in (5.28) and (5.29).

$$\bar{h}_{T\rho}^S = \bar{h}_{S\rho} + \bar{h}_{R\rho} e^{j\rho\theta} \quad (5.28)$$

$$\bar{h}_{T\rho}^R = \bar{h}_{S\rho} e^{-j\rho\theta} + \bar{h}_{R\rho} \quad (5.29)$$

Introducing (5.18) and (5.27) into (5.28) and (5.29) leads to:

$$\bar{h}_{T\rho}^S = 9 \frac{N_s}{\pi\delta} \frac{\sin\left(\rho \frac{\pi}{2}\right)}{\rho} \bar{i}_{S\rho} + \frac{28}{\pi\delta\rho} \sin\left(\frac{\rho\pi}{N_B}\right) \bar{i}_{R\rho} e^{j\rho\theta} \quad (5.30)$$

$$\bar{h}_{T\rho}^R = 9 \frac{N_s}{\pi\delta} \frac{\sin\left(\rho \frac{\pi}{2}\right)}{\rho} \bar{i}_{S\rho} e^{-j\rho\theta} + \frac{28}{\pi\delta\rho} \sin\left(\frac{\rho\pi}{N_B}\right) \bar{i}_{R\rho} \quad (5.31)$$

## 5.2 Flux Linkages

To complete the mathematical model of the machine, it is necessary to achieve the expressions of the flux linkages with the stator phases and the rotor current loops.

### 5.2.1 Flux Linkage with a Stator Ohase

The total flux linkage with a generic phase  $k$  is the sum of the leakage flux and the flux due to the magnetic field in the air gap. By applying the Clarke transformation, it is possible to write:

$$\bar{\varphi}_{S\rho} = \bar{\varphi}_{Sd\rho} + \bar{\varphi}_{ST\rho} \quad \rho = 1, 3, \dots, 17. \quad (5.32)$$

Introducing (5.30) and (5.1) in (1.27) leads to:

$$\varphi_{STk} = \frac{\mu_0 N_s L \tau}{\pi} \sum_{h(\text{odd})=1}^{\infty} \frac{(-1)^{\frac{h-1}{2}}}{h} \Re_e \left[ \bar{h}_{Th}^S e^{-j\rho \frac{2\pi}{28}(k-1)} \right] \quad (5.33)$$

Applying the Clarke transformation to (5.33), it is possible to achieve the following relationships:

$$\bar{\varphi}_{ST\rho} = \frac{N_S L \mu_0 \tau}{\rho \pi} \bar{h}_{T\rho}^S \quad \rho = 1, 3, \dots, 17. \quad (5.34)$$

Similarity, it is possible to define the space vectors of the leakage flux as:

$$\bar{\varphi}_{Sd\rho} = L_{Sd\rho} \bar{i}_{S\rho} \quad \rho = 1, 3, \dots, 17. \quad (5.35)$$

where  $L_{Sd\rho}$  is the stator leakage inductance in the  $\rho$ -th subspace, that describes the flux produced by each stator phase and does not reach the airgap.

$$L_{S\rho} = L_{Sd\rho} + L_{SS\rho} \quad (5.36)$$

Introducing (5.30) in (5.34) leads to:

$$\bar{\varphi}_{ST\rho} = 9 \frac{N_S^2 L \mu_0 \tau}{\rho^2 \pi^2 \delta} \sin\left(\rho \frac{\pi}{2}\right) \bar{i}_{S\rho} + 28 \frac{N_S L \mu_0 \tau}{\rho^2 \pi^2 \delta} \sin\left(\frac{\rho \pi}{N_B}\right) \bar{i}_{R\rho} e^{j\rho\theta} \quad (5.37)$$

From (5.37) It is possible to define the self-inductances  $L_{SS\rho}$  and the mutual inductances  $M_{S\rho}$  as follows:

$$L_{SS\rho} = \frac{9N_S^2 L \mu_0 \tau}{\pi^2 \delta \rho^2} \quad (5.38)$$

$$M_{S\rho} = \frac{28N_S L \mu_0 \tau}{\pi^2 \delta \rho^2} \sin\left(\frac{\rho \pi}{N_B}\right) \quad (5.39)$$

### 5.2.2 Flux linkage with a Rotor Loop

The flux linkage with a rotor loop is the sum of two contributions. The first one is the flux linkage due to the magnetic field in the air gap, the second one is the leakage flux, as emphasized in (5.40).

$$\bar{\varphi}_{R\rho} = \bar{\varphi}_{Rd\rho} + \bar{\varphi}_{RT\rho} \quad \rho = 1, 3, \dots, 17 \quad (5.40)$$

The second term in the right side  $\bar{\varphi}_{RT\rho}$  is the flux linkage due to the magnetic field in the air gap and can be expressed, by introducing (5.26) in to (1.24), as:

$$\bar{\varphi}_{RT\rho} = \frac{L \mu_0 \tau}{\pi \rho} \sin\left(\frac{\rho \pi}{N_B}\right) \bar{h}_{T\rho}^R \quad \rho = 1, 3, \dots, 17. \quad (5.41)$$

The first term in the right side  $\bar{\varphi}_{Rd\rho}$  is the leakage flux, and can be expressed as:

$$\bar{\varphi}_{Rd\rho} = L_{Rd\rho} \bar{i}_{R\rho} \quad \rho = 1, 3, \dots, 17. \quad (5.42)$$

where  $L_{Rd\rho}$  is the rotor leakage inductance in the  $\alpha_\rho - \beta_\rho$  plane that describes the flux that is produced by the rotor phases but does not reach the airgap.

Introducing (5.31) in (5.41) leads to:

$$\bar{\varphi}_{RT\rho} = 9 \frac{N_S L \mu_0 \tau}{\pi^2 \delta \rho^2} \sin\left(\frac{\rho\gamma}{2}\right) \sin\left(\rho \frac{\pi}{2}\right) \bar{i}_{S\rho} e^{-j\rho\theta} + 28 \frac{L \mu_0 \tau}{\pi^2 \delta \rho^2} \left(\sin\left(\frac{\rho\pi}{N_B}\right)\right)^2 \bar{i}_{R\rho} \quad (5.43)$$

From (5.43), it is possible to define the self-inductances  $L_{RR\rho}$  and the mutual inductances  $M_{R\rho}$  as follows:

$$L_{RR\rho} = 28 \frac{L \mu_0 \tau}{\pi^2 \delta \rho^2} \left(\sin\left(\frac{\rho\pi}{N_B}\right)\right)^2 \quad (5.44)$$

$$M_{R\rho} = 9 \sin\left(\rho \frac{\pi}{2}\right) \frac{N_S L \mu_0 \tau}{\pi^2 \delta \rho^2} \sin\left(\frac{\rho\pi}{N_B}\right) \quad (5.45)$$

The rotor inductance is defined as the sum of the leakage and self inductance.

$$L_{R\rho} = L_{Rd\rho} + L_{RR\rho} \quad (5.46)$$

### 5.3 Voltage Equations

The stator voltage equations of the machine can be written in terms of space vectors as:

$$\bar{V}_{S\rho} = R_S \bar{i}_{S\rho} + \frac{d\bar{\varphi}_{S\rho}}{dt} \quad \rho = 1, 3, \dots, 17. \quad (5.47)$$

where  $R_S$  is the resistance of the stator phase and  $\bar{\varphi}_{S\rho}$  is evaluate by (5.32).

The squirrel cage is analysed with reference to the equivalent circuit shown in Fig. 5.2.

By applying Kirchhoff's law, the voltage equation of the  $k^{th}$  rotor loop can be written as:

$$0 = (2R_B + 2R_R) i_{l(k)} + (2L_{Bd} + 2L_{Rd}) \frac{d i_{l(k)}}{dt} - R_B i_{l(k-1)} - R_B i_{l(k+1)} - L_{Bd} \frac{d i_{l(k-1)}}{dt} - L_{Bd} \frac{d i_{l(k+1)}}{dt} + \frac{d\varphi_{lTk}}{dt} \quad (5.48)$$

where  $\varphi_{ITk}$  is the flux linkage with the  $k^{th}$  rotor loop due to the air gap magnetic field.

By means of the Clarke transformation and with some manipulations (5.48) can be rewritten as:

$$0 = (2R_B - R_B \bar{\alpha}_{28}^\rho - R_B \bar{\alpha}_{28}^{(-\rho)} + 2R_R) \bar{i}_{R\rho} + (2L_{Bd} - L_{Bd} \bar{\alpha}_{28}^\rho - L_{Bd} \bar{\alpha}_{28}^{(-\rho)} + 2L_R) \frac{d\bar{i}_{R\rho}}{dt} + \frac{d\bar{\varphi}_{RT\rho}}{dt} \quad (5.49)$$

From (5.49), it is possible to define the equivalent rotor loop resistance in the  $\alpha_\rho - \beta_\rho$  plane and the corresponding equivalent rotor loop leakage inductance as:

$$R_{R\rho} = (2R_B - R_B \bar{\alpha}_{28}^\rho - R_B \bar{\alpha}_{28}^{(-\rho)} + 2R_R) \quad (5.50)$$

$$L_{Rd\rho} = (2L_{Bd} - L_{Bd} \bar{\alpha}_{28}^\rho - L_{Bd} \bar{\alpha}_{28}^{(-\rho)} + 2L_R) \quad (5.51)$$

The final voltage equations in terms of space vectors of the rotor squirrel cage can be written as:

$$0 = R_{R\rho} \bar{i}_{R\rho} + L_{Rd\rho} \frac{d\bar{i}_{R\rho}}{dt} + \frac{d\bar{\varphi}_{TR\rho}}{dt} \quad (5.52)$$

## 5.4 Electromagnetic Torque

Starting by (1.32) and introducing the expressions of the magnetic field generated by stator (5.18) and rotor (5.28) currents, it is possible to express the electromagnetic torque as:

$$T_{em} = \mu_0 p^2 \delta L \tau \sum_{\rho \text{ odd}} \rho \left[ 9 \frac{N_s}{\pi \delta} \frac{\sin\left(\frac{\rho \pi}{2}\right)}{\rho} \bar{i}_{S\rho} \cdot j \frac{28}{\pi \delta \rho} \sin\left(\frac{\rho \pi}{N_B}\right) \bar{i}_{R\rho} e^{j\rho\theta} \right] \quad (5.53)$$

Introducing the mutual induction coefficients defined by (5.39), leads to:

$$T_{em} = 9 p \sum_{\rho \text{ odd}} \rho M_{R\rho} (\bar{i}_{S\rho} \cdot j \bar{i}_{R\rho} e^{j\rho\theta}) \quad (5.54)$$

As can be seen, there are many contributions, one for each  $\rho$  ( $\rho = 1, 3, \dots, 17$ ).

## 5.5 Summary of the Mathematical Model of the Eighteen-Phase Two Poles Squirrel Cage Induction Machines

The mathematical model of the eighteen-phase two poles squirrel cage induction machine, previously determined, expressed in terms of space vectors, is summarized hereafter. Note that, the model takes into account up to the 35th spatial harmonic of the magnetic field in the air gap.

### 5.5.1 Equations

$$\bar{V}_{S\rho} = R_S \bar{i}_{S\rho} + \frac{d\bar{\varphi}_{S\rho}}{dt} \quad \rho = 1, 3, \dots, 17. \quad (5.55)$$

$$0 = R_{R\rho} \bar{i}_{R\rho} + \frac{d\bar{\varphi}_{R\rho}}{dt} \quad \rho = 1, 3, \dots, 17. \quad (5.56)$$

$$\bar{\varphi}_{S\rho} = \bar{\varphi}_{Sd\rho} + \bar{\varphi}_{ST\rho} \quad \rho = 1, 3, \dots, 17. \quad (5.57)$$

$$\bar{\varphi}_{R\rho} = \bar{\varphi}_{Rd\rho} + \bar{\varphi}_{RT\rho} \quad \rho = 1, 3, \dots, 17. \quad (5.58)$$

$$\bar{\varphi}_{RT\rho} = L_{RR\rho} \bar{i}_{R\rho} + M_{R\rho} \bar{i}_{S\rho} e^{-j\rho\theta} \quad \rho = 1, 3, \dots, 17. \quad (5.59)$$

$$\bar{\varphi}_{Rd\rho} = L_{Rd\rho} \bar{i}_{R\rho} \quad \rho = 1, 3, \dots, 17. \quad (5.60)$$

$$\bar{\varphi}_{ST\rho} = L_{SS\rho} \bar{i}_{S\rho} + M_{S\rho} \bar{i}_{R\rho} e^{j\rho\theta} \quad \rho = 1, 3, \dots, 17. \quad (5.61)$$

$$\bar{\varphi}_{Sd\rho} = L_{Sd\rho} \bar{i}_{S\rho} \quad \rho = 1, 3, \dots, 17. \quad (5.62)$$

$$\bar{h}_{T\rho}^S = 9 \frac{N_s}{\pi\delta} \frac{\sin\left(\frac{\rho\pi}{2}\right)}{\rho} \bar{i}_{S\rho} + \frac{28}{\pi\delta\rho} \sin\left(\frac{\rho\pi}{N_B}\right) \bar{i}_{R\rho} e^{j\rho\theta} \quad \rho = 1, 3, \dots, 17. \quad (5.63)$$

$$\bar{h}_{T\rho}^R = 9 \frac{N_s}{\pi\delta} \frac{\sin\left(\frac{\rho\pi}{2}\right)}{\rho} \bar{i}_{S\rho} e^{-j\rho\theta} + \frac{28}{\pi\delta\rho} \sin\left(\frac{\rho\pi}{N_B}\right) \bar{i}_{R\rho} \quad \rho = 1, 3, \dots, 17. \quad (5.64)$$

$$T_{em} = 9 \sum_{\rho=1,3,\dots}^{17} \rho M_{R\rho} (\bar{i}_{S\rho} \cdot j \bar{i}_{R\rho} e^{j\rho\theta}) \quad (5.65)$$

### 5.5.2 MatLab- Simulink Tests

In this type of machine, the variation of the number of polar pairs can be obtained by activating one of the different space vectors available. For example, by supplying the machine with the voltage space vector  $\bar{V}_{S1}$ , a two-pole magnetic field is obtained in the air gap. Otherwise, by supplying the machine with the voltage space vector  $\bar{V}_{S3}$  a six-pole magnetic field is obtained in the air gap.

The mathematical model of the machine has been implemented in MatLab. The script has been realized for evaluating the behaviour of a variable pole number motor drive. The machine has been firstly supplied with the space vector one to evaluate the behaviour of the machine when operate with two pole. After that, the machine has been supplied with the space vector three to evaluate the behaviour of the machine when operate with six pole.

The tests on the machine have been performed with the same magnetic flux in the yoke.

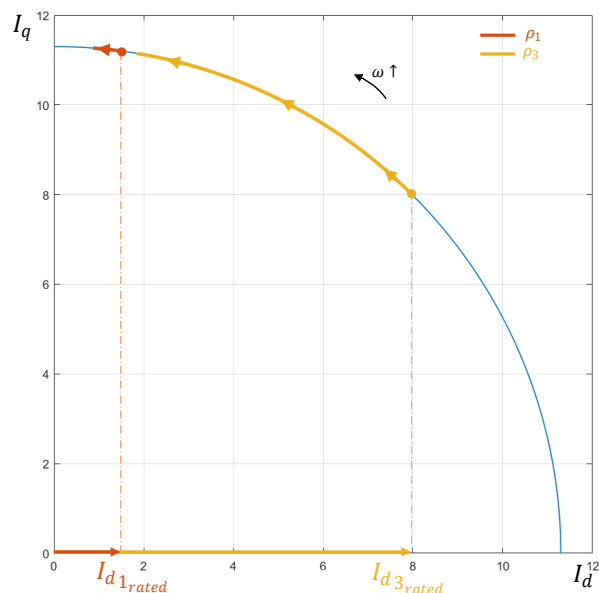


Figure 5.5. Current reference of the machine supplied in space one  $\rho_1$  (orange track – two poles operation mode), and space three  $\rho_3$  (yellow track – six poles operation mode).

As can be seen in Fig. 5.5, to keep the magnetic flux in the yoke equal in both tests and below the limit constraint due to the geometry, the value of  $I_{d1\_rated}$  is less than  $I_{d3\_rated}$ . In this situation when the machine works with six-pole, it can work in to the MPTA point until the current limit is reached. The operating point then moves to the circular current limits.

On the contrary, when the machine is powered with space one (two poles operating mode), it cannot work on the MPTA to respect the imposed constraint. It starts to working on the circular current limit.

The results of the comparison of the two tests are shown in Fig. 5.6.

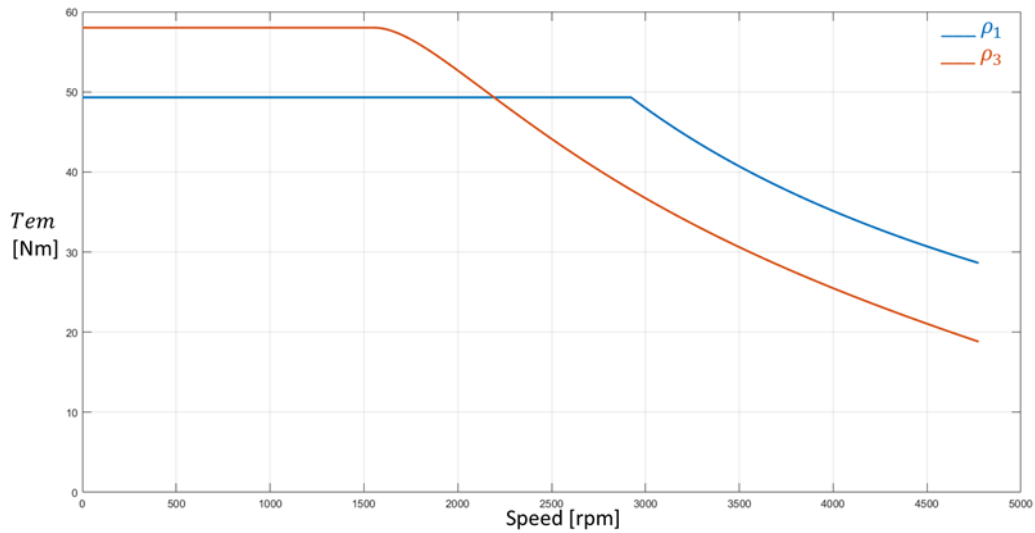


Figure 5.6. Comparison between the operating ranges of an eighteen-phase cage rotor induction machine supplied in space one  $\rho_1$  (blue track – two poles operation mode), and space three  $\rho_3$  (orange track – six poles operation mode).

As can be seen, six pole operation mode can produce more torque at low speed, whereas, on the contrary, two pole operation mode allows to achieve more torque at high speed. It is worth noting that the performance of the motor drive is strictly dependent on the machine design.

Consequently, the variable pole number motor drive can represent a valid option for an electric vehicle powertrain, because it allows obtaining the same behaviour as a conventional powertrain with variable mechanical transmission.

# Conclusion

*In this thesis, several research activities concerning multi-phase machines and drives, as well as multilevel inverters, have been presented, with the aim to contribute to the technological development of electric vehicles.*

*First of all, detailed mathematical models of two different multi-phase machines, i.e., the five-phase induction machine, and the asymmetrical six-phase permanent magnet synchronous machine, potentially appealing for an innovative electric vehicle powertrain, have been presented. The models take into account several spatial harmonics of the magnetic field in the air gap, and are based on the Vector Space Decomposition approach.*

*Then, a new modulation strategy for multi-phase multilevel inverters, which uses the zero-sequence component of the modulating signals to annul the voltage oscillation on the DC-link capacitors in every cycle, has been presented. It was shown that the proposed solution can annul the oscillation also during an open phase fault, and it can be used to flexibly change the voltage level of the two capacitors of the DC-link. All these aspects have been validated by experimental tests carried out on a three-level five-phase T-type inverter.*

*After, an online diagnostic algorithm, able to estimate the rotor magnet demagnetization in a six-phase permanent magnet synchronous motor during the machine operation, has been presented. This technique could be usefully adopted in an electric vehicle powertrain for the monitoring of the state of health of the traction motor, to guarantee the correct operation of the system. A complete analysis of the magnetic field produced by rotor magnets with parallel magnetization has been introduced for supporting the proposed algorithm. The behaviour of the proposed fault detection strategy has been verified by some preliminary experimental tests performed on two prototypes of six-phase permanent magnet synchronous motors.*

*Subsequently, the modulation regions for a five-phase inverter have been analysed. A new region between the linear modulation region and the overmodulation region, called extended linear modulation region, has been defined. In this region, the inverter can operate in linear modulation region with the fundamental voltage space vector, exploiting the inherent degrees of freedom of a multi-phase inverter. For an automotive application, this feature is very interesting because it allows increasing the voltage available to supply the machine, which becomes a boost of the speed of the machine. Moreover, a generalisation for five-phase inverters of the traditional three-phase overmodulation techniques has been presented.*

*In the end, a model of an eighteen phase squirrel cage induction motor has been developed. The number of poles of this particular electric machine can be varied electronically during operation. This peculiarity is appealing for traction applications.*

*The laboratory activities have been carried out in the Laboratory of Electric Machine and Drives (LEMAD) of the University of Bologna.*



# References

- [1] J. W. Kelly, E. G. Strangas and J. M. Miller, "Multiphase space vector pulse width modulation," in *IEEE Transactions on Energy Conversion*, vol. 18, no. 2, pp. 259-264, June 2003.
- [2] L. Parsa, "On advantages of multi-phase machines," 31st Annual Conference of IEEE Industrial Electronics Society, 2005. IECON 2005.
- [3] R. O. C. Lyra and T. A. Lipo, "Torque density improvement in a six-phase induction motor with third harmonic current injection," in *IEEE Transactions on Industry Applications*, vol. 38, no. 5, pp. 1351-1360, Sept.-Oct. 2002.
- [4] S. Williamson and S. Smith, "Pulsating torque and losses in multiphase induction machines," in *IEEE Transactions on Industry Applications*, vol. 39, no. 4, pp. 986-993, July-Aug. 2003.
- [5] E. Semail, X. Kestelyn and F. Locment, "Fault tolerant multiphase electrical drives: The impact of design," 2007 IET Colloquium on Reliability in Electromagnetic Systems, 2007, pp. 1-5.
- [6] J. A. Haylock, B. C. Mecrow, A. G. Jack, and D. J. Atkinson, "Operation of a fault tolerant PM drive for an aerospace fuel pump application," *IEE Proceedings of Electric Power Applications*, vol. 145, Sept. 1998, pp. 441 – 448
- [7] M. Bagheri, E. Farjah and T. Ghanbari, "Selective Utilized Phase Number of Multiphase Induction Motors Strategy to Enhance Electric Vehicles' Drive Range," 2021 12th Power Electronics, Drive Systems, and Technologies Conference (PEDSTC), 2021, pp. 1-5.
- [8] I. Bolvashenkov, J. Kammermann, H. Herzog, I. Frenkel, E. Ikar and L. Khvatskin, "Investigation of reliability and fault tolerance of multiphase traction electric motor supplied with multi power source based on Lz-transform," 2017 2nd International Conference on System Reliability and Safety (ICSRS), 2017, pp. 303-309.
- [9] J. Rodriguez, Jih-Sheng Lai and Fang Zheng Peng, "Multilevel inverters: a survey of topologies, controls, and applications," in *IEEE Transactions on Industrial Electronics*, vol. 49, no. 4, pp. 724-738, Aug. 2002.
- [10] A. E. ElGebaly, A. El-Wahab Hassan and M. K. El-Nemr, "Reactive Power Compensation by Multilevel Inverter STATCOM for Railways Power Grid," 2019 IEEE Conference of Russian Young Researchers in Electrical and Electronic Engineering (ElConRus), 2019, pp. 2094-2099.
- [11] K. Thantirige, A. K. Rathore, S. K. Panda, G. Jayasignhe, M. A. Zagrodnik and A. K. Gupta, "Medium voltage multilevel converters for ship electric propulsion drives," 2015 International Conference on Electrical Systems for Aircraft, Railway, Ship Propulsion and Road Vehicles (ESARS), 2015, pp. 1-7,

- [12] M. A. Abdel-Moamen, S. A. Shaaban and F. Jurado, "France-Spain HVDC transmission system with hybrid modular multilevel converter and alternate-arm converter," 2017 Innovations in Power and Advanced Computing Technologies (i-PACT), 2017, pp. 1-6.
- [13] V. Yaramasu, B. Wu, P. C. Sen, S. Kouro and M. Narimani, "High-power wind energy conversion systems: State-of-the-art and emerging technologies," in Proceedings of the IEEE, vol. 103, no. 5, pp. 740-788, May 2015.
- [14] F. Ma et al., "A Railway Traction Power Conditioner Using Modular Multilevel Converter and Its Control Strategy for High-Speed Railway System," in IEEE Transactions on Transportation Electrification, vol. 2, no. 1, pp. 96-109, March 2016.
- [15] F. Crescimbeni, A. Lidozzi and L. Solero, "High-Speed Generator and Multilevel Converter for Energy Recovery in Automotive Systems," in IEEE Transactions on Industrial Electronics, vol. 59, no. 6, pp. 2678-2688, June 2012.
- [16] M. Gleissner and M. M. Bakran, "Design and Control of Fault-Tolerant Nonisolated Multiphase Multilevel DC-DC Converters for Automotive Power Systems," in IEEE Transactions on Industry Applications, vol. 52, no. 2, pp. 1785-1795, March-April 2016.
- [17] J. Rodriguez, S. Bernet, B. Wu, J. O. Pontt and S. Kouro, "Multilevel Voltage-Source-Converter Topologies for Industrial Medium-Voltage Drives," in IEEE Transactions on Industrial Electronics, vol. 54, no. 6, pp. 2930-2945, Dec. 2007.
- [18] J. Pou, J. Zaragoza, S. Ceballos, M. Saeedifard and D. Boroyevich, "A Carrier-Based PWM Strategy With Zero-Sequence Voltage Injection for a Three-Level Neutral-Point-Clamped Converter," in IEEE Transactions on Power Electronics, vol. 27, no. 2, pp. 642-651, Feb. 2012.
- [19] C. Wang and Y. Li, "Analysis and Calculation of Zero-Sequence Voltage Considering Neutral-Point Potential Balancing in Three-Level NPC Converters," in IEEE Transactions on Industrial Electronics, vol. 57, no. 7, pp. 2262-2271, July 2010, doi: 10.1109/TIE.2009.2024093.
- [20] N. Celanovic and D. Boroyevich, "A comprehensive study of neutral-point voltage balancing problem in three-level neutral-point-clamped voltage source PWM inverters," in IEEE Transactions on Power Electronics, vol. 15, no. 2, pp. 242-249, March 2000, doi: 10.1109/63.838096.
- [21] I. López et al., "Modulation Strategy for Multiphase Neutral-Point-Clamped Converters," in IEEE Transactions on Power Electronics, vol. 31, no. 2, pp. 928-941, Feb. 2016.
- [22] I. López et al., "Generalized PWM-Based Method for Multiphase Neutral-Point-Clamped Converters With Capacitor Voltage Balance Capability," in IEEE Transactions on Power Electronics, vol. 32, no. 6, pp. 4878-4890, June 2017.
- [23] D. Fernandez, D. D. Reigosa, J. M. Guerrero, Z. Zhu and F. Briz, "Permanent-Magnet Magnetization State Estimation Using High-Frequency Signal Injection," in IEEE Transactions on Industry Applications, vol. 52, no. 4, pp. 2930-2940, July-Aug. 2016.

- [24] D. Reigosa, D. Fernández, Y. Park, A. B. Diez, S. B. Lee and F. Briz, "Detection of Demagnetization in Permanent Magnet Synchronous Machines Using Hall-Effect Sensors," in *IEEE Transactions on Industry Applications*, vol. 54, no. 4, pp. 3338-3349, July-Aug. 2018.
- [25] H. Chen, C. Gao, J. Si, Y. Nie and Y. Hu, "A Novel Method for Diagnosing Demagnetization Fault in PMSM Using Toroidal-Yoke-Type Search Coil," in *IEEE Transactions on Instrumentation and Measurement*, vol. 71, pp. 1-12, 2022, Art no. 7501012.
- [26] Y. -C. Kwon, S. Kim and S. -K. Sul, "Six-Step Operation of PMSM With Instantaneous Current Control," in *IEEE Transactions on Industry Applications*, vol. 50, no. 4, pp. 2614-2625, July-Aug. 2014.
- [27] X. Guo, M. He, and Y. Yang, "Over modulation strategy of power converters: A review," *IEEE Access*, vol. 6, pp. 69528–69544, Oct. 2018.
- [28] S. Bolognani and M. Zigliotto, "Novel digital continuous control of SVM inverters in the overmodulation range," in *IEEE Transactions on Industry Applications*, vol. 33, no. 2, pp. 525-530, March-April 1997.
- [29] J. Prieto, F. Barrero, M. J. Durán, S. Toral Marín and M. A. Perales, "SVM Procedure for  $n$ -Phase VSI With Low Harmonic Distortion in the Overmodulation Region," in *IEEE Transactions on Industrial Electronics*, vol. 61, no. 1, pp. 92-97, Jan. 2014.
- [30] C. Zhou, G. Yang and J. Su, "PWM Strategy With Minimum Harmonic Distortion for Dual Three-Phase Permanent-Magnet Synchronous Motor Drives Operating in the Overmodulation Region," in *IEEE Transactions on Power Electronics*, vol. 31, no. 2, pp. 1367-1380, Feb. 2016.
- [31] P. Young and M. Preindl, "Optimal generalized overmodulation for multiphase PMSM drives," *2017 IEEE Applied Power Electronics Conference and Exposition (APEC)*, 2017, pp. 500-505.
- [32] J. Liu, J. Bai, P. Zheng, S. Zhang, M. Wang and Z. Yin, "Torque Analysis of Magnetic-Field-Modulated Double-Rotor Machines with Virtual Work Method," *2018 21st International Conference on Electrical Machines and Systems (ICEMS)*, 2018, pp. 1885-1889.
- [33] L. Zarri, M. Mengoni, A. Tani, G. Serra, Y. Gritli and F. Filippetti, "Control of a multi-motor drive based on five-phase tubular PM actuators for positioning systems," *2011 IEEE International Electric Machines & Drives Conference (IEMDC)*, 2011, pp. 154-159.
- [34] Rossi C, Gritli Y, Pilati A, Rizzoli G, Tani A, Casadei D. "High Resistance Fault-Detection and Fault-Tolerance for Asymmetrical Six-Phase Surface-Mounted AC Permanent Magnet Synchronous Motor Drives" *Energies* 13, no. 12: 3089.
- [35] F. Dubas and C. Espanet, "Analytical Solution of the Magnetic Field in Permanent-Magnet Motors Taking Into Account Slotting Effect: No-Load Vector Potential and Flux Density Calculation," in *IEEE Transactions on Magnetics*, vol. 45, no. 5, pp. 2097-2109, May 2009.

- [36] Z. Q. Zhu, D. Howe and C. C. Chan, "Improved analytical model for predicting the magnetic field distribution in brushless permanent-magnet machines," in *IEEE Transactions on Magnetics*, vol. 38, no. 1, pp. 229-238, Jan. 2002.
- [37] A. Rahideh and T. Korakianitis, "Analytical Magnetic Field Distribution of Slotless Brushless Machines With Inset Permanent Magnets," in *IEEE Transactions on Magnetics*, vol. 47, no. 6, pp. 1763-1774, June 2011.
- [38] B. P. McGrath and D. G. Holmes, "Multicarrier PWM strategies for multilevel inverters," *IEEE Transactions on Industrial Electronics*, vol. 49, no. 4, pp. 858– 867, Aug. 2002.
- [39] Ó. Lopez, J. Alvarez, J. Doval-Gandoy and F. D. Freijedo, "Multilevel Multiphase Space Vector PWM Algorithm," in *IEEE Transactions on Industrial Electronics*, vol. 55, no. 5, pp. 1933-1942, May 2008.
- [40] A.S. Abdel-Khalik, M.I. Masoud, S. Ahmed, B.W. Williams, "Effect of current harmonic injection on constant rotor volume multiphase induction machine stators: a comparative study," *IEEE Transactions on Industry Applications.*, vol. 48, no. 6, pp. 2002–2013, 2012.
- [41] K. Wang, "Effects of harmonics into magnet shape and current of dual three-phase permanent magnet machine on output torque capability," *IEEE Transactions on Industrial Electronics*, vol. 65, no. 11, pp. 8758–8767, Nov. 2018.
- [42] M. Farshadnia, M. A. M. Cheema, A. Pouramin, R. Dutta, J. E. Fletcher, "Design of optimal winding configurations for symmetrical multiphase concentrated-wound surface-mount PMSMs to achieve maximum torque density under current harmonic injection," *IEEE Transactions on Industrial Electronics*, vol. 65, no. 2, pp. 1751–1761, Feb. 2018.
- [43] Z. S. Du, T. A. Lipo, "High torque density and low torque ripple shaped magnet machines using sinusoidal plus third harmonic shaped magnets," *IEEE Transactions Industry Applications.*, vol. 55, no. 3, pp. 2601–2610, May 2019.
- [44] A. Tani, M. Mengoni, L. Zarri, G. Serra, D. Casadei, "Control of multiphase induction motors with an odd number of phases under open circuit phase faults," *IEEE Transactions on Power Electronics*, vol. 27, no. 2, pp. 565– 577, Feb. 2012.
- [45] L. M. Tolbert, Fang Zheng Peng and T. G. Habetler, "Multilevel converters for large electric drives," in *IEEE Transactions Industry Applications*, vol. 35, no. 1, pp. 36-44, Jan.-Feb. 1999.
- [46] H. Xiong, J. Zhang, M. W. Degner, C. Rong, F. Liang and W. Li, "Permanent-Magnet Demagnetization Design and Validation," *IEEE Transactions on Industry Applications*, Vol. 52, No. 4, pp. 2961– 2970, 2016.
- [47] W. Li, A. Li, and H. Wang, "Anisotropic fracture behavior of sintered rare-earth permanent magnets," *IEEE Trans. Magn.*, vol. 41, no. 8, pp. 2339–2342, Aug. 2005.

- [48] D E. Levi, D. Dujic, M. Jones, and G. Grandi, "Analytical Determination of DC-Bus Utilization Limits in Multiphase VSI Supplied AC Drives," *IEEE Trans. on Energy Conversion*, vol. 23, no. 2, pp. 433-443, June 2008.
- [49] A. G. Yepes, J. Doval-Gandoy and H. A. Toliyat, "Improvement in DC-Link Utilization With Reduced Current and Torque Deterioration for Five-Phase Drives by Combination of Circulating-Current Filters and Simple Carrier-Based PWM Based on Closed-Form Expressions," in *IEEE Transactions on Industrial Electronics*, vol. 68, no. 2, pp. 960-971, Feb. 2021.
- [50] X. Zhang and G. H. B. Foo, "Overmodulation of Constant-Switching-Frequency-Based DTC for Reluctance Synchronous Motors Incorporating Field-Weakening Operation," in *IEEE Transactions on Industrial Electronics*, vol. 66, no. 1, pp. 37-47, Jan. 2019.
- [51] P. Stumpf and S. Halász, "Optimization of PWM for the Overmodulation Region of Two-Level Inverters," in *IEEE Transactions on Industry Applications*, vol. 54, no. 4, pp. 3393-3404, July-Aug.
- [52] E. Levi, D. Dujic, M. Jones and G. Grandi, "Analytical Determination of DC-Bus Utilization Limits in Multiphase VSI Supplied AC Drives," in *IEEE Transactions on Energy Conversion*, vol. 23, no. 2, pp. 433-443, June 2008.
- [53] L. Zarri, M. Mengoni, A. Tani, G. Serra and D. Casadei, "Minimization of the Power Losses in IGBT Multiphase Inverters with Carrier-Based Pulsewidth Modulation," in *IEEE Transactions on Industrial Electronics*, vol. 57, no. 11, pp. 3695-3706, Nov. 2010.
- [54] D. Dujic, M. Jones and E. Levi, "Analysis of Output Current Ripple rms in Multiphase Drives Using Space Vector Approach," in *IEEE Transactions on Power Electronics*, vol. 24, no. 8, pp. 1926-1938, Aug. 2009.
- [55] D. Dujic, M. Jones and E. Levi, "Analysis of Output Current-Ripple RMS in Multiphase Drives Using Polygon Approach," in *IEEE Transactions on Power Electronics*, vol. 25, no. 7, pp. 1838-1849, July 2010.
- [56] Z. Nie and N. Schofield, "Multi-phase VSI DC-link capacitor considerations," *IET Power Applications.*, vol. 13, no. 3, pp. 1838–1849, Mar. 2019.
- [57] X. Guo, M. He, and Y. Yang, "Over modulation strategy of power converters: A review," *IEEE Access*, vol. 6, pp. 69528–69544, Oct. 2018.
- [58] S. Bolognani and M. Zigliotto, "Novel digital continuous control of SVM inverters in the overmodulation range," in *IEEE Transactions on Industry Applications*, vol. 33, no. 2, pp. 525-530, March-April 1997.
- [59] A. Iqbal and S. Moinuddin, "Comprehensive Relationship Between Carrier-Based PWM and Space Vector PWM in a Five-Phase VSI," in *IEEE Transactions on Power Electronics*, vol. 24, no. 10, pp. 2379-2390, Oct. 2009.

- [60] J. Malvar et al., "Graphical Diagram for Subspace and Sequence Identification of Time Harmonics in Symmetrical Multiphase Machines," in *IEEE Transactions on Industrial Electronics*, vol. 61, no. 1, pp. 29-42, Jan. 2014.
- [61] E. Libbos, B. Ku, S. Agrawal, S. Tungare, A. Banerjee and P. T. Krein, "Variable-Pole Induction Machine Drive for Electric Vehicles," 2019 IEEE International Electric Machines & Drives Conference (IEMDC), 2019, pp. 515-522.
- [62] A. R. Munoz and T. A. Lipo, "Complex vector model of the squirrel-cage induction machine including instantaneous rotor bar currents," in *IEEE Transactions on Industry Applications*, vol. 35, no. 6, pp. 1332-1340, Nov.-Dec. 1999.